Shallow Donor Qubits in ZnO Nanowires for Quantum Applications

Maria Leena Kyllikki Viitaniemi

A dissertation
submitted in partial fulfillment of the
requirements for the degree of

Doctor of Philosophy

University of Washington

2021

Reading Committee:

Kai-Mei C. Fu, Chair

Boris Blinov

Lukasz Fidkowski

Program Authorized to Offer Degree:
Physics

University of Washington

Abstract

Shallow Donor Qubits in ZnO Nanowires
for Quantum Applications

Maria Leena Kyllikki Viitaniemi

Chair of the Supervisory Committee:
Professor Kai-Mei C. Fu
Physics Department

Donors in ZnO are a promising candidate for quantum network-based quantum technologies with narrow optical lines (7-20 GHz), efficient spin-to-photon transfer (∼90% zero-phonon line efficiency), and long spin coherence times (50 µs Hahn spin-echo T_2) demonstrated in ensembles in bulk [58]. Two outstanding challenges for this system include the isolation of single donor defects and the incorporation of these donors into nanostructures. In this thesis, we utilize ZnO nanowires to address these challenges. We begin by testing several methods of single nanowire isolation, including scanning optical microscopy of ZnO/GaN samples, ion beam milling, exfoliation, and dropcasting. After identifying the most promising methods, favorable optical and spin properties are confirmed to be retained in single ZnO nanowires. Photoluminescence excitation spectroscopy confirms narrow linewidths, optical pumping demonstrates spin initialization, and coherent population trapping is used to prepare a coherent spin state. Finally, two non-standard growth recipes are used to try to address the strain caused by the current method of single nanowire isolation and the large observed surface exciton. In conclusion, by isolating small ensembles of donors using nanowires and showing that these donors can be incorporated into nanostructures, this thesis shows that shallow donors in ZnO have great promise toward use in future quantum technologies.

TABLE OF CONTENTS

Page

LIST OF FIGURES

GLOSSARY

AFM: Atomic Force Microscopy

CPT: Coherent Population Trapping

FDTD: Finite Difference Time Domain simulation

FIB: Focused Ion Beam

FWHM: Full Width at Half Maximum

LO-PHONON REPLICA: Longitudinal Optical Phonon Replicas

MOCVD: Metal Organic Chemical Vapor Deposition

NA: Numerical Aperture

OP: Optical Pumping

PL: Photoluminescence

PLE: Photoluminescence Excitation Spectroscopy

SEM: Scanning Electron Micrograph

SX: Surface Exciton

TES: Two-Electron Satellite Transitions

ACKNOWLEDGMENTS

Behind every graduate student there is a huge team of people without each of whom nothing would get done. Here I hope to thank just a fraction of the people who have supported me on this journey.

First and foremost, I would like to thank my advisor Kai-Mei Fu. They truly care about their students and do everything in their power to help us be successful. From late nights in lab fixing equipment to group meeting presentations full of tough love to lab retreats that bring us together, Kai-Mei has been a wonderful advisor and I appreciate all the work that they put into keeping this group running.

Additionally, this department has many other fantastic professors. In particular, I would like to thank my reading committee, Boris Blinov and Lukasz Fidkowski, and the remaining members of my supervisory committee, Xiaodong Xu, Daniel Gamelin, and Josh Vaughan. Thank you for all of your feedback and genuine interest in my scientific work.

A special thank you goes to Simon Watkins and his group at Simon Fraser University. I was very lucky to get the chance to visit them for a month. He and his students, Chris and Abbas, took me in and taught me how to grow and characterize ZnO nanowires. And once I was back in Seattle, Simon has always been happy to hop on a zoom call and chat about what might be going on with our samples.

The Fu lab is full of the best labmates anyone could ask for. When I first joined, Todd Karin, Ed Kleinsasser, and Cameron Johnson had endless patience to answer my questions about optics and being a scientist. Xiayu Linpeng was the voice of reason to my excitement. We got through many near catastrophes and late nights in lab together. Emma Schmidgall has been a wonderful mentor, showing me that there are many paths to become a great woman in the sciences. Srivatsa Chakravarthi, Vasilis Niaouris, Zeeshawn Kazi, Christian Pederson, Alan Logan, Xingyi Wang, and Lauren Gagnon have learned and struggled with

me so much over the years. They are always happy to get together and chat over coffee, beer, or boba. Chris Zimmermann has been vitally important in helping me get through these last few sets of measurements by assisting with experiments, figures, and motivation. Finally, thank you to all of the other labmates who have been so supportive and made this lab a great place to work in: Sam D'Ambrosia, Lilli Thiel, Nicholas Yama, Roxana Wedowski, Isaiah Kim, Mike Gould, Ian Christen, Andrew Ivanov, Thalya Paleologu, Berit Syltebo, Kendall Crane, Daniel Letzler, Kaitlyn Fong, and everyone else whom has passed through!

Whenever I venture outside of my lab, there are yet more people on campus who have played important roles in the successful completion of my doctorate. Many physics graduate students in the basement and third floor have helped me learn countless pieces of equipment and prepare several samples. I couldn't have done it without you. The physics building staff in the office, machine shop, and all around the building have been essential for getting equipment ordered, parts machined, keeping the building running and clean, getting us paid, and keeping us going. You don't get enough credit for all the work that you do. Staff in other UW departments and buildings have also been essential for the work presented here and for my success. These include the Molecular Analysis Facility, the Washington Nanofabrication Facility, and the Clean Energy Institute.

In addition to help directly with science, my network of emotional support is irreplaceable. My dear friend Jenni Lilleholm has been there for me since the first day that I moved to Seattle. Through lasagna and gravy, she's always had my back. I was also very lucky to have a cohort full of wonderful classmates who made many of the days in Seattle slightly less gray and slightly more full of nachos and hot pot. Additionally, the Physicists for Inclusion and Equity were a fantastic group of students who cared about making this department a better place for current and future physicists. Moreover, my non-physicist friends were essential for keeping me sane. The friends I initially met at the UW Tango Club have been some of the most supportive, interesting, and fun-loving people I've met in Seattle. I also must thank my knitting-circle friends, who are always happy to lend an ear or provide a

distraction. Finally, I can't forget the friends that have been supportive even from across the country or globe. Kira Pendleton and Miia Rantala you have always believed in me!

Taking a step into the past, I'm also very thankful for my first academic mentors. They saw the scientist in me and helped bring her out. At Atlantic High School, Mr. Finklestein and Mr. Will had more patience and encouraging words than anyone would believe. Then at the University of Florida, Amlan Biswas, Sleman Hershfield, and Heather Ray taught me what it meant to be a physicist.

I've saved the most important for the end. My family members have been my rocks. My husband Tommy Wei encouraged me to keep going, even when I was ready to quit. He has also always been happy to pick up the slack when experiments or papers have kept me working at all hours. My parents Sari and Jari Viitaniemi have put more energy into helping their children succeed than anyone else. Their endless work ethic has been a constant source of inspiration and I'm so thankful for their unwavering support. Lastly, my little brother Nikolas Viitaniemi has always been my number one cheerleader. As everyone knows, I'm constantly bragging about how he will take the time to update me about his life and offer encouraging words.

I'm certain that I've left people out, so thank you to everyone that has helped me get here that I didn't already mention. And last but not least, thank you reader. You make writing this thesis worth it.

Chapter 1

INTRODUCTION

1.1 Quantum network-based quantum technologies

Quantum technologies have the potential to drastically change computation and communication. Quantum computers would allow us to solve problems that are currently intractable on classical computers [5, 124, 103]. For example, because molecules are themselves quantum systems, quantum computers have the potential to efficiently simulate these systems [54, 73]. This ability to model large molecules would allow scientists to solve challenges such as designing proteins for medical applications [69, 4] and understand processes such as nitrogen fixation for agriculture [86]. Furthermore, a quantum algorithm written by Shor can be used to factor large numbers [97] and would essentially break current encryption technologies. Conversely, quantum communication and quantum encryption give us the ability to securely distribute communications keys and check for potential eavesdroppers [9, 98].

The fundamental building block of quantum information technologies is the quantum bit (qubit). Similar to a classical bit, the qubit can be in a $|0\rangle$ or a $|1\rangle$ state. However, the qubit can also be in any linear superposition of these states [75],

$$|\Psi_{qubit}\rangle = \alpha\,|0\rangle + \beta\,|1\rangle, \tag{1.1}$$

with $|\alpha|^2 + |\beta|^2 = 1$. In this thesis, we will be discussing one path toward experimentally realizing a qubit with favorable properties for use in quantum technologies based on quantum networks.

Quantum networks provide a way to realize quantum communication and measurement-based quantum computation. As shown in Fig. 1.1(a), a quantum network is made up of quantum nodes, each containing one or more qubits. These quantum nodes are connected using quantum channels [47]. The simplest quantum network is a two node network with one quantum channel. One way to realize a quantum network is using electron or hole spins

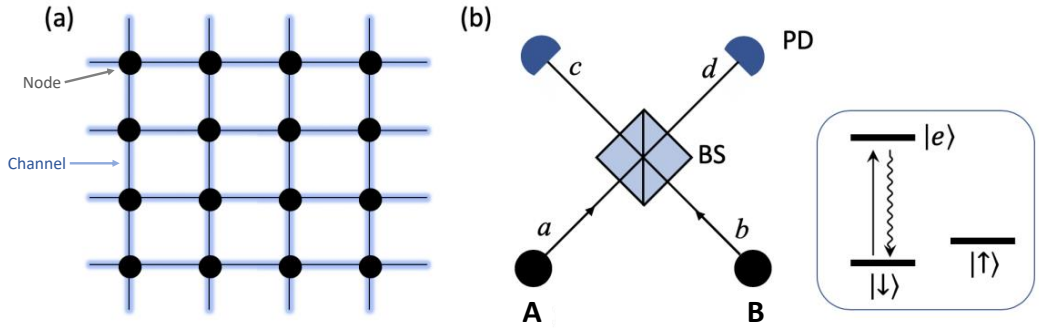

Figure 1.1: (a) Illustration of a 2D quantum network. (b) A protocol for heralded photon entanglement generation of a two-node network based on photon interference. BS: beam splitter. PD: photodiode. Reproduced from [59].

bound to defects in solid state materials. In this example, individual defect spins $(|\uparrow\rangle, |\downarrow\rangle)$ are the qubits $(|0\rangle, |1\rangle)$ and the quantum channel is generated by entanglement utilizing emitted photons [8, 112]. Specifically, entanglement can be generated using the protocol described below and shown in Fig. 1.1(b). We consider a defect with an energetic structure shown in the inset. First, we prepare each of the defect spins in equal superposition states giving the total quantum state

$$|\Psi\rangle = \left(\frac{1}{\sqrt{2}}(|\uparrow\rangle_A + |\downarrow\rangle_A) \otimes \frac{1}{\sqrt{2}}(|\uparrow\rangle_B + |\downarrow\rangle_B)\right) \otimes |vac\rangle\,,$$

where the subscripts (A, B) indicate distinct defects. By applying a resonant laser pulse on the $|\downarrow\rangle \Leftrightarrow |e\rangle$ transition, the $|\downarrow\rangle$ states are excited,

$$|\Psi\rangle = \left(\frac{1}{\sqrt{2}}(|\uparrow\rangle_A + |e\rangle_A) \otimes \frac{1}{\sqrt{2}}(|\uparrow\rangle_B + |e\rangle_B)\right) \otimes |vac\rangle\,.$$

After approximately the lifetime of the excited state $|e\rangle$, a photon is emitted giving

$$|\Psi\rangle = \left(\frac{1}{\sqrt{2}}(|\uparrow\rangle_A + |\downarrow\rangle_A\, a^\dagger) \otimes \frac{1}{\sqrt{2}}(|\uparrow\rangle_B + |\downarrow\rangle_B\, b^\dagger)\right) \otimes |vac\rangle\,,$$

where $a^\dagger$ $(b^\dagger)$ is the operator that indicates a photon along path a (b). Interaction of the photons at the beam splitter (BS) erases the which-path information by giving each photon

equal probability of travelling along path c or d. This gives us the following state:

$$\begin{aligned}
|\Psi\rangle &= \left(\frac{1}{\sqrt{2}}\left(|\uparrow\rangle_A + |\downarrow\rangle_A \left(\frac{ic^\dagger + d^\dagger}{\sqrt{2}}\right)\right) \otimes \frac{1}{\sqrt{2}}\left(|\uparrow\rangle_B + |\downarrow\rangle_B \left(\frac{c^\dagger + id^\dagger}{\sqrt{2}}\right)\right)\right) \otimes |vac\rangle \\
&= \left(\frac{1}{\sqrt{2}}\left(|\uparrow\rangle_A + \frac{ic^\dagger}{\sqrt{2}}|\downarrow\rangle_A + \frac{d^\dagger}{\sqrt{2}}|\downarrow\rangle_A\right) \otimes \frac{1}{\sqrt{2}}\left(|\uparrow\rangle_B + \frac{c^\dagger}{\sqrt{2}}|\downarrow\rangle_B + \frac{id^\dagger}{\sqrt{2}}|\downarrow\rangle_B\right)\right) \otimes |vac\rangle \\
&= \frac{1}{2}\Bigg(|\uparrow\rangle_A|\uparrow\rangle_B + \frac{|\uparrow\rangle_A|\downarrow\rangle_B + i|\downarrow\rangle_A|\uparrow\rangle_B}{\sqrt{2}}c^\dagger + \\
&\quad \frac{|\downarrow\rangle_A|\uparrow\rangle_B + i|\uparrow\rangle_A|\downarrow\rangle_B}{\sqrt{2}}d^\dagger + \frac{i}{2}|\downarrow\rangle_A|\downarrow\rangle_B(d^\dagger d^\dagger + c^\dagger c^\dagger)\Bigg) \otimes |vac\rangle
\end{aligned}$$

If we consider an ideal system without loss and with the ability to count every photon, we can consider cases where only one photon is measured. This case leaves us in a state that has maximal entanglement between our two spin qubits. If the photon was detected along path d, this state would be

$$|\Psi\rangle = \frac{1}{\sqrt{2}}\left(|\uparrow\rangle_A|\downarrow\rangle_B + i|\downarrow\rangle_A|\uparrow\rangle_B\right). \tag{1.2}$$

In other words, we have created a two node quantum network consisting of two spin qubits and one entanglement channel.

Considering the entanglement protocol just described, we can see several key qualities needed for a useful qubit system. First, qubits must be individually addressable and identical. Without identical qubits, identical photons will not be emitted, the which-path information will not be erased, and entanglement will not be generated. For efficient qubit systems, qubits must have efficient spin to photon transfer. As well as allowing for entanglement generation, photons are the clear choice for long distance distribution of quantum information [6, 121, 56]. Furthermore, quantum protocols require us to have the ability to coherently control the spin state and put it into an arbitrary superposition. Finally, for useful quantum computations, qubits need to have a long spin coherence time. The coherence time determines how long information can be stored in a qubit and the amount of time available to perform qubit operations. In the next section, based on these qualities, we will discuss the merits and limitations of various qubit systems.

1.2 Defects in semiconductors for quantum applications

There are several different platforms that meet the criteria described above for measurement-based quantum protocols. Some of the best studied quantum platforms include superconducting circuits, all photonic platforms, trapped ions, and defects in semiconductors. Each of these platforms has advantages and disadvantages. For example, superconducting circuits exhibit the strongest photon-qubit interaction and boast some of the shortest gate times; however, they are easily coupled to the environment resulting in a T_2 time to-date of only 300 µs [81] and they must be used inside a dilution refrigerator. Additionally, superconducting qubits require much additional infrastructure [55] to connect to optical photons, the natural flying qubit, prohibiting the transfer of quantum information over long distances. Regardless, several demonstrations of (potential) quantum advantages have been shown [5, 119]. All photonic quantum computers have a clear connection to optical photons, work at room temperature, and have demonstrated a quantum advantage [124]; however, as current systems have been built out of macroscopic optics, they face technological challenges related to scalability and programmability. In contrast to both superconducting qubits and all photonic quantum platforms, trapped ions have coherence times estimated to be over 1.5 hours [113] and have demonstrated a fault-tolerant logical qubit made from just 13 physical qubits [22]. Additionally, the optical transitions of trapped ions allow for coupling to photons; albeit with relatively slow gate times [12] and scalability challenges related to the ultra-high vacuum environment and ultra-low trapped ion temperatures [80]. Alternatively, using semiconductors as a host material for ions (i.e. defects in semiconductors) may allow us to utilize decades of materials and photonics research to speed-up scalability. Additionally, many defects are coupled to photons and several boast long coherence times [122]. However, the challenge is that while several *different* defects have demonstrated *some* of the properties required for the efficient generation of quantum networks, no defect has demonstrated *all* of these properties. While different quantum applications will likely require the use of different quantum platforms (i.e. hybrid quantum systems using all the technologies described above), this thesis will focus on defects in semiconductors.

Silicon is a natural choice as a host material, because its use in classical computing

electronics has led to decades of advancements in material quality and device integration. Promisingly, donors in isotope-purified silicon boast coherence times greater than seconds, some of the longest coherence times of any semiconductor defect [107, 91]. Single-quantum gate fidelities of greater than 99.9% have been shown for both the electron and nuclear spin [68]. Additionally, extensive research has been conducted on the nanoscale positioning of single donors which allows for local-interaction based gates (i.e. gates without the use of photons) [114, 64, 35, 24]. However, due to silicon's indirect band gap, it does not have efficient optical transitions. Thus, the development of quantum networks using photon-mediated entanglement and many quantum communication protocols will be challenging, if not impossible.

Nitrogen-vacancy (NV) centers in diamond are a leading candidate for photon-based quantum information protocols [92, 19]. Unlike shallow donors in ZnO, they are deep-level defects. While two-node and three-node networks having been demonstrated in this system [82, 40, 20], this achievement is the result of great engineering efforts to build nanophotonic devices to improve the NV centers optical properties [95, 31, 30, 14, 94]. The fundamental challenges of optical inhomogeneity, spectral diffusion, slow network generation rates, and low zero-phonon radiative efficiency [95] make searching for other defects a favorable option.

Donors, acceptors, and quantum dots in III-V materials, such as GaAs, have more favorable optical properties than the above discussed qubit candidates. Efficient optical transitions, spin control, and spin read-out have been shown utilizing both electron spins [28, 26, 15, 27, 84, 49, 25, 45] and hole spins [13, 83, 120, 33, 61, 59]. Two-node networks with kHz generation rates have even been demonstrated in positively charged quantum dots [17]. However, quantum dots suffer from poor optical homogeneity between qubits. Donors and acceptors in bulk III-V materials are more homogeneous, but their inhomogeneous dephasing times (T_2^*) are limited to $\sim$2 ns in electron spins [27] and $\sim$7 ns in hole spins [61]. These short T_2^* times are limited by the hyperfine interactions of the qubit spins with the host nuclear spins. This short T_2^* motivates moving toward materials with spin-free host lattices with the possibility of isotope purification, such as II-VI semiconductors.

1.3 Donor qubits in ZnO for quantum applications

Donors in ZnO combine many of the favorable properties of the different qubit systems described above. While not as prevalent as silicon, ZnO has been used in semiconductor manufacturing [43]. Optical homogeneity has been verified with photoluminescence excitation spectroscopy (PLE) linewidths as narrow as 7 GHz in our best samples. Huang-Rhys parameters of less than 0.1 [110] indicate high radiative efficiency into the zero-phonon line. We have shown all-optical coherent control for small-angle spin rotations [58] with work being done for full-angle microwave spin control. Long longitudinal spin relaxation (T_1) times up to 500 ms have been verified [74]. Additionally, in non-isotope purified ZnO, we have measured inhomogeneous dephasing times (T_2^*) of 17±2 ns and Hahn-spin-echo dephasing times (T_2) times of 50±13 µs [58]. These are comparable to dephasing times in natural silicon, which once isotope purified increased to seconds [107, 91].

Many of the criteria for the creation of quantum networks in the donor in ZnO platform have a clear pathway forward. An outstanding challenge, however, is the ability to individually address qubits. All previous measurements have been performed on bulk ZnO single-crystal substrates with donor concentrations on the order of 10^{16} cm^{-3}. In our ∼1 µm diameter laser spot, this corresponds to ensembles of ∼10,000 donors. While this makes the measured coherence times even more impressive, it leaves us with a challenge: How to optically address just one donor?

For future applications, a combination of two approaches will be necessary. (1) Reducing the concentration of defects with either purer materials or less prevalent defects. (2) Reducing the volume of material within the measurement spot. This thesis will address the second approach. Chapter 2 begins with a description of our two types of as-grown samples, bulk ZnO and ZnO nanowire ensembles. Chapter 3 then discusses the various methods attempted for the isolation of single nanowires. Chapter 4 presents results demonstrating the optical homogeneity and spin coherence of donors in isolated single nanowires. Chapter 5 describes two non-standard growth attempts. The aim of these growths was growth-based nanowire isolation and reduction of the unfavorable surface exciton. Finally, chapter 6 will provide a summary and describe the next steps for reducing defect density and moving

toward quantum applications.

Chapter 2

SHALLOW DONORS IN ZNO SINGLE CRYSTALS AND ZNO NANOWIRES

2.1 Introduction

ZnO can be grown in different ways leading to different morphologies. Each morphology has benefits and drawbacks. Throughout this thesis, we focus on two different types: bulk ZnO and ZnO nanowires. We expect donors embedded in single-crystal bulk materials to have more uniform optical properties than donors in nanostructures. This is because the surfaces of nanostructures are often sources of electric field noise, band bending [102], and strain. However, most quantum applications will require the use of defects coupled to nanophotonics for scalable, on-chip devices [94, 31]. ZnO nanowires provide an opportunity to study the fundamental behavior of donors in nanostructures, as well as a potential avenue for device integration. Nanowires also allow for the near-term isolation of smaller ensembles of donors, a stepping-stone on the way toward single donor isolation.

In Sect. 2.2, we will begin with a physical description of the as-grown samples that we study as well as a brief description of the cryogenic systems used for measurements. Then in Sect. 2.3, the photoluminescence (PL) properties of neutral donors (D^0) are discussed. Sect. 2.4 looks at the energetic structure of the D^0 system in a magnetic field. It is this energetic structure that allows us to utilize donors for quantum information applications. To precisely describe the energetic structure, the g-factor of the donors must be accurately known. Therefore, in Sect. 2.5, PL measurements are utilized to measure the g-factors of various donors and experimental geometries.

2.2 Physical Description and Experimental Set-up

ZnO is a II-VI semiconductor where Zn and O typically crystallize into a hexagonal wurtzite structure. Our bulk samples are hydrothermally grown by Tokyo Denpa (Fig. 2.1(a,b)). The

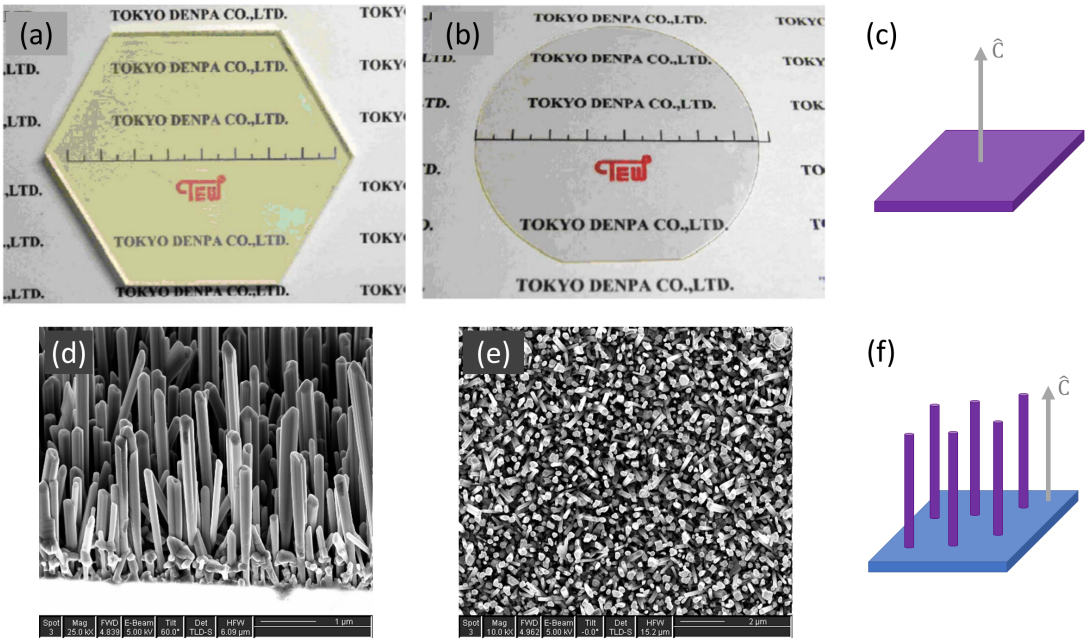

Figure 2.1: Bulk ZnO: (a) 3-inch ZnO crystal, (b) 3-inch (0001) ZnO wafer after polishing by Tokyo Denpa. Scale bar is 80 mm. (a) and (b) reproduced from [7]. (c) Diagram of the bulk crystal showing the c-axis perpendicular to the sample surface.
ZnO Nanowires: SEM of ZnO nanowire samples grown by Simon Watkins' group at Simon Fraser University. Image taken at (d) a 60° angle with a 1 µm scale bar and (e) directly from the top with a 2 µm scale bar. (f) Diagram of the ZnO nanowires (purple) grown on a sapphire substrate (blue) with the c-axis parallel to the long edge of the nanowire.

crystal c-axis [0001] is perpendicular to the surface of the sample (Fig. 2.1(c)). The total donor concentration of all species is on the order of $10^{17}\,\mathrm{cm}^{-3}$, determined by capacitance-voltage measurements [72]; however, the concentrations of individual donor species will be lower.

The ZnO nanowire samples are grown by Simon Watkins' group at Simon Fraser University. They are grown on a c-plane sapphire (0001) substrate via metal organic chemical vapor deposition (MOCVD) as described in Ch. 5. Nanowires are typically 100-200 nm in diameter, 1-4 µm long, and grow in a dense ensemble. Scanning electron micrograph (SEM) images of the nanowire ensemble are shown in Fig. 2.1(d,e). The ZnO crystal c-axis [0001] points along the long axis of the nanowire (Fig. 2.1(f)). The In donor concentration is

estimated to have an upper limit of 10^{16} cm^{-3} from nanoprobe resistivity measurements on similar samples.

All optical measurements are performed in one of two cryogenic systems. The primary system is a helium immersion cryostat with a superconducting magnet. The optical access is through one of four windows and the optical axis can be either parallel or perpendicular to the magnetic field. For measurements at less than 2.1 K, the sample is immersed in superfluid He. For other low-temperature measurements, the sample is in He gas. The secondary system is a cold-finger cryostat with optical access. For this system, the sample is in vacuum. For all measurements, the optical axis is defined as $\hat{k}$ and is parallel to the excitation laser Poynting vector. In both systems, the laser is focused to ∼1 µm in diameter (see Ch. 3 for details).

2.3 Donor Identification

The energy level diagram of the D^0 system at 0 T is shown in Fig. 2.2(a). When the system is excited with energy higher than the band gap of ZnO, excitons may bind to the donor to form the donor-bound exciton (D^0X) state. The formation of the D^0X state is also possible with resonant excitation. After approximately the radiative lifetime of the donor (∼1 ns [110]), the system will relax back to the D^0 state and emit a photon. Fig. 2.2(b) shows a photoluminescence (PL) spectrum of the bulk sample, while Fig. 2.3 shows spectra of several nanowire samples. In each, the D^0X lines for Ga, Al, and/or In are clearly resolved at 3.3599 eV, 3.3607 eV, and/or 3.3567 eV, respectively [67]. The peak around 3.376 eV, labeled FX, is one of the free exciton lines [67]. The feature at 3.333 eV is assigned to the Y line and has been attributed to excitons bound to local defects (i.e. dislocations) [67]. In some of the nanowire samples, a broad surface exciton feature (SX) is present. The surface exciton is a power-dependent band related to surface defects [106, 117] that can overlap the D^0X lines and affect our ability to detect and address the D^0X lines (see Sect. 5.4 for further discussion of the surface exciton).

In addition to direct transitions, the system may relax via several lower-energy paths (Fig. 2.2(a)). For example, the longitudinal-optical (LO) phonon replicas involve the emission of one or more phonons in addition to a photon. The two electron satellite (TES)

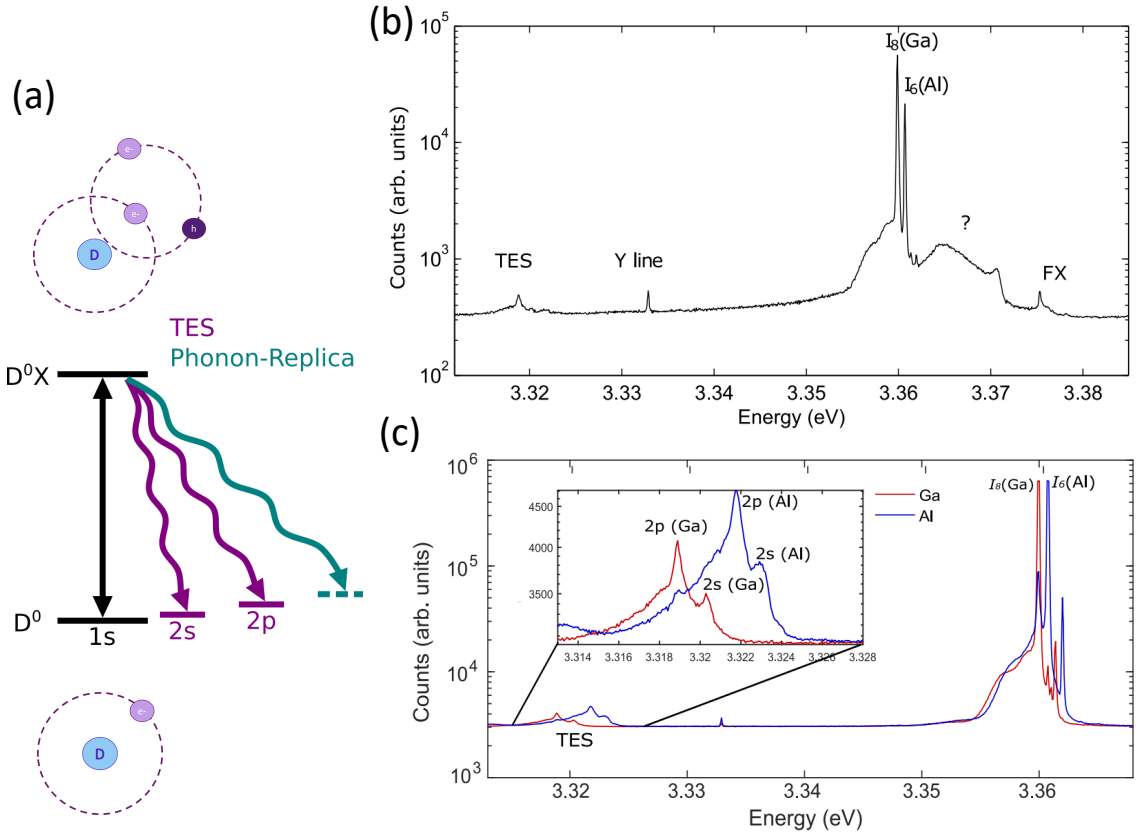

Figure 2.2: (a) Energy level diagram of the D^0 system at 0 T. The low-energy TES/LO-phonon replica transitions are shown. (b) Log-scale PL spectra of a bulk ZnO sample at 0 T, 1.5 K. Excitation laser is at ~3.4 eV and <170 nW with a spot size of 1 µm. (c) Log-scale resonant PL spectra of a bulk ZnO sample at 0 T, 1.5 K. Excitation laser is resonantly exciting the Ga (red) or Al (blue) main donor-bound exciton transition. The inset shows the enhancement of the two-electron satellite peaks compared to the non-resonant case in (b). Line identification is based on Ref. [67]. (b,c) are reproduced from the supporting information for [58].

transitions are the relaxation of the system to an excited hydrogenic orbital (i.e. 2s or 2p orbital states) [67]. Because the emission from these lower-energy transitions are proportional to how resonant the excitation laser is on the direct D^0-D^0X transition, they are a useful tool to confirm the identification of the D^0X lines. Fig. 2.2(c) shows the enhancement of the TES and LO-phonon replicas under resonant excitation of their corresponding D^0X lines, as compared to the off-resonant spectra shown in Fig. 2.2(b). The Ga (Al) TES/LO-

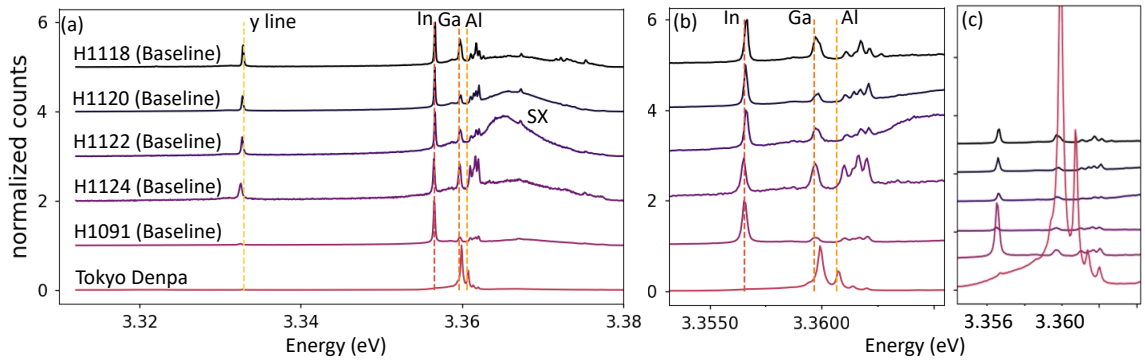

Figure 2.3: PL spectra of a bulk (Tokyo Denpa) sample and several nanowire ensemble samples. (a) The data are normalized to the max counts for ease of comparison of the relative intensities of different features. (b) The same as (a), but zoomed in to ease the comparison of spectral shapes of the D^0X lines. (c) The non-normalized data is shown for the comparison of overall intensities.

phonon replicas are enhanced when the excitation laser is resonant on the Ga (Al) D^0X transition energy.

Fig. 2.3 shows spectra from several samples that were taken with the same measurement conditions to screen the nanowire samples from different growth rounds for promising PL features. These measurements were performed with a spot size approximately a hundred times larger than our typical $\sim$1 µm laser spot; therefore, we are probing hundreds of nanowires simultaneously. All of the samples shown here contain In, Ga, and/or Al D^0X lines; however, as shown in Fig. 2.3(a), their intensities relative to other features vary. For example, the SX is nearly non-existent in sample H1091, but as tall as the In D^0X line in sample H1122. Additionally, the linewidth of the D^0X lines can vary between samples. Notably, most of the samples shown here have spectrometer-resolution-limited D^0X linewidths, indicating high crystal quality and minimal strain. Moreover, the overall brightness of the samples is compared in Fig. 2.3(c); brighter samples are more favorable because of shorter measurement times, but less favorable because of likely increased donor concentrations. Finally, considering all of these factors (relative feature intensity, linewidth, and overall intensity) we choose the samples which are the most promising to study. For example, from this batch of nanowire samples we begin by studying H1091 and H1118, because of their

high In D^0X intensity and small SX feature. We perform similar screenings on older batches of nanowires after using these nanowires for testing isolation methods (Ch. 3).

2.4 Energetic Structure

In order to utilize donors for quantum applications, the spin degeneracy of the D^0 and D^0X states must be lifted. A magnetic field lifts the spin degeneracy of the D^0 (D^0X) state due to the electron (hole) Zeeman effect [18, 111]. The splitting of the excited state is solely determined by the hole g-factor (g_h), because the two excited-state electrons form a spin singlet. The electron g-factor (g_e) is highly isotropic, while g_h depends on the orientation of the magnetic field with respect to the crystal c-axis. For $\vec{B} \perp \hat{c}$, $g_h > 0$. For $\vec{B} \parallel \hat{c}$, $g_h < 0$. These energy-level splittings leads to four direct D^0-D^0X transitions, where the polarization rules are determined by the orientation of the magnetic field with respect to the crystal c-axis. As shown in Fig. 2.4(a,b), we define the crystal c-axis to be parallel to $\hat{z}$ ($\hat{c} \parallel \hat{z}$) and the magnetic field to be in the xz-plane ($\vec{B} \perp \hat{y}$). Fig. 2.4(b) shows a diagram of the energy level structures with a magnetic field applied perpendicular to the crystal axis ($\vec{B} \perp \hat{c}$) and a magnetic field applied parallel to the crystal axis ($\vec{B} \parallel \hat{c}$). A derivation of the polarization rules is shown in Appendix A. Experimental considerations related to polarization are discussed in Sect. 3.6. $\sigma^{\pm}$ is defined as $\hat{x} \mp i\hat{y}$. Transitions with $\hat{z}$-polarized light are approximately two orders of magnitude weaker than other transitions. The polarization rules are slightly relaxed when coupling into the end of a nanowire.

In high-quality samples, the Zeeman splitting and polarization rules are clearly visible in photoluminescence (PL) spectra; however, the measurement geometry affects which polarizations are accessible. Only light polarized perpendicular to the optical axis ($\hat{k}$) can be observed. Fig. 2.4(c) shows several PL spectra of bulk ZnO at different magnetic fields. At 0 T, two peaks, corresponding to Ga and Al D^0X lines, are visible. The optical axis is perpendicular to the sample surface ($\hat{k} \parallel \hat{c}$) for all spectra. With $\vec{B} \perp \hat{c}$, four peaks are visible for each donor, corresponding to $\hat{x}$ and $\hat{y}$ polarized light. For each donor, there are two pairs of peaks; the large splitting between each pair of peaks is the result of the electron Zeeman effect. The small splitting between the two different polarizations is the result of the hole Zeeman effect. With $\vec{B} \parallel \hat{c}$, only two peaks are visible for each donor; this

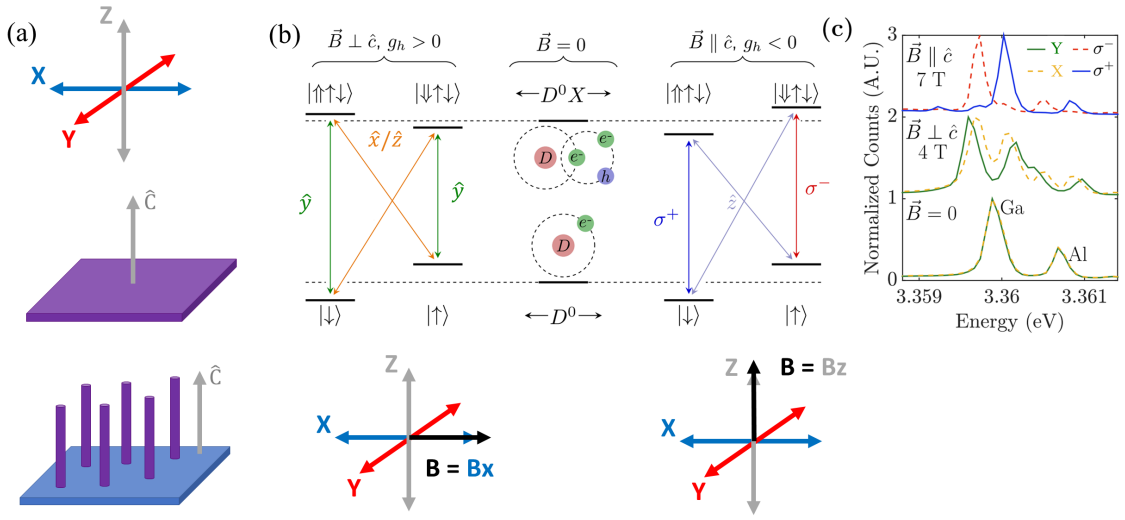

Figure 2.4: (a) Diagrams showing the Cartesian axes defined for the bulk sample and the nanowire sample. We define the crystal c-axis to be parallel to $\hat{z}$ ($\hat{c} \parallel \hat{z}$) and the magnetic field to be in the xz-plane ($\vec{B} \perp \hat{y}$). (b) Energy diagram of the shallow donor system in Voigt geometry (left), no magnetic field (middle), and Faraday geometry (right). $|\Uparrow\rangle(|\uparrow\rangle)$ denotes the hole (electron) spin. The magnetic field orientation is depicted on the Cartesian coordinate system below the respective energy level diagram. (c) From bottom to top, PL spectra at 0 T and 5.2 K, 4 T and 5.2 K with $\vec{B} \perp \hat{c}$, and 7 T and 1.5 K with $\vec{B} \parallel \hat{c}$. The excitation laser was at 3.45 eV.

is because the $\hat{z}$ transitions are weak and not visible with $\hat{k} \parallel \hat{z}$. In Sect. 2.5, we will use PL spectra to measure the electron and hole g-factors.

2.5 g-factor measurements

The electron and hole g-factors determine the D^0 and D^0X splittings under magnetic field; therefore, for a complete understanding of the donor energetic structure, it is essential for us to have accurate measurements of the g-factor for each type of donor and experimental geometry. By measuring the energy splittings of the ground and excited states as a function of magnetic field (i.e. Zeeman energy), we are able to obtain the electron and hole g-factors for several samples. In these experiments, photoluminescence (PL) measurements were performed using laser excitation higher in energy than our D^0X transition of interest. The

energy splittings are then fit to the linear function

$$\Delta E_{=} g_{\mathrm{i}} \mu_{\mathrm{B}} B, \tag{2.1}$$

where g_{i} is the g-factor in a given geometry, i is either electron or hole, μ_{B} is the Bohr magneton, and B is the applied magnetic field. To get accurate measurements for both the electron and hole g-factors, PL measurements must be performed at different polarizations; see Fig 2.4 for the polarization selection rules. To collect different polarizations, a half-wave plate in the collection and excitation path, in combination with a linear polarizer in the collection path, was used. We assume that the polarization of the off-resonant excitation has no major effect, and that the main effect of the half-wave plate in combination with the linear polarizer is to select which transitions are collected.

2.5.1 Ga donors in bulk, $\vec{B} \perp \hat{c}$, $\vec{k} \parallel \hat{c}$

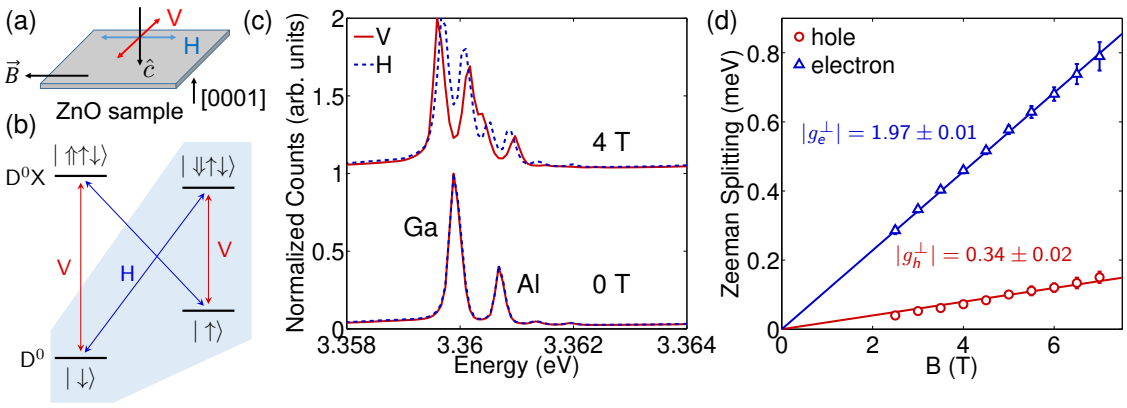

Figure 2.5: (a) Experimental geometry. $\hat{c}$ is the optical propagation axis. $\vec{B}$ is the magnetic field. H and V correspond to $\hat{x}$ and $\hat{y}$, respectively. (b) Energy diagram of the donor system at magnetic field with $\hat{B} \perp \hat{c}$. $|\Uparrow\rangle(|\uparrow\rangle)$ denotes the hole (electron) spin. (c) Spectra at 0 T and 4 T with V and H polarized collection. The excitation laser is at 3.446 eV with vertical polarization. Temperature is 5.5 K. Both the Ga and Al donor peaks split into four different peaks with applied magnetic field. (d) Electron and hole Zeeman splitting of the Ga donor as a function of magnetic field. The red and blue lines are linear fits of the Zeeman splitting. Figure is reproduced from [58].

Fig. 2.5(c) shows a representative PL spectra for the Ga and Al donor in a bulk sample

with $\vec{B} \perp \hat{c}$ and $\vec{k} \parallel \hat{c}$. We measure the g-factor of the Ga donor. For this measurement geometry (Fig. 2.5(a)), H and V correspond to $\hat{x}$ and $\hat{y}$ polarized light, respectively. At 4 T, we are able to see the two distinct pairs of peaks for each polarization. As discussed above, the average separation between these pairs of peaks is caused by the electron Zeeman effect, while the splitting between the V and H positions for each peak is caused by the hole Zeeman effect. As shown in Fig. 2.5(d), we are able to fit the splittings to Eq. 2.1. This allows us to measure the in-plane g-factors for the Ga donors in bulk ZnO to be $|g_e^{\perp}| = 1.97$ and $|g_h^{\perp}| = 0.34$ [58]. The measured g-factors are only slightly higher than the reported values in literature for Ga donors in ZnO, $|g_e^{\perp}| = 1.9$ and $|g_h^{\perp}| = 0.25$ [111]. Notably for these samples, the splittings are large enough that we are able to simply use the maximum of the spectra to find the center energy of the transitions with high enough resolution for the fit.

2.5.2 In donors in a nanowire ensembles, $\vec{B} \perp \hat{c}$, $\vec{k} \parallel \hat{c}$

For nanowire ensembles, we perform measurements with $\vec{B} \perp \hat{c}$ and $\vec{k} \parallel \hat{c}$. V and H correspond to $\hat{x}$ and $\hat{y}$ polarized light, respectively (inset of Fig. 2.6(a)). For In donors in nanowire ensembles, we find that the g-factors are smaller than for Ga donors in bulk ZnO and that the polarization rules are relaxed when coupling into a nanowire; therefore, to estimate the g-factor we modify the above measurement technique as follows. We use a half waveplate to measure the spectra at many different polarization angles (rather than at just the $\hat{x}$ and $\hat{y}$ polarizations) and fit each of the spectra with a Voigt function (a convolution of Gaussian and Lorentzian function). Representative spectra and fits at the maximum and minimum polarizations are shown in Fig. 2.6(a). The relative energies of the maxima of the high and low energy peaks at different polarizations are shown in Fig. 2.6(b). We can then fit the resulting oscillation to a simple model,

$$E_{\mathrm{pos,i}} = E_{\mathrm{center,i}} + \Delta E_{\mathrm{excited,i}} \times \sin\left(a_{\mathrm{i}}\varphi + b_{\mathrm{i}}\right) \quad (\mathrm{i} = \mathrm{low},\ \mathrm{high}), \tag{2.2}$$

where $E_{\mathrm{pos,i}}$ is the position of the low-energy (i = low) or high-energy peak (i = high). $E_{\mathrm{center,i}}$ is the average position of each peak. $\Delta E_{\mathrm{excited,i}}$ is the amplitude of the oscillation of each peak. φ is the angle of the half-wave plate. a_{i} and b_{i} are the frequency and phase

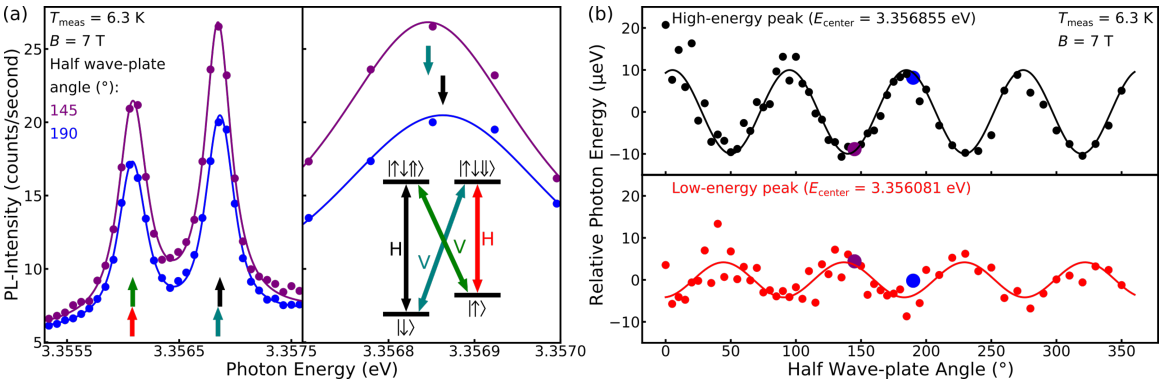

Figure 2.6: Polarization-dependent PL measurements were performed on a nanowire ensemble at 7 T ($\hat{c} \perp \vec{B}$ and $\hat{c} \parallel \hat{k}$) and 6.3 K using laser excitation at 3.4440 eV and 40 nW. (a) PL spectra are shown for two different positions of the half-wave plate. Left panel: Two distinct lines are observed originating from In D^0X transitions involving the split ground-states. The lines are denoted as low-energy and high-energy peak. Right panel: A zoomed-in version of the left panel is shown to demonstrate the shift observed in the high-energy peak for different polarizations; this shift originates from the splitting of the excited state of the In D^0-D^0X system. The arrows indicate the spectral maximums of the transitions shown with the same color. The inset illustrates the different transitions and their polarizations. H (V) stands for horizontally (vertically) polarized light. (b) The relative change in the position of the low- and high-energy peak seen in (a) as a function of the angle of the half-wave plate is displayed. The position of the low- and high-energy feature seen in (a) was determined using a Voigt fit. The data points marked in purple and blue correspond to the spectra displayed in (a). Polarization selectivity is observed. Data is reproduced from the supplementary information of [108].

of the sinusoidal curve. As expected, the period of the oscillation is 90 ° [111]. $E_{\text{center,high}} - E_{\text{center,low}}$ equals the ground-state splitting, and thus

$$E_{\text{center,high}} - E_{\text{center,low}} = g_{\text{e}}^{\perp} \mu_{\text{B}} B. \tag{2.3}$$

With the values stated in Fig. 2.6(b), we obtain a value of 1.91 for $g_{\text{e}}^{\perp}$. $\Delta E_{\text{excited,i}}$ (i = low or high) represents the splitting of the excited state, and thus can be used to calculate the hole g-factor ($g_{\text{h}}^{\perp}$) via

$$\Delta E_{\text{excited,i}} = g_{\text{h}}^{\perp} \mu_{\text{B}} B.$$

From Fig. 2.6(b), it can be seen that $\Delta E_{\text{excited,low}}$ is lower than $\Delta E_{\text{excited,high}}$, indicating that the high energy peak displays better (but not perfect) polarization selectivity. Thus,

$\Delta E_{\text{excited,high}}$ can be used to determine a value of 0.05 as a lower bound for $g_{\text{h}}^{\perp}$. The measured electron and hole g-factors are similar to the values reported in literature for In donors in ZnO, $|g_e^{\perp}| = 1.93$ and $|g_h^{\perp}| = 0.0 - 0.1$ [18, 88]. It is important to note that the hole g-factor for In donors is smaller than that of Ga donors; this fact leads the coherent population trapping dip studied in Sect. 4.4 to be more centered on the reverse spectral hole peak, thus making it easier for us to initially discover the coherent population trapping dip.

2.5.3 In donors in a single dropcast nanowire, $\vec{B} \perp \hat{c}$, $\vec{k} \perp \hat{c}$

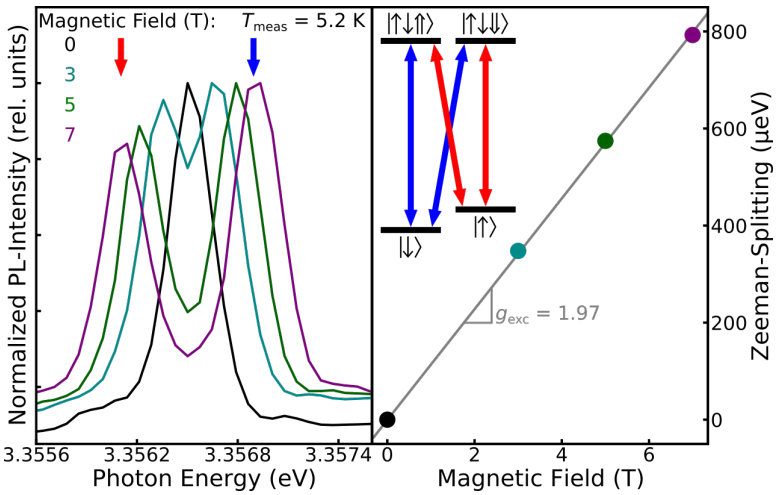

Figure 2.7: Magnetic field-dependent PL spectra of the In D^0X transitions for a single nanowire at 5.2 K, $\hat{B} \perp \hat{c}$, $\vec{k} \perp \hat{c}$. Data are shown at 0 (black), 3 (teal), 5 (green), and 7 T (purple). The right panel shows the Zeeman splitting as a function of magnetic field. The gray line is a fit to the data which yields the sum of the electron and hole g-factors. This figure is reproduced from [108].

In dropcast nanowires (see Sect. 3.5), the optical axis is perpendicular to the crystal c-axis ($\vec{k} \perp \hat{c}$) and $\vec{B} \perp \hat{c}$. As seen in Fig. 2.7, the sum of g_e and $g_h^{\perp}$ is measured to be $g_{tot} = 1.97$. This is consistent with our measured value $g_e = 1.91$ for nanowire ensembles; it can be assumed that $g_e^{\perp} \cong g_e^{\parallel}$ [111]. As described in Sect. 4.4, we use high-resolution PL excitation spectroscopy to further confirm $g_e = 1.90$. With these measurements, we obtain a lower bound for $g_h^{\perp}$ of 0.07. This is consistent with the g-factor measured for ensemble

nanowires, indicating that the dropcasting process and isolation in a single nanowire does not appear to affect the g-factor.

2.5.4 Ga donors in bulk, $\vec{B} \parallel \hat{c}$, $\vec{k} \parallel \hat{c}$

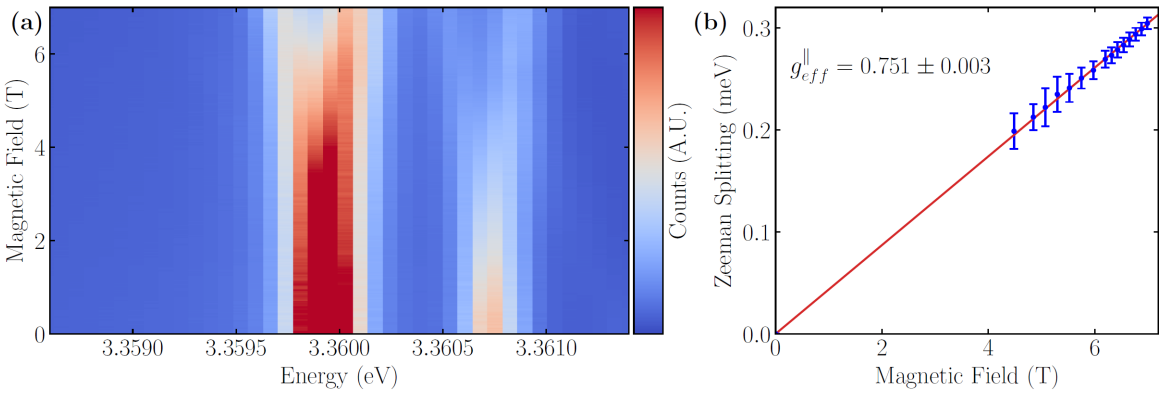

Figure 2.8: (a) Magneto-PL spectra in the Faraday geometry at 5.2 K. The excitation energy is 3.45 eV. The peak near 3.36 eV is the Ga D^0X line. (b) Zeeman splitting of the Ga donor lines as a function of magnetic field. This figure is reproduced from [74].

To determine the hole g-factor with $\vec{k} \parallel \hat{c}$ and $\vec{B} \parallel \hat{c}$, we measure spectra as a function of magnetic field (Fig. 2.8(a)). In this case, the two peaks correspond to the $\sigma+$ and $\sigma-$ transitions (Fig. 2.4). When fitting the separation between these peaks to Eq. 2.1 (Fig. 2.8(b)), the resulting effective g-factor is the difference between the electron and the hole g-factors. If we assume $g_e^{\parallel} \cong g_e^{\perp} = 1.97$ (Sect. 2.5.1 and [111]), we may estimate $g_h^{\parallel} = -1.22 \pm 0.01$, which is in agreement with the literature value of $g_h^{\parallel} = -1.2$ [111].

2.5.5 Summary

In summary, the the electron and hole g-factors have been measured in several samples and in several geometries (Table 2.1). All of our values are consistent with values from the literature [111, 18, 88]. Notably, we find that $g_h^{\perp}$ for In donors in nanowires is smaller than those in Ga donors in bulk samples. This may be due to differences between donors or it may be the result of reduced polarization selectivity when coupling into the end of

a nanowire. In the case of unresolved transitions, imperfections in polarization selectivity lead to decreases in the measured g-factors. However, in the literature, differences in the g-factors of different donors have been observed within the same experimental set-up [18]. Additionally, $|g_h^{\perp}|$ values of 0.1 and 0 have been measured for In [18, 88], while values of 0.25 have been measured in Ga donors [111]. This leads us to believe that at least a portion of the difference in measured $g_h^{\perp}$ is the result of differences between In and Ga donors.

Sample	Magnetic field	Optical axis	g_e	g_h
Ga in bulk	$\vec{B} \perp \hat{c}$	$\vec{k} \parallel \hat{c}$	1.97	0.34
In in ensemble nanowires	$\vec{B} \perp \hat{c}$	$\vec{k} \parallel \hat{c}$	1.91	0.05
In in single nanowire	$\vec{B} \perp \hat{c}$	$\vec{k} \perp \hat{c}$	1.90	0.07
Ga in bulk	$\vec{B} \parallel \hat{c}$	$\vec{k} \parallel \hat{c}$	1.97 (assume)	-1.22

Table 2.1: Electron and hole g-factors for various samples in various geometries.

Chapter 3

SINGLE NANOWIRE ISOLATION

3.1 Introduction

One way to encode quantum information is to use a pair of states within a single qubit, such as the spin states of a donor-bound electron, to encode for $|1\rangle$ / $|0\rangle$. To use this type of encoding scheme requires the isolation of a single qubit. Thus, in addition to understanding the effects of nanostructure integration on shallow donors in ZnO, we also aim to approach the single donor limit by isolating smaller ensembles of donors. To understand how we may approach this goal, we must consider our measurement volume. The measurement volume of our system is determined by the confocal volume of our microscope, the region where the laser intensity is within $1/e^2$ times its maximum. As shown in Fig. 3.1, we estimate this by assuming a 3D Gaussian shape [90]

$$V_c = (\pi/2)^{3/2} r_{xy}^2 r_z = (\pi/2)^{3/2} \kappa r_{xy}^3 \tag{3.1}$$

where r_{xy} is the $1/e^2$ distance in the xy-plane, r_z is the $1/e^2$ distance along the optical axis, and κ is a geometric factor equal to r_z/r_{xy}. κ may be approximated using the Ralyeigh limit [118].

$$\kappa = r_z/r_{xy} = (2n\lambda/\mathrm{NA}^2)(0.61\lambda/\mathrm{NA})^{-1} = 2.33n/\mathrm{NA} \tag{3.2}$$

where NA is the numerical aperture of the microscope objective, λ is the wavelength of light, and n is the index of refraction. Substituting Eq. 3.2 into Eq. 3.1 gives

$$V_c = (\pi/2)^{3/2}(2.33n/\mathrm{NA}) r_{xy}^3. \tag{3.3}$$

In our system, r_{xy} is estimated to be 0.5 µm and the NA is 0.7. n is measured by our group in bulk ZnO via transmission and reflection measurements. At 369 nm, we find $n = 2.7$. Using these parameters, we estimate a confocal volume of 2.2 μm^3. Because our measurements are performed with the laser focused at the sample surface, we divide this number by two.

Therefore, assuming a donor density of $10^{16}\,\mathrm{cm}^{-3}$, we estimate that there are $\sim 10^4$ donors in our measurement volume for bulk samples.

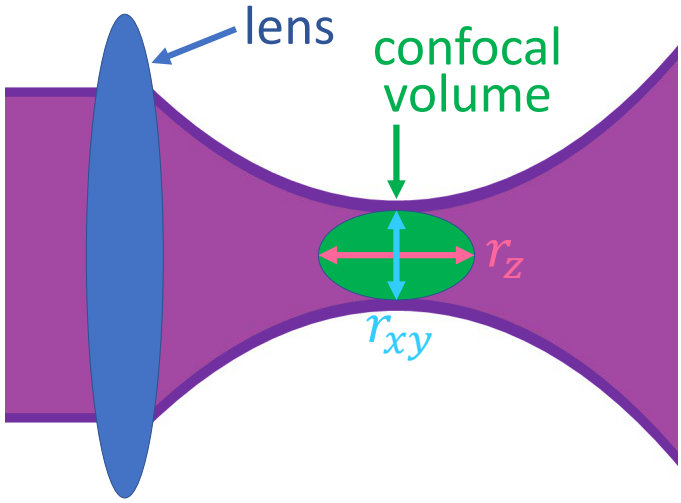

Figure 3.1: Schematic of a focusing laser. The purple area is a cross-section of the laser after passing through a focusing lens. The focusing lens is shown in blue. The green area is a cross-section of the confocal volume, where the laser intensity is within $1/e^2$ times its maximum.

We may reduce the number of donors simultaneously probed by reducing the amount of ZnO within our measurement volume. Our standard nanowire samples are grown on a sapphire substrate and are $1-4\,\mu\mathrm{m}$ tall and 100-200 nm in diameter. Because the nanowires grow densely, these samples can be approximated as a $\sim 2\,\mu\mathrm{m}$-thick thin film. r_z is similar to the height of the nanowires ($\kappa r_{xy}/2 = 2.2\,\mu\mathrm{m}$); therefore, we only marginally reduce the number of donors that we probe by moving from a bulk sample to a standard nanowire sample. However, ZnO nanowires grown on a GaN substrate grow less densely than our standard nanowire samples. Thus, in Sect. 3.2, we utilize a ZnO/GaN sample to reduce the volume of ZnO within our measurement volume. We then further reduce the volume of ZnO probed by isolating a single nanowire. For a single average-sized nanowire with a donor density of $10^{16}\,\mathrm{cm}^{-3}$, we estimate that there are < 400 donors are in our measurement volume. This is nearly two orders of magnitude fewer donors than in our bulk sample measurements!

However, isolating a single nanowire without altering the optical properties of its donors is non-trivial. We begin with standard nanowire samples that have the narrowest and brightest D^0X lines, as described in Sect. 2.3. From these samples, we explored several ways to realize single nanowire isolation. In Sect. 3.3, we used a focused ion beam to mill down all the nanowires around a single nanowire of interest. In Sect. 3.4, nanowires are removed from the substrate by pressing them into indium metal. After this exfoliation process, we can locate areas where nanowires have been removed with a low density. Sect. 3.5 describes the process of sonicating nanowires in ethanol and then dropcasting them onto a substrate. In each section, isolation is first confirmed with scanning electron microscopy (SEM) images. Then the quality of the nanowires is checked by performing photoluminescence (PL) spectroscopy. We find that isolating single nanowires via ion beam milling or exfoliation damages/strains the nanowire of interest; however, using the dropcasting method, we are able to find nanowires in which favorable PL properties have been retained.

3.2 Isolation via Scanning Optical Microscopy

One way to isolate a small volume of material is to perform optical microscopy on a thin sample. In this technique, a laser is focused on the sample while PL is collected from the same spot. The lateral measurement area is determined by the size of the optical spot; for our system, this is typically $\sim$1 µm in diameter. In this section, we consider samples in which the thickness of ZnO is approximately the same as the axial confocal distance of $\sim$2.2 µm of our system.

In the standard nanowire samples grown on a sapphire substrate (Sect. 2.2), there are $\sim$5 nanowires and a floor of partially nucleated ZnO nanostructures within the measurement volume (Fig. 2.1(d,e)). However, it is also possible to grow ZnO nanowires on a GaN substrate; the nanowires grow much less densely in this case (Fig. 3.2(a)). For the ZnO/GaN samples, we expect to optically isolate a floor of nanowalls ($\sim$850 nm tall) and $\sim$1 nanowire ($<$250 nm in diameter and $\sim$2 µm tall). We estimate that we probe ensembles of $< 5 \times 10^3$ donors.

For optical measurements, the ZnO nanostructures are mounted into a He immersion cryostat with an external magnetic field $\vec{B}$ applied such that $\vec{B} \parallel \hat{c}$. This applied mag-

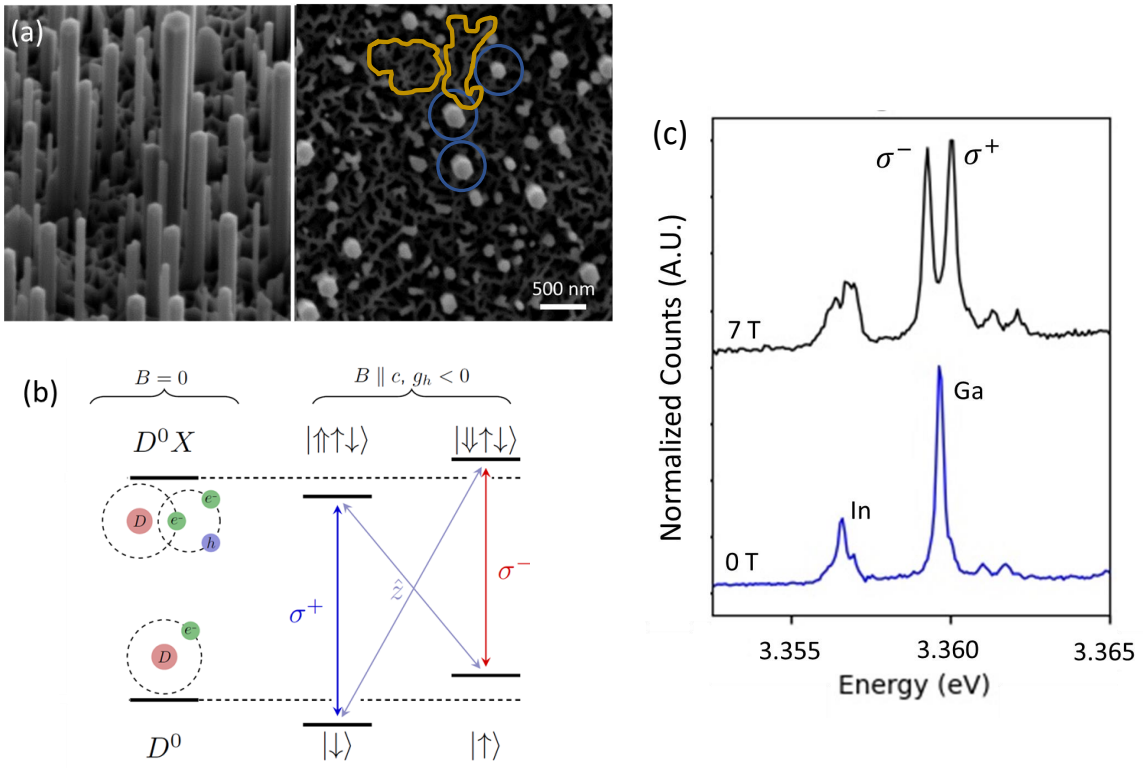

Figure 3.2: (a) SEM image of ZnO nanostructures grown on GaN. ∼1 µm-tall nanowires (blue) and ∼850 nm-tall nanowalls (orange) are visible. This image is taken at a 60° (right) and 0° (left) tilt. (b) Energy diagram of the donor system in Faraday geometry ($\vec{B} \parallel \hat{c}$). (c) PL spectra of the Ga and In D^0X transitions at 5.5 K. In the top spectra, a 7 T magnetic field is applied in Faraday geometry ($\vec{B} \parallel \hat{c}$). Figures reproduced from [109].

netic field splits the donor D^0X transition into $\sigma+$ and $\sigma-$ (Fig. 3.2(b)). The sample is excited with pulsed excitation at ∼3.444 eV and PL spectra are collected at 0 T and 7 T. In Fig 3.2(c), the D^0X transitions for Ga and In donors are observed along with the Zeeman splitting at 7 T. Our ability to observe spectrometer-limited linewidths as well as the electron Zeeman splitting means that we are able to individually address each of the $\sigma+$ and $\sigma-$ transitions. This allows us to use this sample in the studies described in Ch. 4.

Though the PL spectra looked favorable at certain locations, the ZnO/GaN samples did not uniformly exhibit bright, single D^0X lines. In Fig. 3.3, scanning optical microscopy images (also called confocal scans) of different regions on a ZnO/GaN sample are shown.

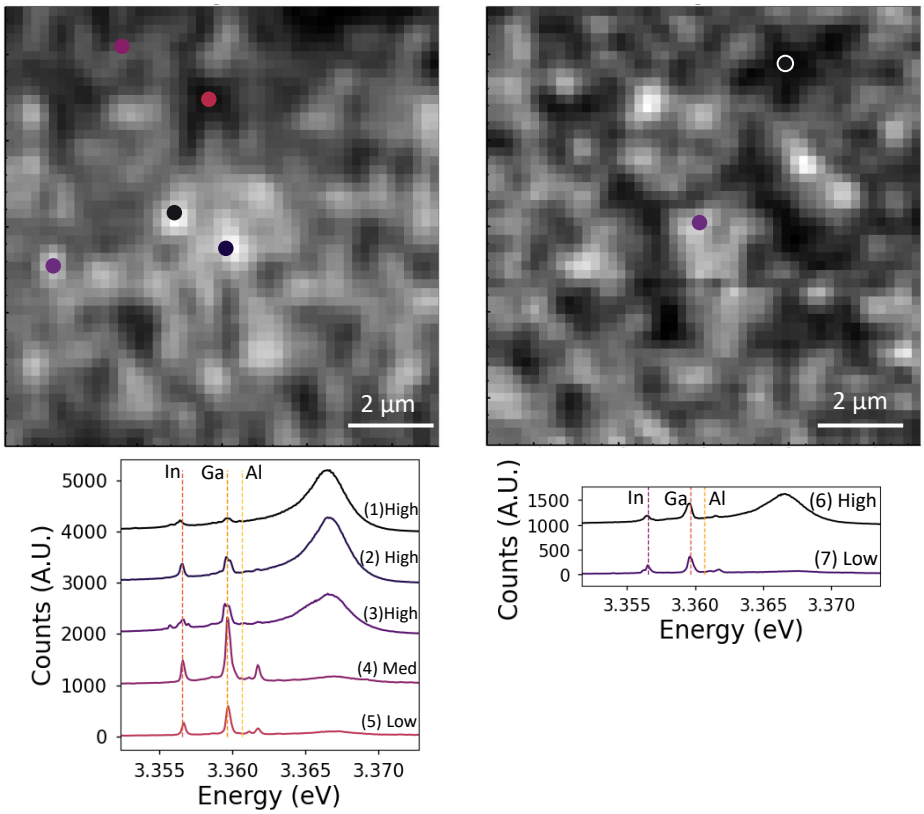

Figure 3.3: Confocal scan with PL from the D^0X spectral region collected while exciting with a pulsed laser at ∼360 nm. This is a region with little splitting or shifting of the donor lines. Several spectra are shown from various locations on the confocal scans. The spectra have been offset for clarity, but have not been normalized. The colors of the spectra match the colors of the locations on the confocal scan. The "low", "med", and "high" notations on the spectra indicate the approximate amount of total counts on the confocal scan at the location that the spectra was taken.

For these scanning optical microscopy images, a focused laser spot is raster-scanned across the sample surface while PL signal is collected from each spot. Upon collecting spectral data, we see that both of these regions are promising, in that at most locations there is little observed splitting or shifting of the D^0X lines. However, even in these promising regions, some locations are more favorable than others. For example, many of the locations with high intensity on the confocal scans in Fig. 3.3, such as those corresponding to spectra 1, 2, 3, and 6, have a large surface exciton (SX). The SX interferes with our ability to identify and

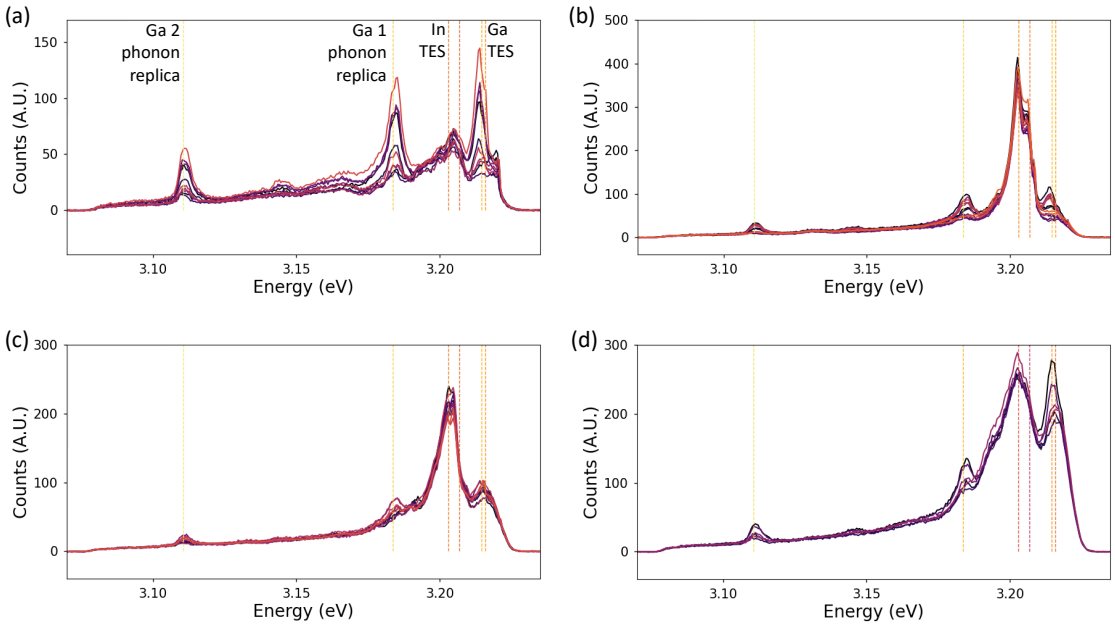

Figure 3.4: Spectra at four different locations with near-resonant excitation of the Ga D^0X line. The Ga TES, In TES, and Ga LO-phonon-replicas are marked in each plot. Each plot (a-d) refers to a different location. The spectra within each plot correspond to slightly different excitation energies. Locations with a strong response of the Ga TES and Ga LO-phonon-replicas as the excitation laser is scanned over the Ga D^0X transition are preferred.

address the D^0X lines. In choosing a location for further study, it is necessary to balance a small SX with a high D^0X intensity. Thus, locations such as the one corresponding to spectra 4 are the most favorable. It is also interesting to note that just looking at a confocal scan, where the difference in signal can be the result of changes in the intensity of the D^0X peak and/or the SX, is not enough to tell us about the quality of a location; we must use spectral data. Therefore, we use a combination of confocal and spectral measurements to look for regions (i.e. areas of confocal scans) with many favorable looking locations (i.e. specific points on a confocal scan). We then use the best regions as described in the next paragraph.

Once a region with several locations exhibiting sharp and bright D^0X lines is identified, we then choose the best locations for the measurements performed in Ch. 4. We look for locations that have a strong response in the TES and LO-phonon replica spectral region to

resonant excitation of the D^0X lines (see Sect. 2.3 and Sect. 4.2). Fig. 3.4 shows spectra of the TES/LO-phonon replica spectral region from four different locations. For these examples, the continuous-wave excitation laser has been scanned over the Ga D^0X line, though we often also considered the case of scanning over the In D^0X line. The most favorable locations have a strong response of the TES and LO-phonon replica peaks that correspond to the D^0X line we are resonantly exciting and have a low signal in other areas. For example, Fig. 3.4(a,b,d) all show reasonable enhancement of the Ga TES and Ga LO-phonon replicas as the excitaion laser is scanned; however, Fig. 3.4(a) is the most favorable, because it has the lowest background coming from the In TES lines. Fig. 3.4(c) is an example of a small response to the resonant laser and a high background, making this the least favorable location of the four shown in this figure.

We are also interested in whether the favorable-looking locations correspond to nanowires or nanowalls. We thus sought to correlate the PL measurements with SEM images. To enable us to correlate different microscopy methods, we made markers with a focused ion beam (FIB). A beam of Ga ions is used to mill into the sample, then a beam of electrons is used to image the markers and nanowires. More details on the FIB process are provided in Sect. 3.3. Fig. 3.5(a) is an SEM image where the darker squares and rectangles on the right and left edges are the markers, the brightest areas of the sample contain fallen-over nanowires, and the gray areas are undamaged regions of nanowires and nanowalls. Within the markers, the GaN substrate is exposed; occasionally, small amounts of ZnO remain within the marker region as indicated by the small bright dots in the right-edge marker. The undamaged ZnO region is similar to the zoomed-in images in Fig. 3.2, in that the small bright circles are the nanowires and all the material in between are nanowalls.

Using these markers, we are able to collect scanning optical microscopy images (confocal images) of the regions of which we have SEM images, while the sample is mounted in our cold-finger cryostat system. We begin by using the direct laser reflection as our confocal image signal. In Fig. 3.5(b), the blue overlaid image is the laser-reflection image with the intensity inverted (i.e. the areas with highest laser reflection appear dark). In the marker region, the laser is strongly reflected off of the smooth GaN substrate. This allows us to get an approximate position and magnification for the laser-reflection image with respect

to the SEM image. We fine tune the position and magnification by noting that the tops of the undamaged nanowires also appear to strongly reflect the laser. We have therefore confirmed that we are collecting confocal images in the region of interest and have the correct orientation and magnification factor between the SEM and confocal images.

Then we collect confocal images while exciting with a laser higher in energy than the D^0X transitions (3.4440 eV) at 13 K and 0 T. The laser reflection is filtered out and only PL between 3.3230-3.3773 eV (367 - 373 nm) is collected, corresponding to the donor D^0X and SX luminescence. The donor PL is quenched in a large region around the markers due to damage from the ion beams; this makes it more difficult to get the initial alignment between the SEM and confocal images. Our hypothesis was that the nanowires would wave-guide the light toward the objective; therefore, the nanowires would be the brightest features in this confocal image. However, we found that the nanowires appear dim in our D^0X-PL confocal scans (Fig. 3.5(c)). Considering the results in Fig. 3.3, we are uncertain whether the high signal seen on the nanowalls in these D^0X-PL confocal scans is the result of D^0X or SX luminescence.

Finally, as shown in Fig. 3.5(d), we excited the sample with near-donor-resonant laser light (3.36004 eV) at 13 K and 0 T. The laser reflection is filtered out and only luminescence between 3.2028-3.3230 eV (373 - 387 nm) is collected, corresponding to the TES/LO-phonon replica PL (Sect. 2.4). The bright spots are not correlated with any structures in the sample. This may be because the TES and LO-phonon replicas are only enhanced when the excitation laser is resonant with a donor D^0X transition. While spectra taken using the spectrometer appear to have D^0X lines at the same energy, there may be shifts in D^0X energies that are smaller than the resolution of our spectrometer. These shifts may be the result of differences in strain or impurity concentrations across the sample. Therefore, we are unable to correlate the TES/LO-phonon replica confocal scans to structures in the SEM images.

In conclusion, we found that there are regions in the ZnO/GaN sample that display favorable PL properties that warrant further study; these properties include sharp and bright D^0X lines and a strong response of the TES/LO-phonon replica lines to resonant excitation. However, we were unable to correlate the PL to particular structures in the sample. The

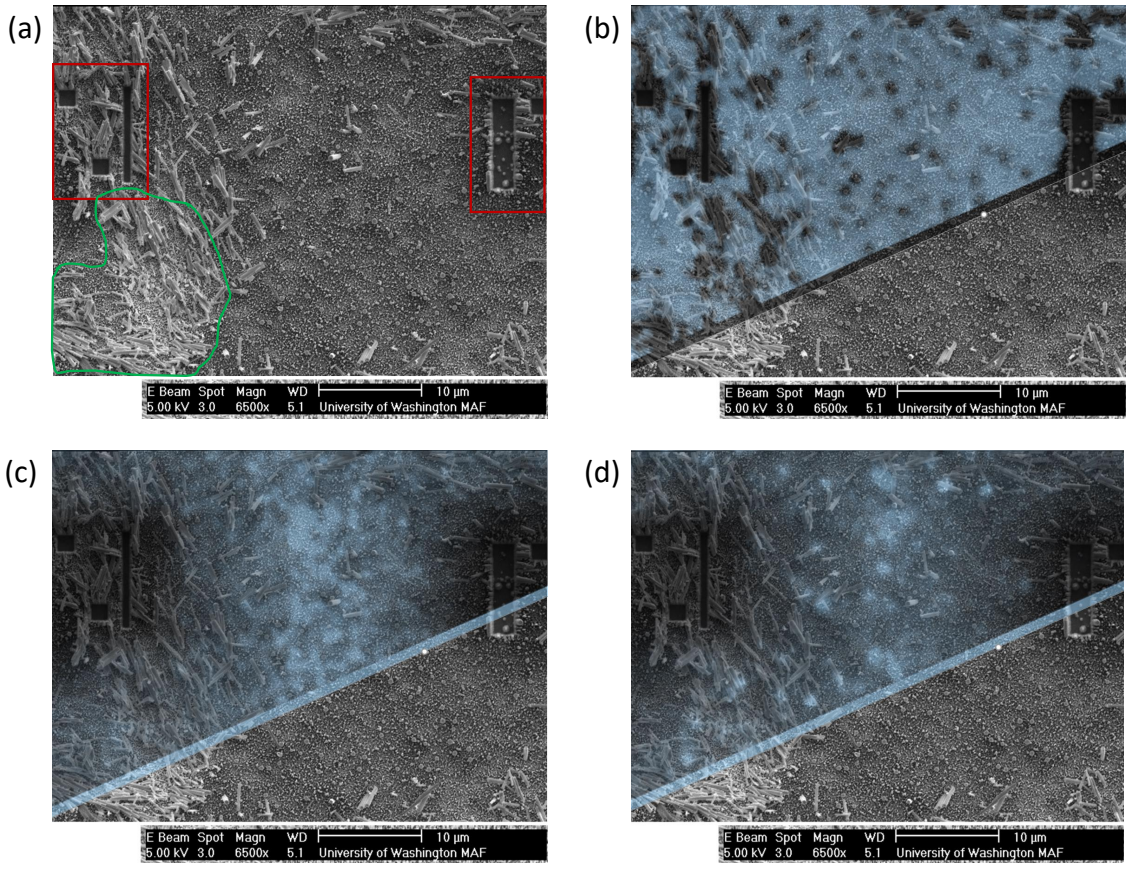

Figure 3.5: (a) SEM image of the region of interest on the ZnO nanowire on GaN sample. The squares and rectangles marked in red are markers made using the FIB. The green encircled area is a region of fallen over nanowires. (b) Gray SEM image with a blue laser-reflection confocal scan overlaid. Intensity is inverted for ease of comparison (i.e. areas with high laser reflection appear dark and vice versa). The FIB markers and the tops of the nanowires tend to reflect more laser light. There are some spots that are reflective without an obvious well-oriented nanowire. (c) Gray SEM image with a blue D^0X-PL confocal scan. Intensity is not inverted (i.e. areas with high PL emission appear bright). The nanowires tend to appear dark. This was harder to match because the whole region near the maker is dark due to PL quenching from damage by scattered ions. (d) Gray SEM image with a blue TES/LO-phonon replica region PL confocal image overlaid. Intensity is not inverted. There is not a clear correlation between bright/dark spots in the confocal image and nanowires in the SEM.

combination of the high PL variability with a lack of correlation to known nanostructures decreases the attractiveness of this route toward few and single donor isolation.

3.3 Physical Isolation via Ion Beam Milling

Physically isolating a single ZnO nanowire would allow us to minimize the amount of material within our measurement volume, while hopefully retaining the favorable optical properties measured in the nanowire ensemble samples. One of our attempts to isolate a single, vertically-oriented nanowire was to use focused ion beam (FIB) milling to mill down all of the nanowires within a region while leaving one nanowire standing in the middle. We used our standard nanowire samples grown on a sapphire substrate, because of the high uniformity in quality of these samples compared to the ZnO/GaN samples (i.e. all locations on the ZnO/Sapphire samples have sharp, bright D^0X lines). The milling settings must be carefully chosen to minimize the damage caused to the nanowire of interest by scattered ions, ZnO re-deposition, and heating. This must be balanced with the desire to completely remove the surrounding ZnO. This work was performed on the University of Washington Molecular Analysis Facility FEI XL830 dual-beam SEM-FIB.

A further complication is that to image the region we are milling, we must raster-scan high energy electrons or ions and collect the resulting signals. This process of imaging damages the sample in a way similar to milling. Sometimes the damage is visible, such as in the case of "melted" nanowires. Other times the damage isn't visible externally and is only perceived when doing photoluminescence (PL) measurements. Because of the difference in particle size and acceleration energy, imaging using an ion beam causes more damage than imaging with an electron beam. However, due to the geometry of the tool, when writing with ions, electron imaging occurs at a 52° angle (Fig. 3.6). Therefore the writing method must balance accuracy to be well centered on a nanowire with damage done to the nanowire.

We used two writing methods:

1. Donut method: This method better matches the cross-section of a nanowire (i.e. a circle); therefore, we can theoretically remove more material from around the nanowire than using a non-circular shape. Due to the limitations of our tool, this method must

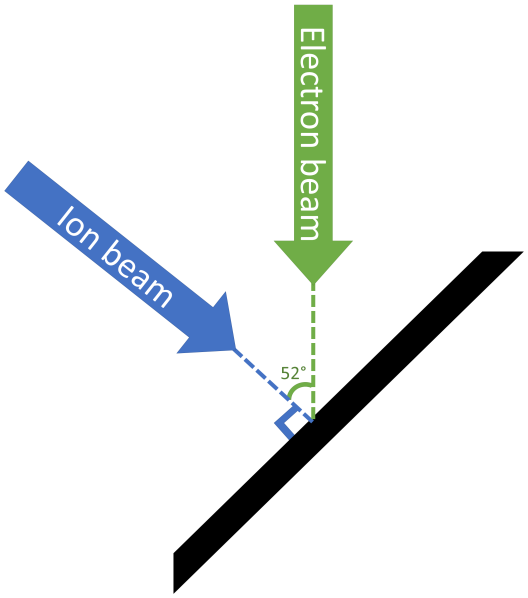

Figure 3.6: Diagram of the geometry of the FIB tool when in milling mode. The black trapezoid indicates the sample stage. When milling, the sample stage must be perpendicular to the ion beam. However, imaging is primarily done with the electron beam, which is at a 52° angle to the ion beam. Therefore, the stage must be carefully set at the eucentric height such that tilting the stage does not move the image significantly. Additionally, if imaging with the electron beam, the ion beam position relative to the image must be carefully calibrated.

be aligned using ion beam imaging; therefore, this method leads to accurately centered nanowires, but causes more damage to the nanowire of interest.

2. Square method: The shape of the milled region is not as suitable as the donut method, but the writing has more flexibility. I have developed a method that allows one to center a small square on a nanowire while only imaging it with the angled electrons. It involves several consecutive ion beam writes that help triangulate the position of the ion beam in the field of view before performing the final small square write.

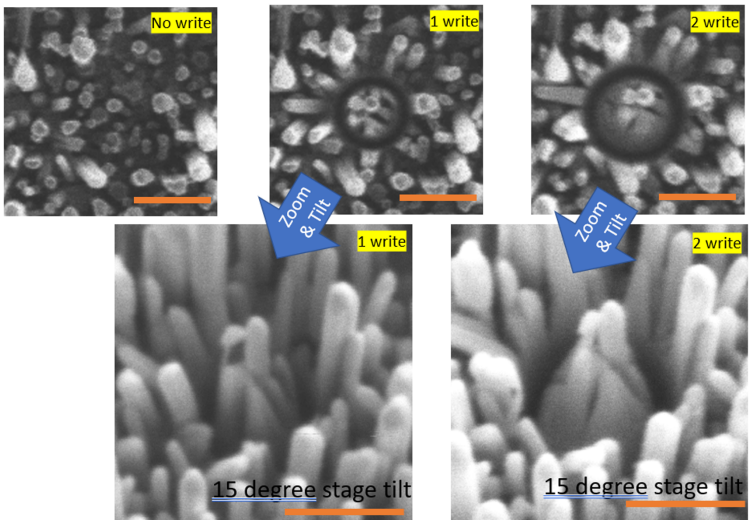

Figure 3.7: SEM images of an attempt at the donut method of nanowire isolation. The top three images are imaged with the electron beam perpendicular to the sample surface. The left-most image is of the unaltered sample. A donut pattern is milled with the stage tilted such that the ion beam is perpendicular to the sample surface. An ion current of 11 pA and an accelerating voltage of 30 kV is used. The middle image is after writing a donut pattern once. The right-most image is after writing a second, slightly-larger donut pattern. The bottom two images are taken with the stage tilted such that the electron beam is 15° from perpendicular with the sample surface.

Fig. 3.7 shows an attempt at the donut method of milling. In this attempt, we performed two consecutive writes with the second write using a slightly larger diameter donut with the goal of expanding the cleared region. However, when the sample is tilted, we see that the nanowires closest to the nanowire of interest have all fallen over onto the nanowire of interest. Additionally, we see that after the second write, the nanowire of interest has increased slightly in diameter. We attribute this to the re-deposition of ZnO from the cleared region. From this nanowire isolation attempt, we learn that if we mill too closely to the nanowire of interest, then the morphology of the nanowire will change. Changing the nanowire morphology will likely lead to strain that may affect the PL properties.

Fig. 3.8 shows attempts at the donut method of milling using donuts with different radii. For the smallest inner radius (0.25 µm), we see that, similar to above, the nanowire of interest has significantly increased in diameter. For the medium inner radius (0.6 µm),

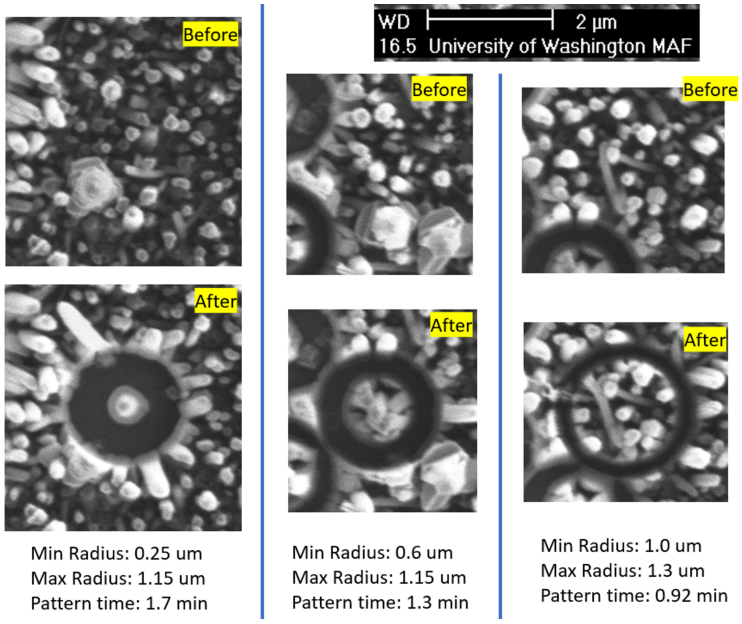

Figure 3.8: SEM images of three different attempts at the donut method of milling. An ion current of 70 pA and an accelerating voltage of 30 kV were used for the milling. Images are taken with the electron beam perpendicular to the sample surface. As indicated, the radii increase from right to left. As the radii increase, the damage to the nanowire of interest decreases, but the amount of remaining ZnO near the nanowire of interest increases.

the nanowire of interest has only increased in diameter slightly; however, there are many pieces of ZnO left around it. For the largest inner radius (1.0 µm), the nanowire of interest does not appear to have changed morphology; however, there are several full nanowires within the donut. It should be noted that the writing time changes by about a factor of two between the different writes and may affect the amount of damage. Additionally, the ion beam scatters ions into a region around the cleared region; the affected area is determined by the type of ion, the ion current, the accelerating voltage, and other factors. It is therefore possible that though there is ZnO near the nanowire of interest when using larger donut radii, the overall PL from this region may be quenched.

Fig. 3.9 shows an attempt at the square method of milling. The large rectangles are markers used to calibrate the position of the ion beam while only imaging with the electron beam. This allows for the final square outline to be milled around the nanowire of interest

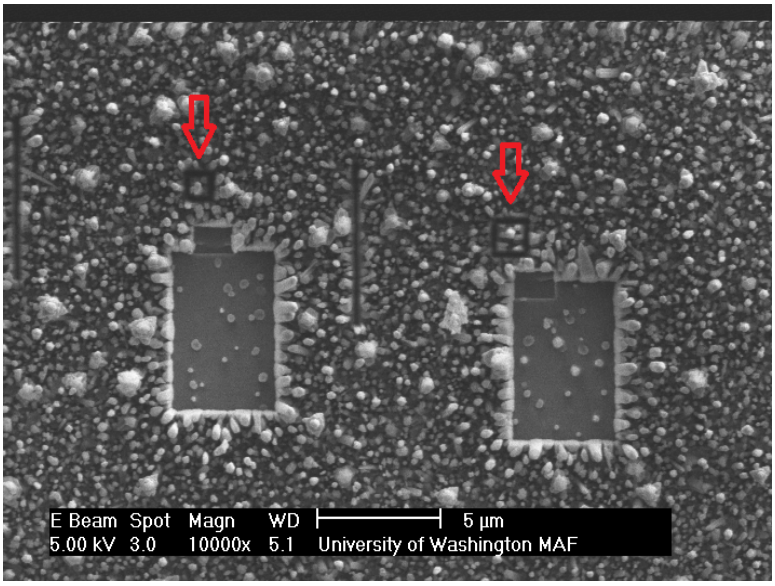

Figure 3.9: SEM image of two attempts at the square method of milling. The large rectangles are markers used to calibrate the position of the ion beam while only imaging with the electron beam. The red arrows are pointing toward the final square outlines used to isolate a single nanowire. The final mill was performed with an ion current of 70 pA and an accelerating voltage of 30 kV.

without imaging the nanowire with the ion beam. Physically, the square method of milling produces similar results to the donut method of milling.

After testing several parameters and identifying the most promising, I performed a careful final round of milling with as few images as possible. Fig. 3.10(a) shows SEM images of two of the donut patterns. We next performed low temperature scanning optical microscopy to determine how the FIB process affected the ZnO donor properties. Confocal scans show a large region of quenched PL around each the top donut (pattern #6, Fig. 3.10(b)) and the bottom donut (pattern #7, Fig. 3.10(d)). If the confocal image saturation is adjusted, a bright region becomes apparent at the center of each of the donuts (Fig. 3.10(c,e)). For pattern #7, spectra are collected starting at the center bright spot and moving radially outward (Fig. 3.10(f,g)). We assume that far from the quenched luminescence (darkest plotted spectra) the PL is unaffected by the ions. As we approach the marker, the PL intensity decreases until the bright spot. On the bright spot (yellow plotted spectra), the

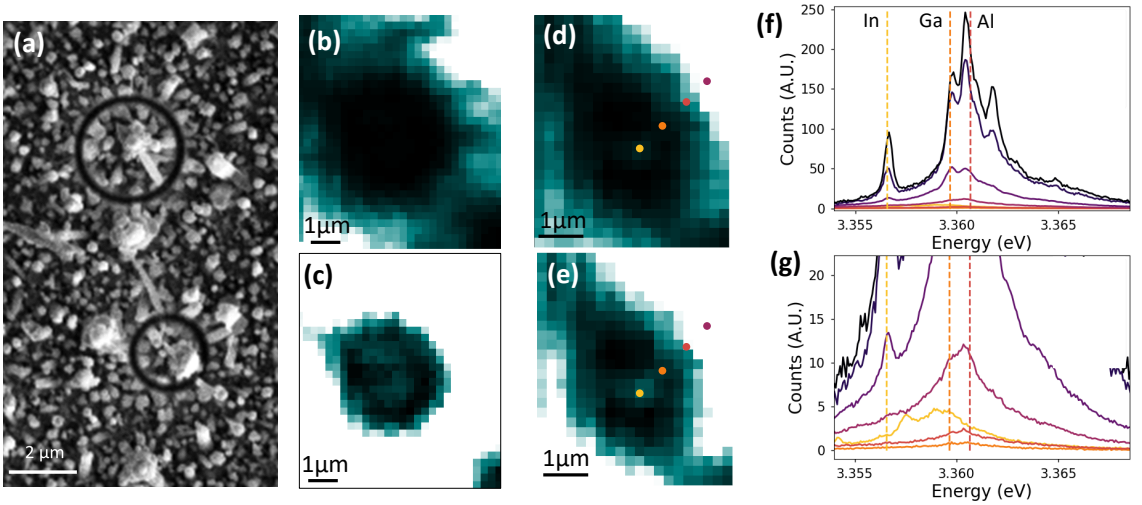

Figure 3.10: (a) SEM image of donut pattern #6 (top) and pattern #7 (bottom). Confocal images of pattern #6 (b,c) and of pattern #7 (d,e) are collected. A region of quenched luminescence is apparent in a region larger than the cleared region. (c,e) If the saturation of the image is adjusted, a small bright region can be seen inside the quenched region. (f,g) For pattern #7, spectra are collected at 10.2 K with 10 µW of pulsed laser excitation at ∼3.444 eV. Starting with the lightest color, the distance of the spectra position from the bright spot are 0.0, 0.7, 1.4, 2.1, 4.2, 5.7, and 8.5 µm. The approximate locations of the first four spectra are indicated on confocal images (d,e) with colored dots.

PL recovers slightly, but is shifted from the D^0X transition energies; either the D^0X PL shifted in energy or this is a different transition. While it is promising that we see the expected overall changes in PL intensity, the luminescence is broad and dominated by a large SX. Additionally, the D^0X transitions do not appear where expected. For these reasons as well as the suspected strain caused by the "melting" of the nanowire, this type of physical isolation was not further studied.

3.4 Physical Isolation via Exfoliation

We attempted to isolate vertically-oriented single nanowires by removing a subpopulation via exfoliation in indium metal. We begin by preparing a SiO_2 substrate with a thin layer of soft indium metal (Fig. 3.11(a)). We then take the ensemble nanowire samples grown on sapphire and gently press them into the indium metal with the nanowires facing the indium.

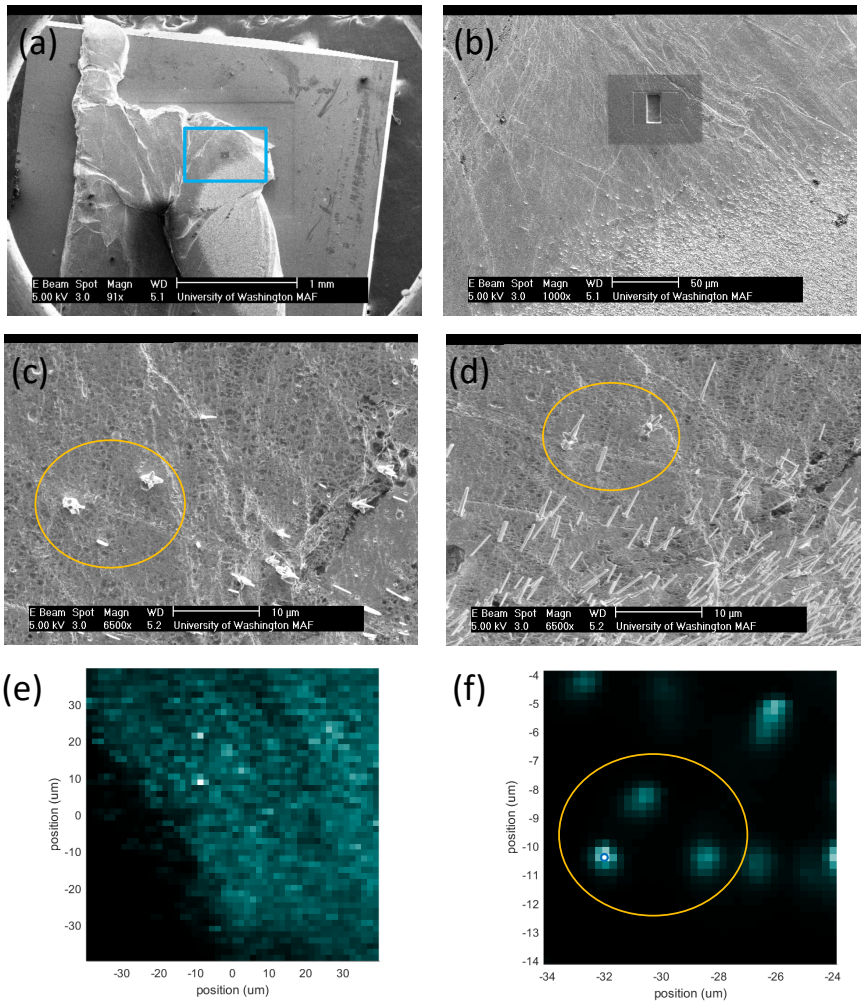

Figure 3.11: (a) SEM image of a large non-uniform piece of indium on top of a rectangular piece of SiO_2. The large feature indicated by a blue square is a marker used to locate the region of interest (b) SEM image of the region of interest. A gradient of nanowires is visible with a high density in the lower right and no nanowires in the upper left. (c) SEM image of the three nanowires of interest imaged directly from the top. The nanowires of interest are circled in yellow. (d) SEM image of the three nanowires of interest imaged with the sample stage tilted to confirm that they are nanowires (rather than nanoparticles). One of the nanowires has a simple morphology. Two of the nanowires have a flower on the top as well as a thick, non-uniform morphology. (e,f) Scanning optical image of the (e) full region of interest and (f) zoomed-in on the three nanowires of interest. The laser reflection is filtered out and only the PL is collected.

When we pull the nanowire sample out of the indium, some of the nanowires remain stuck in the indium (Fig. 3.11(b)). The natural variations in the height of the indium and the height of the nanowires leads to a gradient in the indium-bound nanowire density. We are most interested in the regions where nanowires are $> 2\,\mu m$ apart, because this allows for optical isolation. It is interesting to note that this method of isolation leads us to isolate the tallest nanowires.

After nanowires have been transferred to the indium metal, scanning electron micrographs (SEMs) are used to locate nanowires that look isolated and undamaged. From the top, vertically-oriented nanowires look like small dots; therefore, to confirm that they are not nanoparticles, the sample must be tilted (Fig. 3.11(c,d)). Once a region of interest with several nanowires has been identified, a large marker is made using focused ion beam (FIB) milling. As shown in Fig. 3.11(a,b), the marker is made several microns away to avoid damage to the nanowires of interest by scattered ions. Finally, consecutively zoomed out SEM images are taken so that the nanowires of interest can be found for optical measurements inside the cryostat.

Once individual nanowires identified via SEM have been located inside the cryostat, confocal images as shown in Fig. 3.11(e,f) are taken. The nanowires appear as point sources, because they are viewed from the top. To asses whether the exfoliation process affects the properties of the donors, spectra are taken. We find that exfoliated nanowires in dense regions retain spectra similar to those in the as-grown ensemble nanowire samples (Fig. 3.12(a)). However, the nanowires that are isolated in sparse regions have vastly varying spectral properties (Fig. 3.12(b)). These nanowires in sparse regions have D^0X lines that are shifted, broad, and split. We attribute some of these effects to strain. Additionally, the exfoliated nanowires in the sparse regions were the tallest; these taller nanowires also appear to be correlated with nanowires that have "flowers" on top or that are wider and have a strange morphology (Fig. 3.11(c,d)). As shown in Fig. 3.12(c), we also found that the low-density, exfoliated nanowires sometimes have unstable PL. The relative luminescence from different peaks changes over time and shifts. Because of these unfavorable properties seen for exfoliated nanowires, we did not study them further.

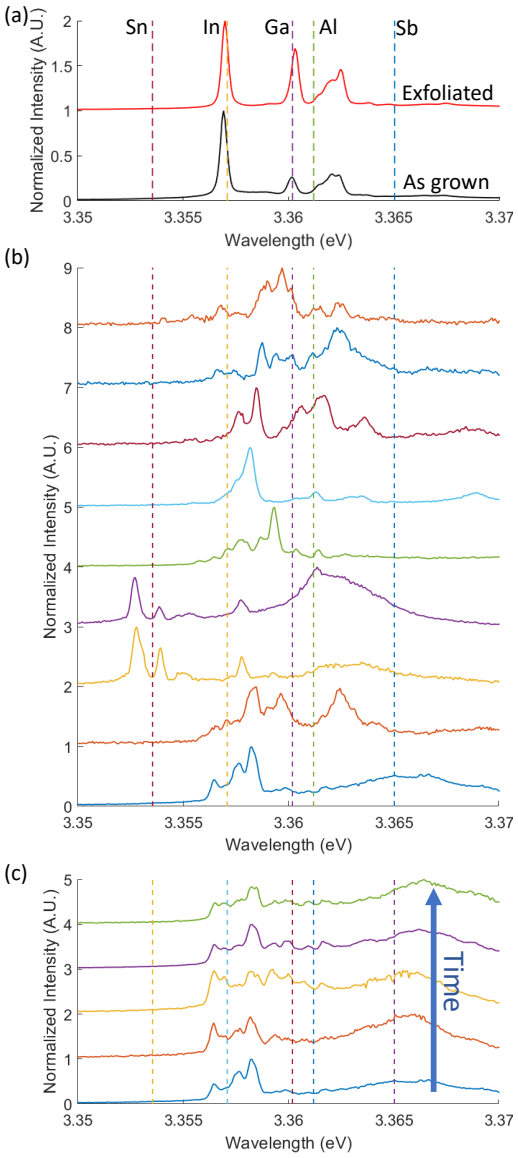

Figure 3.12: All spectra are excited with a continuous-wave laser at 3.444 eV at ∼4.2 K. (a) Spectra of the as grown nanowire sample (black) and a dense region of the exfoliated sample (red). They have very similar D^0X lines. The sample was excited with 175 µW (32 µW) for the as-grown (exfoliated) sample. (b) Spectra of several different single mechanically-isolated nanowires. All nanowires are excited with 200-500 nW. (c) Spectra from the same nanowire over 5 min. The time between measurements is not uniform. The nanowire is excited with 500 nW.

3.5 Physical Isolation via Dropcasting

Finally, we performed physical isolation of nanowires by dropcasting. In this method, the ensemble sample is sonicated in ethanol to detach the nanowires from the sapphire substrate. The nanowires are then dropcast from the solution onto a SiO_2 substrate. The dropcast nanowires are mapped and screened for favorable photoluminescence (PL) properties. Fig. 3.13 shows the results from screening several dropcast nanowires. The right column shows an optical microscope image used for initial mapping of the nanowire region. Optical microscopy is useful because it has a large field of view. Additionally, since it relies on ambient scattered light for imaging, it does not damage the samples. However, the resolution of optical microscopy is restricted by the diffraction limit of visible light and our optical microscope does not have the same precision in positioning as an SEM; this prevented us from using this method for mapping the exfoliated nanowires (Sect. 3.4) which appear as small 100 nm-sized dots when viewed from the top (as opposed to 2 µm-sized wires). The large feature in the bottom left corner of several of the images is the end of a scratch mark used for locating the region of interest. The nanowire of interest for each row is circled in yellow. The second column shows an SEM image of the nanowire of interest. The high resolution of the SEM images allow us to confirm that we are probing single nanowires and observe the differences in their morphology. The widths of the nanowires range from 160 to 360 nm. SEM images are often taken after all other measurements, because imaging with high-energy electrons may damage the nanowires. The third column shows a confocal scan with the laser reflection collected. The nanowire appears dark because it scatters light, while the substrate appears bright because the reflected laser is efficiently collected by the objective. This is a fast measurement that is useful for locating physical features when the sample is mounted inside a cryostat. The fourth column shows a confocal scan with only the D^0X PL collected. The signal at every pixel is determined by how much the laser is able to excite a particular location and how much the system is able to collect at a given location; therefore, even if the PL is waveguided to the ends of the nanowire, the middle of the nanowire will appear bright because the laser is able to excite at that location (and some of the light from the ends reaches the objective). The small circular markers in the

D^0X confocal scan indicate the location of the spectra shown in the fifth column. From the spectra, we see that the nanowires have PL of varying qualities. For the next measurements, we screen for nanowires that have a single narrow In D^0X line. Split D^0X lines are attributed to strained nanowires. Overall, we find that approximately one in five to ten nanowires has favorable PL. These promising results prompt us to continue studying this type of sample in Ch. 4.

3.6 Experimental Considerations

When choosing which isolated nanowire samples to continue studying several factors must be considered, such as photoluminescence (PL) properties, collection efficiency, and which polarizations are accessible. In the previous sections, we have seen that the dropcast nanowires have the least damage of the isolated nanowires and therefore the most favorable PL properties. However, in this section we will see that the horizontal "lying-down" geometry has a lower collection efficiency than the vertical "standing-up" geometry. Additionally, we will learn more about the differences in the accessible polarizations in each geometry.

To better understand how the orientation of the nanowire affects the collection efficiency, we must understand how light is emitted from the nanowire. To do this, we visualize the electric field strength of a dropcast nanowire using finite difference time domain (FDTD) simulation. The defect emission is modeled as three dipole sources oriented in the $\hat{x}$, $\hat{y}$, and $\hat{z}$ directions at the center of the nanowire. In the left panel of Fig. 3.14, the nanowire is simulated as lying on a substrate of 285 nm SiO_2 deposited on Si. The rectangle outlines the cross section of the nanowire (100 nm$\times$1 µm) and the horizontal lines divide materials with different indices of refraction. The simulation shows that the electric field power is guided to the ends of the nanowire and most of the energy flows into the substrate instead of the air due to the higher index of refraction. There is some asymmetry resulting from the interference of the three dipoles sources used in the simulation. We compare the lying-down nanowire to a single standing-up nanowire on a sapphire substrate in the right panel of Fig 3.14. We see that the majority of the electric field power is still guided to the ends of the standing nanowire; however, in this orientation the top end of the nanowire is far from the substrate and pointing toward the objective, allowing for a higher collection efficiency.

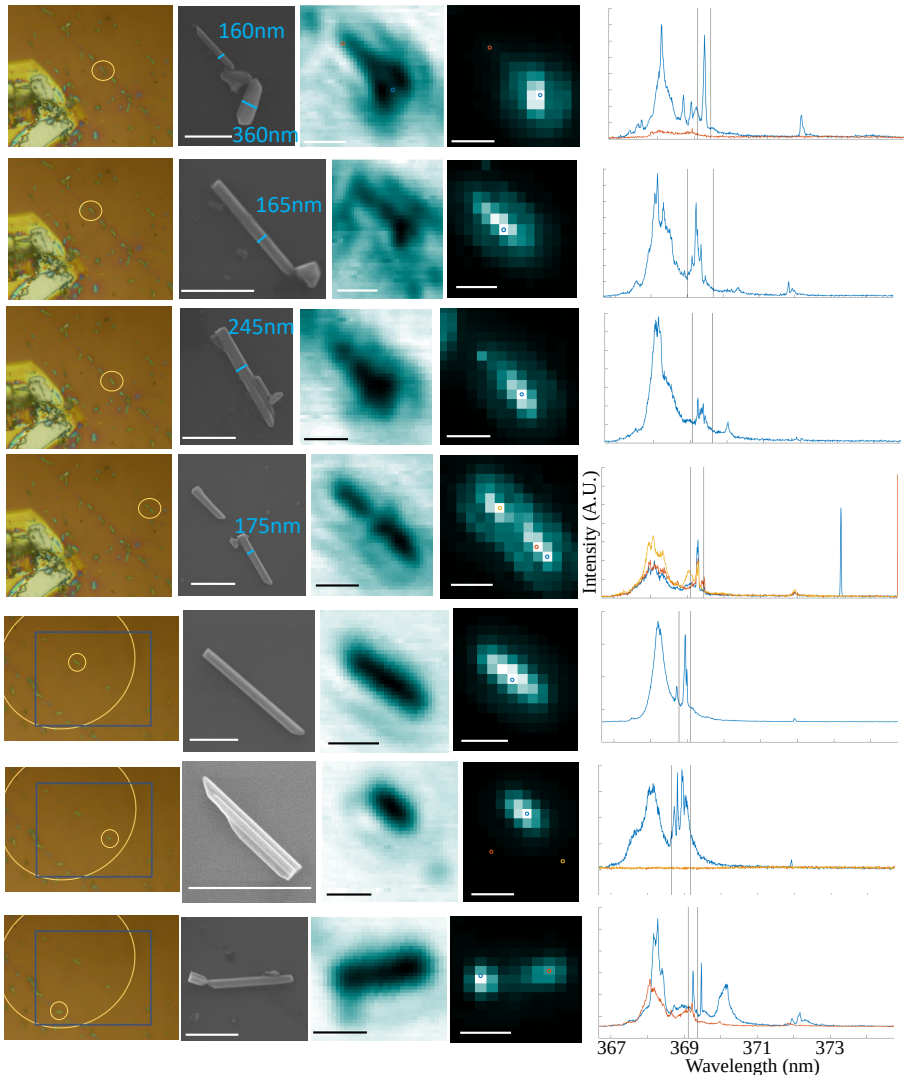

Figure 3.13: Results from the screening of several dropcast nanowires. Samples were dropcast from ensemble sample H936. Measurements are performed at 5.4 K and 0 T. Each row shows data from the same nanowire. First column: Optical microscopy image with nanowire of interest circled. Second column: SEM image of the nanowire of interest. Third column: Confocal microscopy image with the laser reflection collected. Fourth column: Confocal microscopy image with only the D^0X PL collected. Fifth column: Spectra from the location marked by a small circle in the fourth column. The black lines indicate the integration region used for the image in the fourth column. Pulsed laser excitation at 3.444 eV and 80 nW was used. All scale bars are 1 µm.

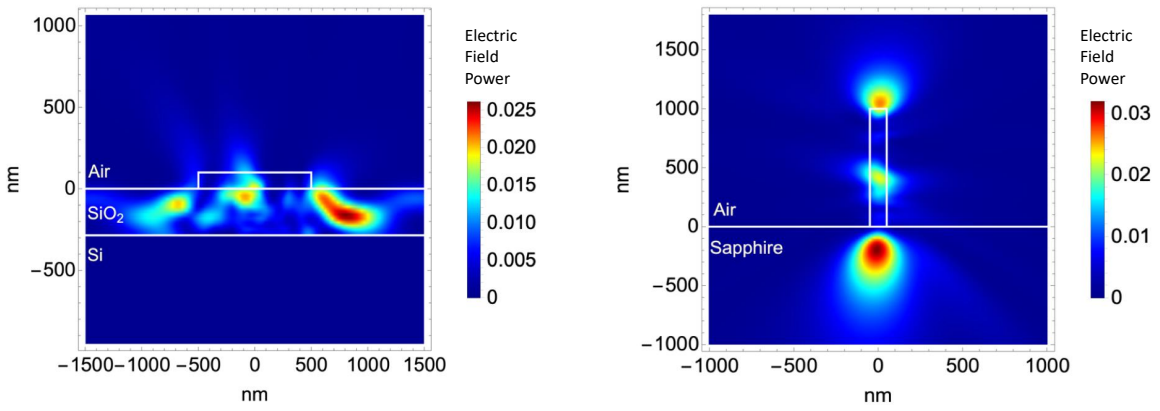

Figure 3.14: Left: Electric field strength of a ZnO nanowire lying on a Si/SiO_2 substrate (285 nm SiO_2). Right: Electric field strength of a ZnO nanowire standing on a sapphire substrate.

The orientation of the nanowire with respect to the optical axis ($\hat{k}$) determines which polarizations are accessible for excitation and collection. As described in Sect. 2.4, we define $\hat{c} \parallel \hat{z}$ and $\vec{B} \perp \hat{y}$. As shown in Fig 3.15(b,c) and derived in Appx. A, if we could collect light from all directions, we would see signatures of $\hat{x}$, $\hat{y}$, and $\hat{z}$ for each $\vec{B} \perp \hat{c}$ and $\vec{B} \parallel \hat{c}$. However, because light can only travel perpendicular to its polarization, we are only able to collect two polarizations at a time. Fig 3.15(d-h) show which D^0X transitions are accessible for each possible nanowire and magnetic field geometry.

For the experiments described in Ch. 4, we need to be able to individually address two and only two transitions; therefore, having transitions that are distinct both energetically and by polarization is ideal. Additionally, the $\hat{x}$ and $\hat{y}$ transitions are preferable to the weaker $\hat{z}$ transition. This rules out geometries such as that shown in Fig. 3.15(g) where the two transitions of the same polarization are similar in energy. The geometry shown in Fig. 3.15(e) is theoretically viable because the two accessible transitions have different polarizations; however, this geometry would be experimentally challenging because the polarization rules are relaxed when coupling into a nanowire and these transitions have similar energies. Geometries such as in Figs. 3.15(d,f) are viable because the two transitions with the same polarizations are energetically distinct. If the ability to individually address two transitions was the only consideration, the geometry in Fig. 3.15(h) would be ideal; how-

ever, we must also consider other factors, such as collection efficiency, and the lying-down nanowires have worse collection efficiency than the standing-up nanowires. While non-ideal, the measurements performed in Ch. 4 are done on the ZnO/GaN samples in the geometry shown in Fig. 3.15(e) and on the dropcast nanowire samples in the geometry shown in Fig. 3.15(f). For future measurements, we would like to move to the case where individual nanowires are standing-up on the substrate and have the magnetic field oriented perpendicular to the crystal *c*-axis (Fig. 3.15(d)).

3.7 Summary

Several methods of isolating smaller volumes of ZnO were attempted. Optical isolation of a small volume of ZnO utilizing the ZnO/GaN samples showed good photoluminescence (PL) properties in some locations that will be further studied in Ch. 4. However, this sample is not the most desirable sample, because of the non-uniformity in PL quality and the uncertainty in whether the PL measured is from nanowires or nanowalls. Physical isolation via ion beam milling led to poor PL properties due to damage from ion milling, ion and electron imaging, and strain. Samples that were physical isolated via exfoliation also displayed poor PL properties that were likely the result of selecting nanowires with non-standard morphologies, SEM imaging, and strain caused by the exfoliation process. The FIB and exfoliated types of samples were not further studied. Physical isolation via dropcasting led to samples where approximately one in five to ten nanowires have sharp, bright D^0X lines and a strong response in the TES/LO-phonon spectral region to resonant excitation. The dropcasting method isolates a smaller volume of ZnO compared to using the ZnO/GaN samples. However, the dropcast nanowires have a lower collection efficiency than methods that result in a standing-up nanowire. Nevertheless, these samples will be further studied in Ch. 4. Additionally, work is currently being done in our group in collaboration with Dirk Englund's group at MIT to push the dropcast nanowires to the edge of a substrate. This will allow for samples to be mounted such that the tips of the dropcast nanowires are pointed toward the objective.

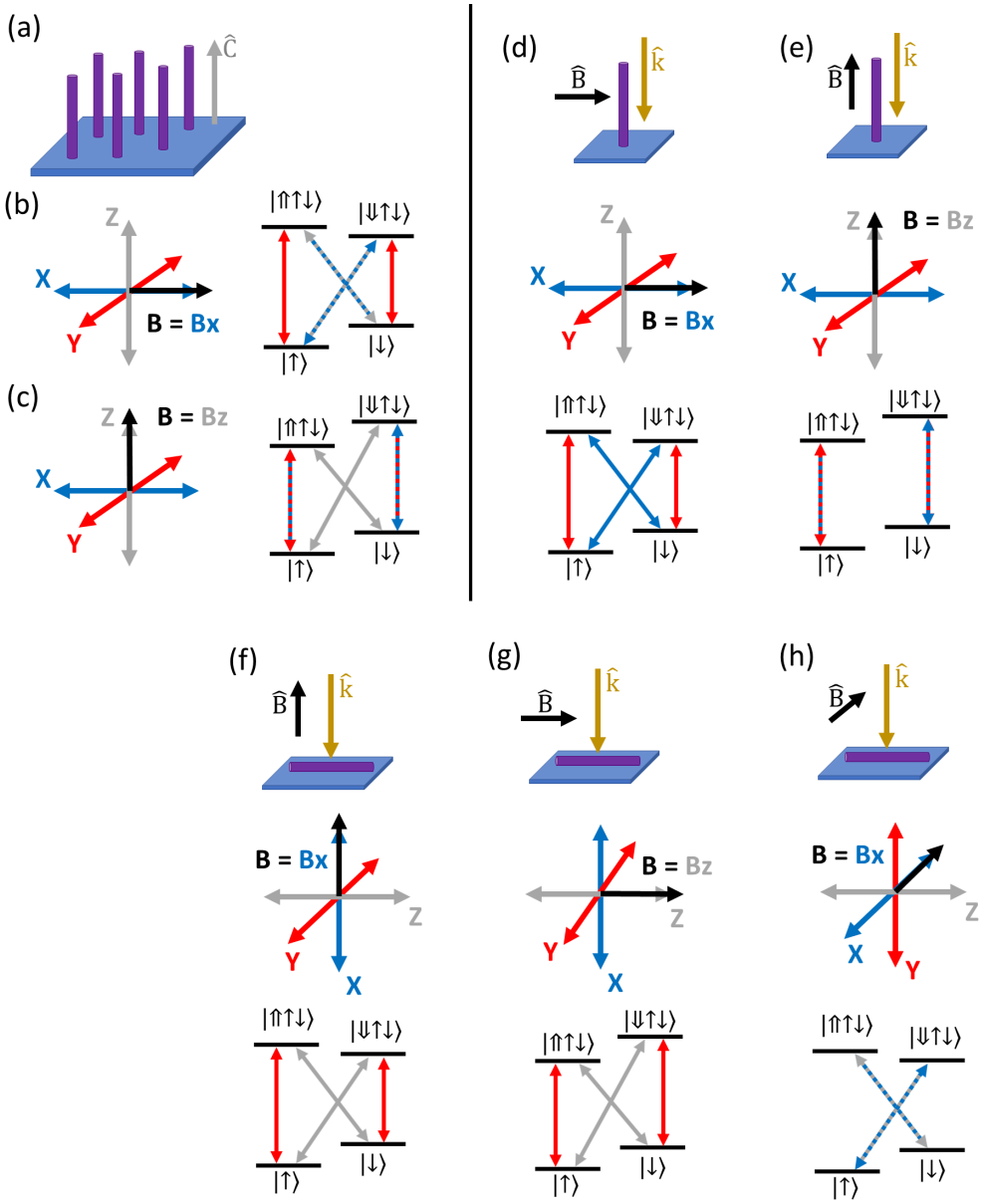

Figure 3.15: (a) Diagram defining the crystal $\hat{c}$ axis along the long axis of the nanowire. For all energy level diagrams, red, blue, and gray correspond to $\hat{y}$, $\hat{x}$, and $\hat{z}$ polarizations, respectively. Dashed lines correspond to elliptically polarized light; dashed lines with the same line colors, but different arrow colors correspond to elliptically polarized light of different handedness. (b,c) Energy level diagrams showing the transitions if we could collect light from all directions. (d-h) Top: A diagram of a nanowire and magnetic field orientation. $\hat{k}$ is the optical axis. Middle: The corresponding Cartesian coordinate system. Bottom: The corresponding energy level diagram with only the accessible transitions shown.

Chapter 4

OPTICAL AND SPIN PROPERTIES

4.1 Introduction

Most photon-based quantum information protocols utilizing donor defects will require the isolation of single donors [52, 8] and nanoscale device integration [94, 95]. However, donors are often sensitive to surface noise due to their extended effective-mass wave function and shallow donor binding energy [44, 85]. This may make obtaining good spin and optical properties for donors in nanostructures challenging. Therefore, once we have identified the most promising small-volume samples (Ch. 3), we must check that the favorable optical and spin properties seen in bulk and ensemble nanowire samples are retained. We pay particular attention to the mechanisms for linewidth broadening. These mechanisms are a good indication of the factors that may limit our ability to utilize donors in ZnO as qubits, such as our ability to individually address a given transition, whether the photons emitted are identical, and the coherence times of the system. We also consider different donors in different samples. While we choose the donor in each sample which has the brightest photoluminescence (PL), it should be noted that In donors offer some advantages over Ga and Al. In has a larger binding energy, making it more robust to temperature, and separating its D^0X line spectrally from the surface exciton and other donor lines. Additionally, In exhibits a larger hyperfine interaction with the In-9/2 spin potentially allowing for a multi-qubit register.

In Sect. 4.2, we begin by measuring the D^0X linewidth at 0 T using photoluminescence excitation spectroscopy (PLE). This resonant absorption technique allows us to achieve a higher resolution than PL measurements, because our resolution is limited by the laser linewidth (<1 MHz) rather than the diffraction spectrometer resolution. Narrow optical linewidths are important because they enable the optical probing of the spin properties of the donor ground-state and indicate high sample quality. PLE is also a measure of the

inhomogeneous linewidth, the ensemble linewidth that is a result of differences in donor environments. In Sect. 4.3, spin initialization is demonstrated using optical pumping. Spin initialization is the first step in any quantum protocol. To prove optical pumping, we observe the reverse spectral hole in a two-laser PLE experiment. The linewidth of the reverse spectral hole is typically considered a measure of homogeneous broadening, which is a broadening mechanism that affects all individual donors the same; however, we suspect that our measured spectral hole linewidth may additionally have a component from inhomogeneity in time. In Sect. 4.4, a coherent superposition spin state is prepared via coherent population trapping (CPT). CPT demonstrates our ability to prepare a qubit into a coherent quantum state, a necessary step for most quantum computation protocols. Additionally, CPT, as the basis for electromagnetically-induced transparency [34], has applications ranging from robust entanglement creation for quantum repeaters [21] to single photon-storage [62, 79] for linear optics quantum computation [48].

4.2 Photoluminescence Excitation Spectroscopy

4.2.1 ZnO Nanowires on GaN

ZnO nanowires grown on GaN substrates allow for the isolation of fewer donors than bulk samples (Sect. 3.2), while retaining the increased collection efficiency of vertically oriented nanowires (Sect. 3.6). Here, we utilize confocal microscopy to isolate $< 5 \times 10^3$ Ga donors in the ZnO/GaN samples. In photoluminescence (PL) measurements, the Ga D^0X linewidth can be spectrometer-resolution limited as shown in Fig. 4.1(a). An accurate measurement of the linewidth will allow for a better understanding of the quality of and decoherence mechanisms within our best samples. To obtain higher-resolution spectra, we perform photoluminescence excitation spectroscopy (PLE). In PLE, the Ga D^0X two-electron satellite (TES) and longitudinal optical (LO) phonon replicas are monitored while tuning the excitation laser wavelength over the Ga D^0X transitions. The TES and LO-phonon replica signal is enhanced when the excitation laser is resonant on the D^0X transition (Fig. 4.1(b)). For this sample, only the second LO phonon replica (highlighted in green) is integrated. By plotting this integrated signal as a function of excitation laser energy and fitting with a Voigt

function (Fig. 4.1(c)), we find that the full width at half the maximum signal (FWHM) at 0 T is 0.1 meV (24 GHz). This linewidth is the result of inhomogeneous and homogeneous broadening mechanisms. Inhomogeneous broadening mechanisms may include strain, varying donors concentrations, or nearby surfaces that all cause small changes in individual donor environments, as well as spectral diffusion. Homogeneous broadening mechanisms may include temperature broadening and power broadening. Typically, the inhomogeneous broadening exceeds the homogeneous broadening. The mechanisms contributing to broadening in this sample will be further studied using reverse spectral hole measurements in Sect. 4.3.

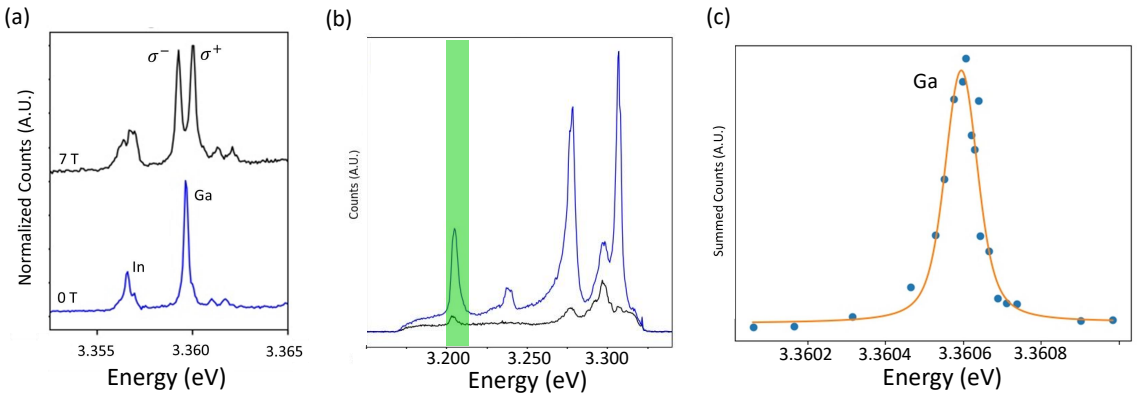

Figure 4.1: All measurements are on the ZnO/GaN sample at 5.5 K. (a) PL spectra of the Ga and In D^0X transitions. In the top spectra, a 7 T magnetic field is applied with $\vec{B} \parallel \hat{c}$. (b) Spectra of the LO-phonon replica region with resonant (blue) and off-resonant (black) excitation. The second LO phonon replica is highlighted in green. (c) PLE of the Ga D^0X transition at 0 T collecting the second LO-phonon replica luminescence. The fit FWHM is 0.1 meV (24 GHz). This figure is reproduced from [109].

4.2.2 Dropcast Nanowires

We have screened ensemble nanowire samples (Sect. 2.3) and single dropcast nanowires (Sect. 3.5) for single spectrometer-limited D^0X lines. Of those samples, we then have chosen samples that have a strong response of the TES/LO-phonon replicas to resonant excitation. In these most-promising dropcast nanowire samples, we focus on the In D^0X line rather

than the other donor lines, because of its strong signal, large binding energy, and potential for a multi-qubit register (Sect. 4.1).

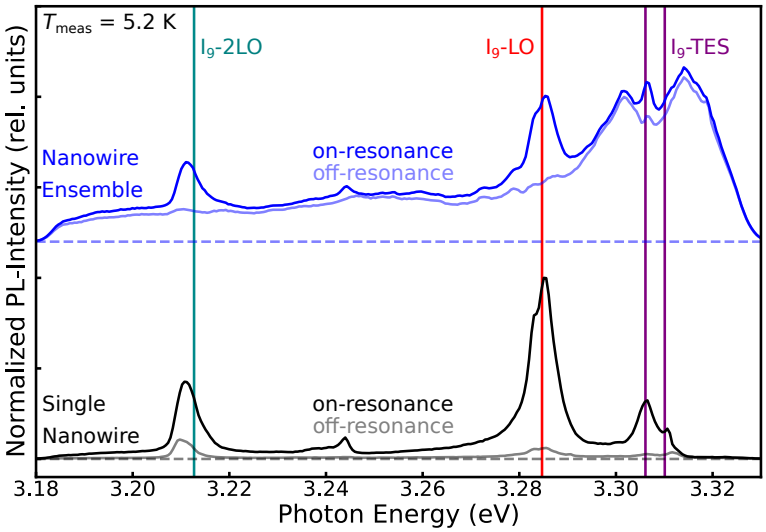

Figure 4.2: PL spectra of the TES and LO-phonon replica spectral region for a single nanowire (bottom black) and the nanowire ensemble (top blue). The ensemble data has been offset for clarity. The dashed line indicates zero intensity for the corresponding data set. All measurements are at 0 T and 5.2 K. The excitation power is 7.2 µW (200 nW) for the single nanowire (ensemble) measurements. The darker (lighter) data is with the excitation laser on-(off-)resonance with the In D^0X peak. A large non-specific background is visible for the nanowire ensemble region for both the on- and off-resonance spectra. This figure is reproduced from the supplementary information of [108].

Fig. 4.2 shows an ensemble nanowire sample (blue) and single dropcast nanowire (black) with excitation laser on- and off-resonance with the In D^0X transition. As expected, for both the nanowire ensembles and single nanowires, the TES and phonon replica are enhanced when the excitation laser is on-resonance. In the ensemble sample, however, even in the off-resonance case a large background is apparent. This background, that is uncorrelated with the In D^0X transition, may be related to the observed non-uniformity of individual nanowires or to the thin 2-dimensional layer of ZnO on the ensemble substrate (Fig. 3.2(a)). This non-specific background makes monitoring resonant excitation more challenging for nanowire ensembles. For the ensemble measurements, the background is subtracted and only the LO-phonon replicas are integrated for the PLE signal. Additionally, in some of

these PLE measurements an oscillatory background, due to wavelength-dependent optical components, has been removed. Appendix B explains this procedure. In the figure captions, we state whether this oscillation correction has been applied.

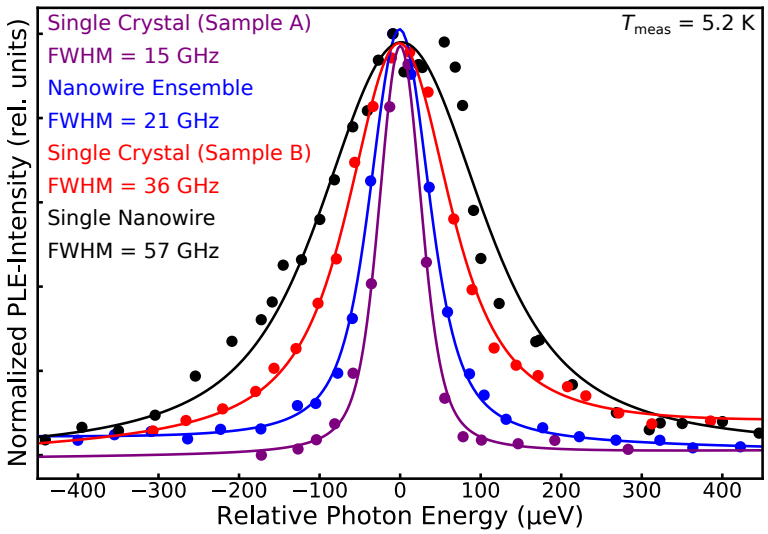

Figure 4.3: PLE spectra of bulk samples (purple and red), ensemble nanowire sample (blue), and single dropcast nanowire (black). All measurements are performed at 0 T and 5.2 K. For the bulk measurements, the excitation laser is scanned over the Ga D^0X peak with 100 nW while the TES and LO-phonon replica PL is collected. For the single dropcast nanowire measurements, the excitation laser is scanned over the In D^0X peak with 7.2 μW while the TES and LO-phonon replica PL is collected. For the nanowire ensemble measurements, the excitation laser is scanned over the In D^0X peak with 200 nW. For the nanowire ensemble measurements only, the non-specific background is subtracted and only the two-LO-phonon replica PL is collected. The solid lines are fits to the data. The FWHM for each data set is listed. This figure is reproduced from the supplementary information of [108].

To learn about the differences in linewidth broadening in different samples, we compare their 0 T PLE spectra. Fig. 4.3 displays 0 T PLE spectra for hydrothermally-grown bulk Tokyo Denpa ZnO, a single dropcast nanowire, and the unaltered nanowire ensemble sample that the dropcast sample was made from. For the bulk samples, PLE was performed on the Ga D^0X transition, whereas for the single nanowire and nanowire ensembles, the measurements were conducted on the In D^0X transition. An excitation power of 100-200 nW was used for the bulk and nanowire ensemble samples, but 7.2 μW was needed for the single

nanowire measurements. We had to use a higher excitation power for the single nanowires, because of the smaller volume of material within our measurement spot and the decreased collection efficiency (Sect. 3.6). Typically, the linewidths measured using single-laser PLE measurements at 0 T are dominated by inhomogeneous broadening. The linewidth of the nanowire ensemble (∼20 GHz) is comparable to the linewidth of different ZnO bulk crystals (15-25 GHz). This indicates that the inhomogeneous broadening observed for nanowire ensembles is comparable to that of high-quality, commercially-available, single-crystalline bulk ZnO. The single nanowires display linewidths as narrow as 57 GHz, indicating that additional broadening mechanisms are affecting single nanowires compared to nanowire ensembles. These additional mechanisms may include inhomogeneous broadening caused by the dropcasting process, such as strain or damage to the surface. The single dropcast nanowires may also have broader linewidths, because of the increased powers used for their measurements. Higher powers may result in homogeneous laser-induced temperature broadening or power broadening, as well as increased inhomogeneous broadening caused by spectral diffusion. The competition between inhomogeneous and homogeneous broadening mechanisms is further studied using reverse spectral hole measurements in Sect. 4.3.

4.3 Optical Pumping and Reverse Spectral Hole Burning

4.3.1 Introduction

Before a quantum algorithm can be executed, the qubit system must be initialized to a known spin state. For optically-active donors, this may be achieved via resonant optical pumping [60, 99]. For optical pumping, first the spin degeneracy must be lifted, such as by applying a magnetic field. Then, by applying a resonant laser to the $|\uparrow\rangle \Leftrightarrow |\Downarrow\uparrow\downarrow\rangle$ transition (Fig. 4.4(a)), any population in $|\uparrow\rangle$ is excited to the $|\Downarrow\uparrow\downarrow\rangle$ D^0X state. While D^0X states can relax into either D^0 spin state [111], any population that relaxes to $|\uparrow\rangle$ is immediately re-excited. Therefore, after several cycles, the spin is initialized to the $|\downarrow\rangle$ state. A similar procedure can be done utilizing any of the allowed optical transitions.

Fig. 4.6(a) shows photoluminescence (PL) spectra within the TES and LO-phonon replica spectral region for a single nanowire under resonant excitation of the In D^0X tran-

sition with one or two lasers. The measurements were performed at 7 T ($\hat{c} \perp \vec{B}, \hat{k}$). The inset in Fig. 4.6(a) shows on which transitions the lasers are applied. Notably, due to optical pumping, the signal under two-laser excitation is larger than the sum of the signals obtained for single-laser excitation. Under single-laser excitation, the system is spin-initialized to the ground-state level where no resonant laser is applied. Therefore, in the steady-state, only a small fraction of the system will remain in the ground-state level that the single laser is applied to, leading to a small PL signal. In an ideal system with no spin relaxation and perfect excitation selectivity, the signal will be zero. When resonant lasers are applied on two different ground state populations simultaneously, each laser will be optically pumping into a different ground state and the system will reach a dynamic equilibrium with population in both ground states. This means that system will never be fully initialized and a higher PL signal will be measured. As we will see in the next sections, this results in a recovered PLE signal called the reverse spectral hole.

4.3.2 ZnO nanowires on GaN

For the ZnO nanowires grown on GaN, measurements are performed with $\vec{B} \parallel \hat{c}$ and with the optical axis parallel to the crystal axis ($\vec{k} \parallel \hat{c}$). Fig. 4.4(b) shows two PLE spectra which confirm that optical pumping can be achieved. The excitation is power is 100 nW for all lasers. First, we perform a single-laser PLE measurement, where a continuous-wave laser is scanned over the Ga D^0X transition resonances and the second LO-phonon replica PL is collected. For these single-laser, steady-state measurements, we expect the PLE intensity to be significantly weaker at 7 T than it was at 0 T due to optical pumping. For the single-laser measurements, the σ^+ transition has a linewidth of 0.3 meV (73 GHz) (blue circles in Fig. 4.4(b)). The linewidth of this single-laser feature is theoretically a combination of the effects of optical pumping saturation and the inhomogeneous linewidth. The σ^- transition is weaker due to the lower thermal population of the $|\uparrow\rangle$ state. To confirm that the overall low signal is due to optical pumping between the two D^0 ground spin states as opposed to population leaving the system, we perform two-laser spectroscopy (green triangles in Fig. 4.4(b)). In this measurement, one laser is fixed at the σ^+ transition, while a second

laser is scanned over both transitions. Because the fixed laser continuously optically pumps population from $|\downarrow\rangle$ to $|\uparrow\rangle$, the signal is increased when the scanning laser is resonant with the $\sigma-$ transition and optically pumps population from $|\uparrow\rangle$ to $|\downarrow\rangle$. This results in a recovered $\sigma-$ peak and is called a reverse spectral hole. The reverse spectral hole should reflect the linewidth of just the subpopulation that is optically pumped by the fixed laser; thus, this linewidth is expected to reflect the linewidth of the Ga D^0X transition that is the result of homogeneous broadening mechanisms and spectral diffusion that is fast compared to our measurement time (∼20 s). We measure the linewidth of the reverse spectral hole to be ∼0.2 meV (43 GHz).

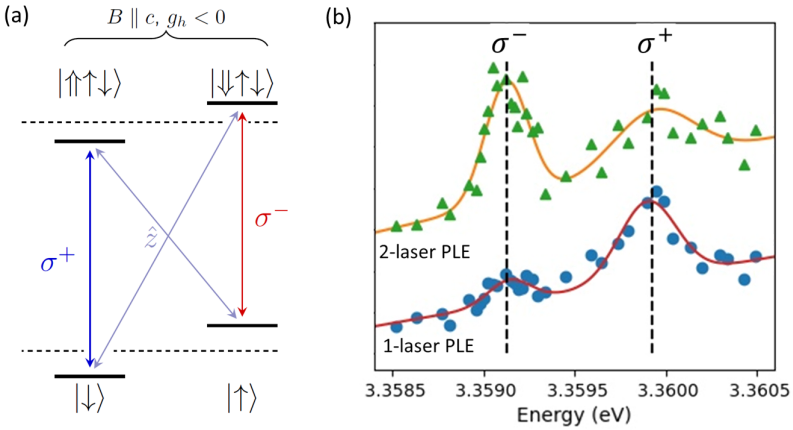

Figure 4.4: (a) Energy level diagram of the D^0 system with $\vec{k} \parallel \hat{c}$. (b) PLE of the Ga D^0X lines of the ZnO/GaN sample at 7 T collecting only the second LO phonon replica. Measurements are performed with excitation and pump laser powers of 100 nW. The blue circles are a single-laser PLE. The data in green triangles is a two-laser PLE with the pump laser resonant on the σ^+ transition. This figure is reproduced from [109].

Comparing the reverse spectral hole linewidth of 43 GHz to the 0 T, single-laser PLE linewidth of 24 GHz (Sect. 4.2), we find that the reverse spectral hole linewidth is broader. This is unusual, because the 0 T PLE linewidth is a measure of inhomogeneous and homogeneous broadening and thus should be the same width or broader than the reverse spectral hole linewidth which is considered a measure of just homogeneous broadening and fast spectral diffusion. One reason that the reverse spectral hole linewidth might be broader than the 0 T PLE linewidth is that there is increased laser-induced temperature and power

broadening in the reverse spectral hole measurements compared to the 0 T single-laser measurements; however, this is unlikely considering that the nominal difference in the total power is only a factor of two (i.e. 100 nW for each laser in the 0 T single-laser measurement and 7 T two-laser experiment). Another possible explanation is that these measurements were performed at different locations and there may be significant differences in the homogeneous broadening and fast spectral diffusion at different locations in this sample. In order to test this hypothesis, we would need to perform a careful study over many locations; however, the labor intensive nature of finding promising looking locations in this sample (Sect. 3.2) makes this path intractable. Therefore, the uncertainty in the cause of the linewidth broadening in addition to the uncertainty of which nanostructures we're probing (Sect. 3.2) leads us to focus solely on the dropcast nanowires for the remainder of this chapter.

4.3.3 Dropcast Nanowires

Optical pumping can also be seen in the standard nanowire ensemble samples (ZnO/Sapphire) and single dropcast samples. Fig. 4.6(b) displays PLE spectra for a nanowire ensemble under single- and two-laser excitation of the In D^0X transition. The application of the laser fields is shown in the inset of Fig. 4.6(b). For ensemble nanowire samples, measurements are performed with $\vec{B} \parallel \hat{c}$ and $\vec{k} \parallel \hat{c}$. The excitation power is 200 nW. Similar to the ZnO/GaN sample, first, we perform a single-laser scan over the D^0X transitions at 7 T (black data). Due to a hole splitting that is smaller than our inhomogeneous linewidth, the two transitions with the same electron spin ground-state are not resolved. For the single-laser PLE, a low signal is again observed due to optical pumping. For the pair of transitions involving the $|\uparrow\rangle$ state, the signal lies below the noise floor. For two-laser PLE, the reverse spectral hole is seen at the $|\uparrow\rangle \Leftrightarrow |\Downarrow\uparrow\downarrow\rangle$ ($|\downarrow\rangle \Leftrightarrow |\Uparrow\uparrow\downarrow\rangle$) energy when the pump laser is resonant on the $|\downarrow\rangle \Leftrightarrow |\Uparrow\uparrow\downarrow\rangle$ ($|\uparrow\rangle \Leftrightarrow |\Downarrow\uparrow\downarrow\rangle$) transition. he linewidth of the reverse spectral hole of the standard nanowire ensemble sample is ∼15 GHz. A similar phenomenon can be seen for two different single dropcast nanowires in Fig. 4.6(c,d); however, a broader linewidth of ∼ 55 GHz is measured. In single dropcast nanowires, measurements are performed on the In D^0X transition with $\vec{B} \perp \hat{c}$ and $\vec{k} \perp \hat{c}$ (inset of Fig. 4.6(c,d)). Similar to the 0 T

PLE (Sect. 4.2), we must use a higher excitation power (7.2 µW) for the single dropcast nanowires.

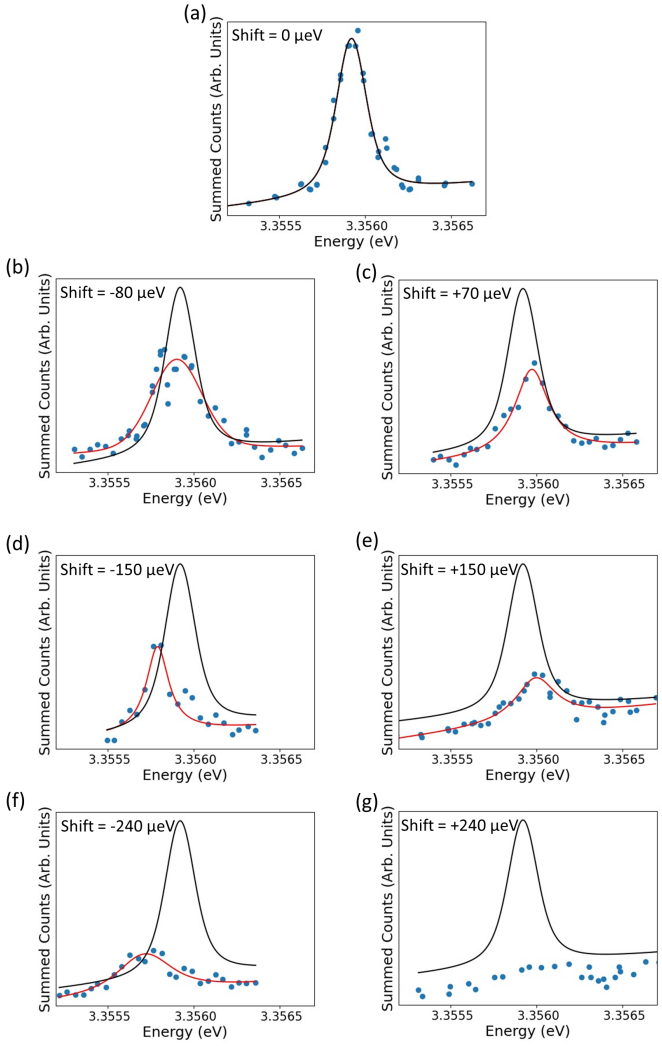

Figure 4.5: Two-laser PLE of a single dropcast nanowire. All measurements are performed at 7 T ($\hat{c} \perp \vec{B}, \hat{k}$) and 5.2 K. All laser powers are 7.2 µW. The probe laser is scanned over the In $|\uparrow\rangle \Leftrightarrow |\Downarrow\uparrow\downarrow\rangle$ transition while the TES and LO-phonon replica luminescence is measured. (a) The pump laser is on-resonance with the In $|\downarrow\rangle \Leftrightarrow |\Uparrow\uparrow\downarrow\rangle$ transition. The black line is a fit to the data. (b-g) The pump laser is shifted from the resonance by the indicated amount. The red line is a fit to the data. The black line is the fit from (a) re-plotted to aid comparison. (g) The pump laser was detuned far enough that no re-pumping was allowed; therefore, the signal was below the noise floor. This figure is reproduced from the supplementary information of [108].

To further confirm that the observed peak is related to the reverse spectral hole and not some other process in the system, we perform two-laser PLE for a single nanowire with different pump laser wavelengths near the In D^0X transition (Fig. 4.5). The measurements were performed at 7 T ($\hat{c} \perp \vec{B}, \hat{k}$). Fig. 4.5(a) is a PLE with the pump laser on-resonance with the In $|\downarrow\rangle \Leftrightarrow |\Uparrow\uparrow\downarrow\rangle$ transition. Fig. 4.5(b-g) are PLE with the pump laser shifted by the indicated energy. By comparing the off-resonance data (blue data) with the on-resonance data (black fit reproduced in each figure), we can see that the more off-resonance the excitation is, the more the signal decreases. This can be understood as being a result of the pump laser optically pumping a smaller subpopulation.

The reverse spectral holes, seen in the ensemble sample and in the single nanowire sample, show that optical pumping between the two D^0 ground states is occurring. The two-laser linewidth of 15 GHz (55 GHz) for the ensemble (single) nanowires corresponds to the spectral diffusion and homogeneously broadened linewidth of the donor subpopulation that is optically pumped. Surprisingly, these values are within the uncertainty of the 21 GHz (57 GHz) 0 T single-laser ensemble (single) nanowire PLE linewidth (Sect. 4.2) which includes static inhomogeneous broadening from the entire donor ensemble. It is unlikely that the similarity between the 0 T single-laser and the reverse spectral hole linewidths in these samples is a coincidental result caused by differences between specific locations or nanowires, because of the observed uniformity in PL measurements performed on any given ensemble sample and the similarity between the linewidths measured across both single nanowires. Therefore, the similarity between the 0 T single-laser and the reverse spectral hole linewidths suggest that the dominant broadening for both of these measurements is related to homogeneous mechanisms, such as power broadening [87] and laser-induced temperature broadening, as well as spectral diffusion that is fast compared to our measurement time (20 s) [38, 23, 63]. Thus, surprisingly, the inhomogeneous broadening expected in the 0 T single-laser measurements is similar to or smaller than these mechanisms. Furthermore, we may consequently attribute the increased linewidths measured in single nanowires compared to ensemble samples to be related to mechanisms exacerbated by higher excitation powers, such as homogeneous broadening and fast spectral diffusion, and increased sample strain/damage which may increase spectral diffusion.

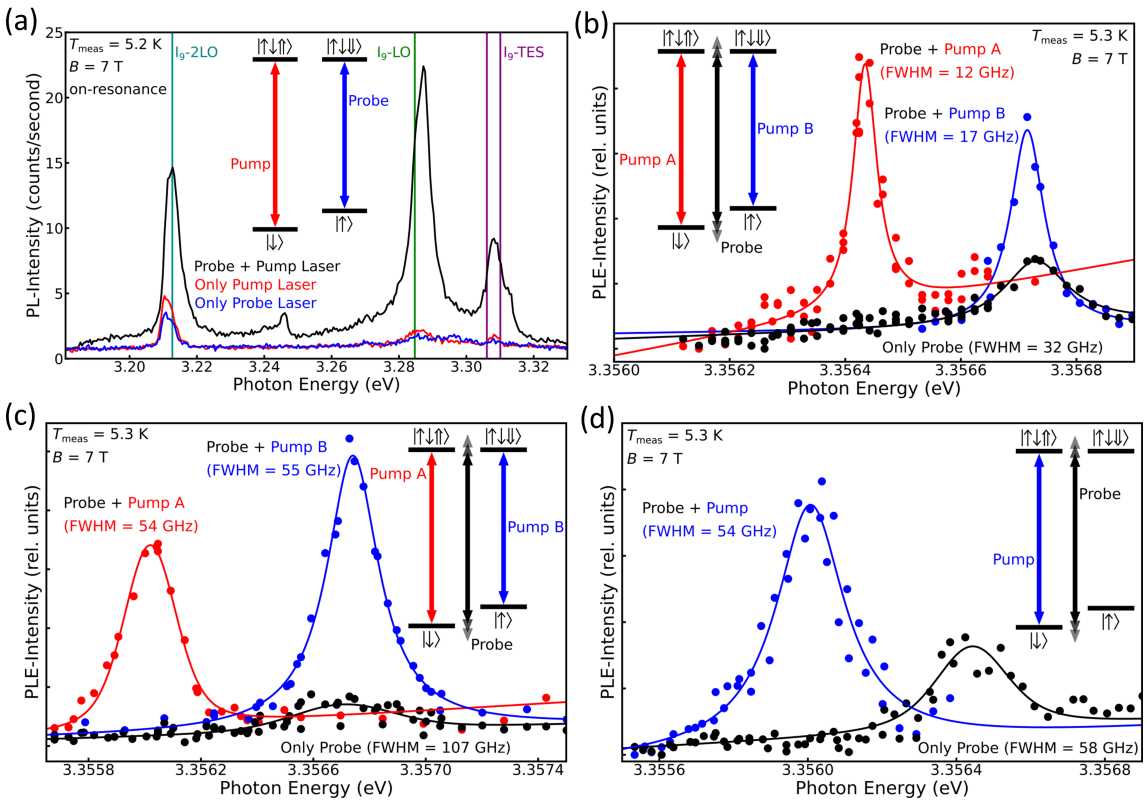

Figure 4.6: (a) PL spectra of the TES and LO-phonon replica spectral region for a single dropcast nanowire at 7 T ($\hat{c} \perp \vec{B}, \hat{k}$) and 5.2 K. Both the pump and probe lasers have an excitation power of 7.2 µW. The inset shows an energy diagram illustrating the application of the laser fields. The probe laser is on-resonance with the In $|\uparrow\rangle \Leftrightarrow |\Downarrow \uparrow\downarrow\rangle$ transition. The pump laser is on-resonance with the In $|\downarrow\rangle \Leftrightarrow |\Uparrow \uparrow\downarrow\rangle$ transition. (b-d) Single- and two-laser PLE of a (b) nanowire ensemble and (c,d) single dropcast nanowire sample. (c) and (d) are two different single nanowires. The experimental geometry is (b) $\vec{B}, \vec{k} \parallel \hat{c}$ or (c,d) $\vec{B}, \vec{k} \perp \hat{c}$. The excitation power is (b) 100 nW or (c,d) 7.2 µW. The oscillation correction was applied to (c,d) (Appendix B). This figure is reproduced from [108].

4.4 Coherent Population Trapping in Single Dropcast Nanowires

Coherent population trapping (CPT) occurs when the two transitions of a Λ system are simultaneously pumped and the system enters a dark state [27, 93, 32, 120]. For example, the Λ system can be formed between the two electron ground states and a single excited D^0X state. Mathematically, we can gain some insight into CPT by considering a simplified Hamiltonian. States $|1\rangle$ and $|2\rangle$ correspond to the ground spin states and state $|3\rangle$ is the

excited state. This Hamiltonian, in the rotating wave approximation and interaction frame, in the absence of relaxation terms, and on two-photon resonance is given by

$$H = -\hbar \begin{pmatrix} 0 & 0 & \frac{\Omega_{\text{pump}}}{2} \\ 0 & 0 & \frac{\Omega_{\text{probe}}}{2} \\ \frac{\Omega_{\text{pump}}}{2} & \frac{\Omega_{\text{probe}}}{2} & 0 \end{pmatrix} \tag{4.1}$$

where Ω_{probe} (Ω_{pump}) is the Rabi frequency of the probe (pump) fields applied to the $|2\rangle \Leftrightarrow |3\rangle$ ($|1\rangle \Leftrightarrow |3\rangle$) transition. By solving the eigensystem $H|\Psi\rangle = E|\Psi\rangle$, we find the following eigenvalues [25],

$$\lambda_{\text{dark}} = 0 \tag{4.2}$$

$$\lambda_{\text{a}} = -\sqrt{|\Omega_{\text{probe}}|^2 + |\Omega_{\text{pump}}|^2} \tag{4.3}$$

$$\lambda_{\text{b}} = \sqrt{|\Omega_{\text{probe}}|^2 + |\Omega_{\text{pump}}|^2} \tag{4.4}$$

and corresponding eigenvectors

$$|\Psi_{\text{dark}}\rangle = \frac{1}{\sqrt{|\Omega_{\text{probe}}|^2 + |\Omega_{\text{pump}}|^2}} (\Omega^*_{\text{probe}}, -\Omega_{\text{pump}^*}, 0) \tag{4.5}$$

$$|\Psi_{\text{a}}\rangle = \frac{1}{\sqrt{|\Omega_{\text{probe}}|^2 + |\Omega_{\text{pump}}|^2}} \left(\frac{\Omega_{\text{probe}}}{2}, \frac{\Omega_{\text{pump}}}{2}, -\frac{\sqrt{|\Omega_{\text{probe}}|^2 + |\Omega_{\text{pump}}|^2}}{2} \right) \tag{4.6}$$

$$|\Psi_{\text{b}}\rangle = \frac{1}{\sqrt{|\Omega_{\text{probe}}|^2 + |\Omega_{\text{pump}}|^2}} \left(\frac{\Omega_{\text{probe}}}{2}, \frac{\Omega_{\text{pump}}}{2}, \frac{\sqrt{|\Omega_{\text{probe}}|^2 + |\Omega_{\text{pump}}|^2}}{2} \right) \tag{4.7}$$

Notably, one of the eigenvectors is a superposition of only the two ground states (Eq. 4.5). Since the excited state is never populated in this case, this means that no photoluminescence (PL) can be experimentally observed. For systems where the lower state coherence times are longer than the excited state radiative lifetime, the dark state will be the steady state solution under continuous excitation.

Experimentally, CPT is realized as sharp 2 GHz wide dip on the reverse spectral hole peak. Fig. 4.7(a,b) shows a high resolution two-laser PLE scan performed at 7 T ($\hat{c} \perp \vec{B}, \hat{k}$) that reveals such a dip. In our experiments, because the Zeeman splitting between the D^0X states is small relative to the reverse spectral hole linewidth, the pump laser is able to excite both $|\downarrow\rangle \Leftrightarrow |\Uparrow\uparrow\downarrow\rangle$ and $|\downarrow\rangle \Leftrightarrow |\Downarrow\uparrow\downarrow\rangle$ simultaneously as depicted in the insets of

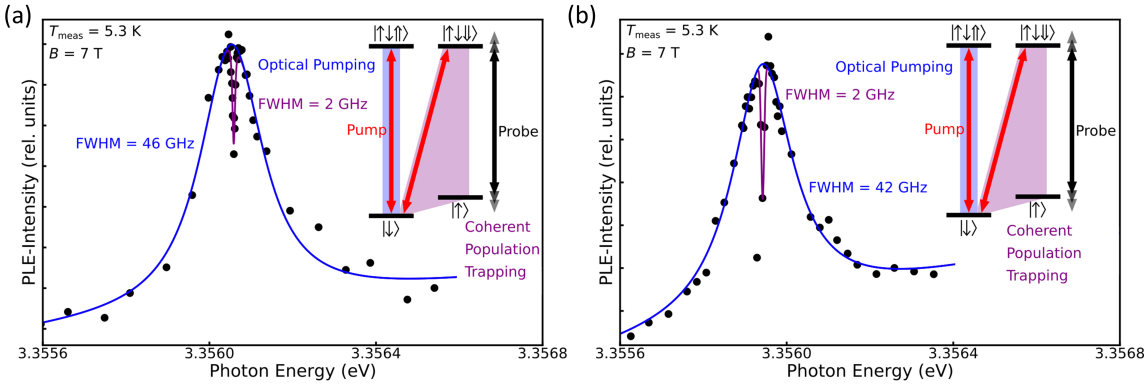

Figure 4.7: High resolution, two-laser In D^0X PLE spectrum. (a) and (b) are similar data for two different single dropcast nanowires. The insets show energy diagrams illustrating the application of the laser fields. Measurements are performed at 5.3 K and 7 T ($\hat{c} \perp \vec{B}, \hat{k}$). The excitation power is 7.2 µW for both pump and probe lasers. The solid lines are empirical fits to the reverse spectral hole peak and the CPT dip. The oscillation correction has been applied (Appendix B). These figures are reproduced from [108].

Fig. 4.7(a,b). A Λ system is formed by the pump laser driving $|\downarrow\rangle \Leftrightarrow |\Downarrow\uparrow\downarrow\rangle$ and the probe laser on $|\uparrow\rangle \Leftrightarrow |\Downarrow\uparrow\downarrow\rangle$.

To confirm that the dip is related to CPT, we detune the pump laser energy by Δ from $|\downarrow\rangle \Leftrightarrow |\Downarrow\uparrow\downarrow\rangle$ and measure the shift of the dip. From the left panel of Fig. 4.8, it can be seen that both the CPT dip and the reverse spectral hole peak shift when the spectral position of the pump laser is shifted. The right panel of Fig. 4.8 compares the shift of the CPT dip and the peak of the reverse spectral hole. As expected from CPT, the dip shift is one-to-one with the pump laser shift. Additionally, the difference between the spectral position of the dip and the spectral position of the pump laser is 0.76-0.77 eV. This is consistent with the expected ground-state splitting of 0.77 eV at 7 T assuming an electron g-factor of 1.90 (Sect. 2.5). The shift of the peak of the reverse spectral hole does not occur one-to-one with the shift of the pump laser's spectral position; therefore, the reverse spectral hole's lineshape is not solely determined by the position of the pump laser. This may be an indication of spectral diffusion.

Fig. 4.9 shows that reducing the pump laser power reduces the dip linewidth and con-

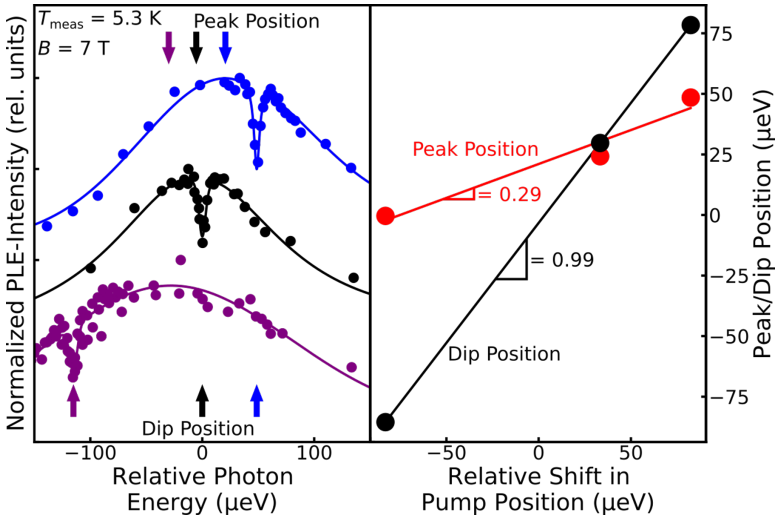

Figure 4.8: High resolution, two-laser In D^0X PLE spectra of a single drop-cast nanowire. All measurements are performed at 7 T ($\hat{c} \perp \vec{B}, \hat{k}$) and 5.3 K. All laser powers are 7.2 μW. The pump laser wavelength is shifted near the In $|\downarrow\rangle \Leftrightarrow |\Uparrow\uparrow\downarrow\rangle$ resonance. The left panel shows the PLE data with arrows indicating the fit peak and dip positions. The right panel shows the peak (red) and dip (black) positions as a function of the pump laser shift. The error in the energetic position is less than 1 μeV for the dip and 8-15 μeV for the peak. This figure is reproduced from the supplementary information for [108].

trast as expected in CPT [27, 61]. The smallest linewidth (1 GHz) approaches the linewidth expected due to the spin-9/2 In nuclear-electron hyperfine interaction, where the In line splits into 10 hyperfine lines separated by 100 MHz each [29, 11]. The CPT dip is a measure of the ground-state dephasing. Thus, considering spectral diffusion as a broadening mechanism for the reverse spectral hole peak, the narrowness of the CPT dip (1 GHz) compared to the reverse spectral hole peak (55 GHz) rules out ground-state spectral diffusion; therefore, excited-state spectral diffusion is the dominant spectral diffusion mechanism in this system.

4.5 Summary

The optical and spin properties are explored for several low-volume nanowire samples. For the ZnO/GaN nanowire sample and the single dropcast nanowire sample, photoluminescence excitation spectroscopy is performed at 0 T showing that narrow donor D^0X linewidths are retained in the nano-environments. Spin initialization via optical pumping is

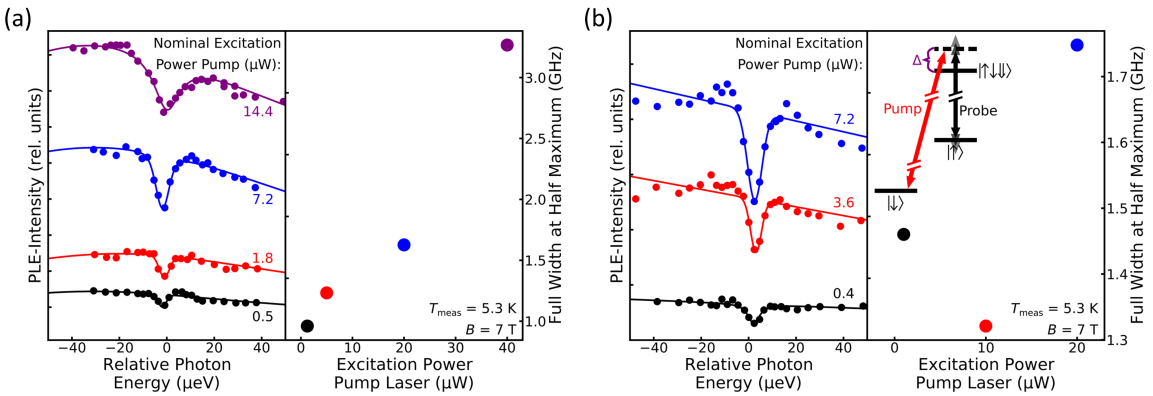

Figure 4.9: (a) and (b) are similar data for two different nanowires. Left panels: High resolution, two-laser In D^0X PLE spectra of a single dropcast nanowire zoomed in on the CPT dip. Measurements are performed at 5.3 K and 7 T ($\hat{c} \perp \vec{B}, \hat{k}$). The excitation power is 7.2 μW for the probe laser. The pump laser power is listed. The solid lines are empirical Voigt fits. Right panels: The fit FWHM as a function of pump power. The inset shows an energy diagram illustrating the application of the laser fields. This figure is reproduced from [108].

also demonstrated for both of these samples. In the single dropcast nanowire samples, the similarity between the 0 T single-laser and reverse spectral hole linewidths indicates that inhomogeneous broadening is less important than homogeneous broadening and spectral diffusion mechanisms. Finally, the preparation of a coherent superposition of the ground states is demonstrated via coherent population trapping in the single dropcast nanowires. These measurements together demonstrate the promise of donors in ZnO nanostructures for photon-based quantum applications; however, there are more challenges which need to be addressed. For example, to further improve our coherent control of the spin state, we are working toward the direct microwave control of the electron spin, rather than the optical control that we currently use. Microwave control may reduce the effects of laser-induced dephasing allowing us to achieve narrower linewidths in single nanowires and full access of the Bloch sphere. Additionally, as we will discuss further in the next section, utilizing non-standard ZnO nanowire growths may allow us to address challenges in the scalability of future nanowire-based devices and in the ability to address single defects.

Chapter 5

NON-STANDARD NANOWIRE GROWTHS

5.1 Introduction

The ZnO nanowires described in previous chapters are a great starting point for learning about the quantum properties of ZnO nanostructures; however, there are still many challenges to overcome before they can be used in scalable quantum technologies. In this chapter, we attempt to tackle two of those challenges by utilizing growth processes with novel substrates and additional steps. In Sect. 5.2, we begin by taking a closer look at metal organic chemical vapor deposition (MOCVD) and our standard ZnO nanowire recipe. Sect. 5.3 describes our attempts at selective area growth using a masked and patterned sapphire substrate. While Ch. 3 describes several methods of post-growth nanowire isolation, these methods often lead to additional strain in the nanowires and are labor-intensive. Selective area growth of nanowires would allow ZnO nanowires to be utilized in low-strain, scalable devices. In Sect. 5.4, we attempt to tackle the presence of a large surface exciton (Sect. 2.3) in our standard ZnO nanowire samples. The surface exciton energy overlaps with the D^0X transitions, making identification and resonant excitation of the D^0X states less efficient. If we can grow a shell of higher band-gap material around the nanowire, we hypothesize that the surface exciton can be shifted to higher energies away from the D^0X transitions.

5.2 Metal Organic Chemical Vapor Deposition

Metal organic chemical vapor deposition (MOCVD) is an epitaxial technique, meaning that gaseous precursors are deposited to form a thin crystalline material that follows the crystalline template of the substrate. The precursors in MOCVD are organometallic compounds. Compared to other epitaxial techniques, MOCVD has a large degree of flexibility and can grow crystals of high purity; however, MOCVD requires the use of expensive reactants and has the largest parameter space to explore [100]. While great advances have been made in

understanding the mechanisms for the growth of semiconductors using MOCVD, there are still some aspects where our understanding remains incomplete [104].

Our MOCVD reactor utilizes a relatively inert carrier gas (N_2) to transport organometallic compounds to the sample chamber. The carrier gas passes through a bubbler (Fig. 5.1(a)). In the bubbler, the carrier gas is injected into a liquid organometallic compound, such as dimethylzinc (DMZn), diethylzinc (DEZn), or bis(cyclopentadienyl)magnesium (Cp2Mg) and picks up some of the compound in a gaseous phase. The amount of organometallic compound picked up depends on the partial pressure inside the bubbler. The carrier gas and gaseous organometallic compound then travel to the sample chamber.

At the sample chamber, the organometallic compounds are brought together along with any gas phase reactants (N_2O or O_2) near the sample substrate. The substrate may be heated during the growth process, as well as annealed before or after nanowire growth. Annealing before the growth under N_2 and O_2 or under N_2O gas at 950°C removes any impurities from the substrate and saturates the sample surface with the O precursor (N_2O or O_2). Post-reaction annealing may be used to remove some structural impurities.

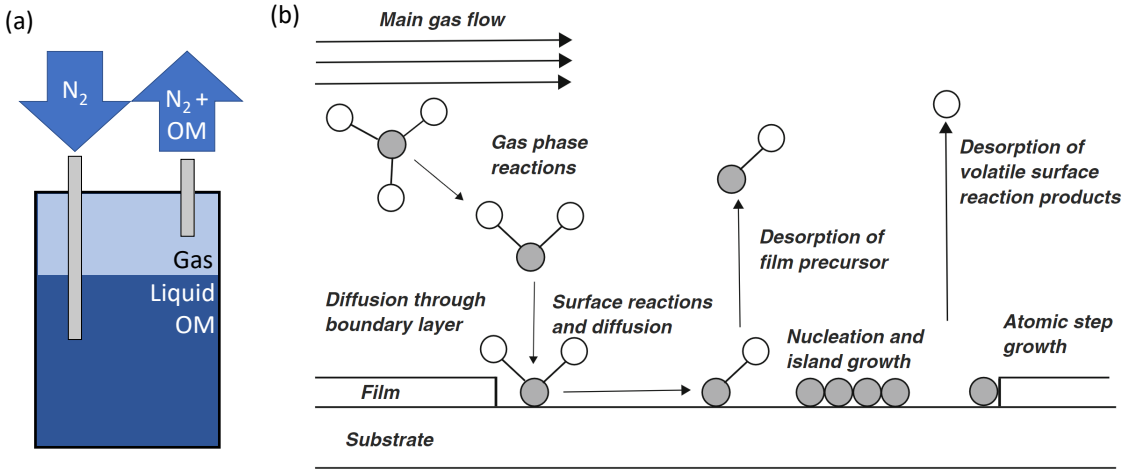

Figure 5.1: (a) A diagram of a bubbler. (b) A diagram depicting the types of processes possible inside the sample chamber. The exact processes that occur will vary depending the reactants, temperature, and other factors. (b) is reproduced from [78].

The processes that take place at the substrate surface are depicted in Fig. 5.1(b). These

processes may include [104]:

- diffusion of reactants through the boundary layer
- homogeneous reactions, where one or more of the precursors decomposes in the gas phase
- adsorption of reactants onto the substrate
- diffusion of reactants on the substrate surface
- heterogeneous reactions, where precursors decompose independently at the surface
- desorption or incorporation of adatoms at crystal step edges

Which of these processes dominates depends on the thermodynamics (i.e. whether the crystalline solid phase or gaseous phase has the lower energy) and the kinetics (i.e. the rate at which different processes, such as diffusion and chemical reactions, occur) of the system. Changing the growth parameters affects the competition between these different processes and leads to the growth of different sample morphologies; however, it is challenging to definitively say which processes are the most important for any given growth. For example, there are several different explanations for the formation of ZnO nanowires that range from arguments that substrate polarity is the most important determining factor [104] to explanations about differences in surface energy and diffusion length [77]. can still be used to change the exact morphology the nanowires [104].

In the subsequent sections, we shall explore the parameter space of several different growth conditions in the hopes of controlling various nanowire properties of interest. The parameters that we change include: the type of Zn precursor (DMZn, DEZn), the type of O precursor (O_2, N_2O), the molar flow rate of each of the precursors, the temperature during growth, and the length of each growth. Additionally, the pre- and post-annealing parameters include temperature, length of time, and flowing gas (N_2, O_2, or N_2O). The parameters used in the growth of our standard ZnO-nanowire samples was determined by the group of Simon Watkins at Simon Fraser University.

Our standard growth includes:

- Pre-anneal of the sapphire substrate at 950°C under O_2 and N_2 for 20 min
- Grow at 605°C for 60 min with 2.2×10^{-5} mol/min of DMZn and 1.3×10^{-1} mol/min of N_2O

- Post-anneal at 605°C for 2 min under N_2O

5.3 Selective Area Growth

5.3.1 Introduction

Our standard ZnO nanowire samples grow with a high density of nanowires, ~5 nanowires within a 1 µm-diameter laser spot. However, for photon-based quantum applications, nanowires should be deterministically grown with a >2 µm spacing. This would allow for optical isolation and easy incorporation into devices. One method to achieve this is with selective area growth using a masked and patterned substrate, where nanowires preferentially grow at locations where the substrate is exposed and do not grow on the mask.

Selective area growth has been shown using GaAs microstructures grown by MOCVD. Selectivity was achieved using a GaAs substrate masked with SiO_2. Small holes in the SiO_2 that expose the GaAs substrate preferentially nucleate the GaAs microstructures. Both desorption of adatoms, controlled by temperature [36], as well as diffusion of adatoms, controlled by hole size [41], are important for growth selectivity. Furthermore, ZnO nanostructures have been selectively grown by MOCVD using a SiN_x mask on a ZnO/Sapphire substrate [104] or at the tips of GaN micropyramids [39]. These methods are not ideal for our goals as using a ZnO/sapphire substrate would increase the amount of ZnO within our measurement volume and the GaN micropyramids are labor-intensive.

We present results on the selective area growth of our ZnO nanowires utilizing a sapphire substrate masked with SiO_2 or SiN_x. We will first create novel substrates by masking our standard sapphire substrate with SiO_2 or SiN_x and exposing the sapphire by etching holes of varying sizes. The morphology and nucleation rate of ZnO have been shown to vary greatly based on the substrate material [70, 115]; hence, we will then attempt to find a set of parameters that allow for the ZnO nanowires to nucleate faster on sapphire than on the mask materials (SiO_2 or SiN_x).

5.3.2 Substrate Preparation

To create the masked and patterned substrates, we first grow the mask material onto the sapphire and then use electron beam lithography and wet chemical etching to create small patterns in the mask.

The process is (Fig. 5.2 (a) and Appx. C):

- Cleave the sapphire into ∼1 cm^2 pieces. Smaller pieces make uniform coating with PMMA challenging.
- Deposit ∼30-100 nm of SiO_2 or SiN_x onto the sapphire piece using plasma-enhanced chemical vapor deposition.
- Prepare the samples for electron beam lithography by spin coating with PMMA and sputtering gold on top. PMMA is a positive resist. Gold in necessary to prevent charging during the electron beam writing process.
- Expose areas of the PMMA that will be removed (i.e. holes and markers) with an electron beam.
- Develop the PMMA in a cold IPA/water mixture. Most of the gold will also come off.
- Etch in buffered hydrofluoric acid (BHF) to remove the SiO_2 or SiN_x from the exposed regions. Nominally, BHF will etch SiO_2 (SiN_x) at a rate of 490 nm/min (60 nm/min) and not etch sapphire [116]. I measured an etch rate around 40-150 nm/min (20 nm/min) for SiO_2 (SiN_x).
- Remove the residual PMMA by sonication in acetone.

Since we do not know what size hole will work the best for the nucleation of a single nanowire, we make a variety of different hole sizes as shown in Fig. 5.3(a). The holes are 3 µm apart with diameters ranging from 100 nm to 300 nm in 50 nm increments. We arrange the holes in a 10x10 pattern (Fig. 5.3(b)). The whole square pattern is 30 µm x 30 µm. These 10x10 square patterns are arranged into groups of 3 or 4. Fig. 5.3(c) shows a group of 3. These groups include larger markers (10 µm x 20 µm) that are visible in an optical microscope at 5x magnification. The groups of 3 include number or letter labels in the bottom left quadrant for ease of identification. Fig. 5.3(d) shows an optical image of a group of 3 patterned in SiO_2.

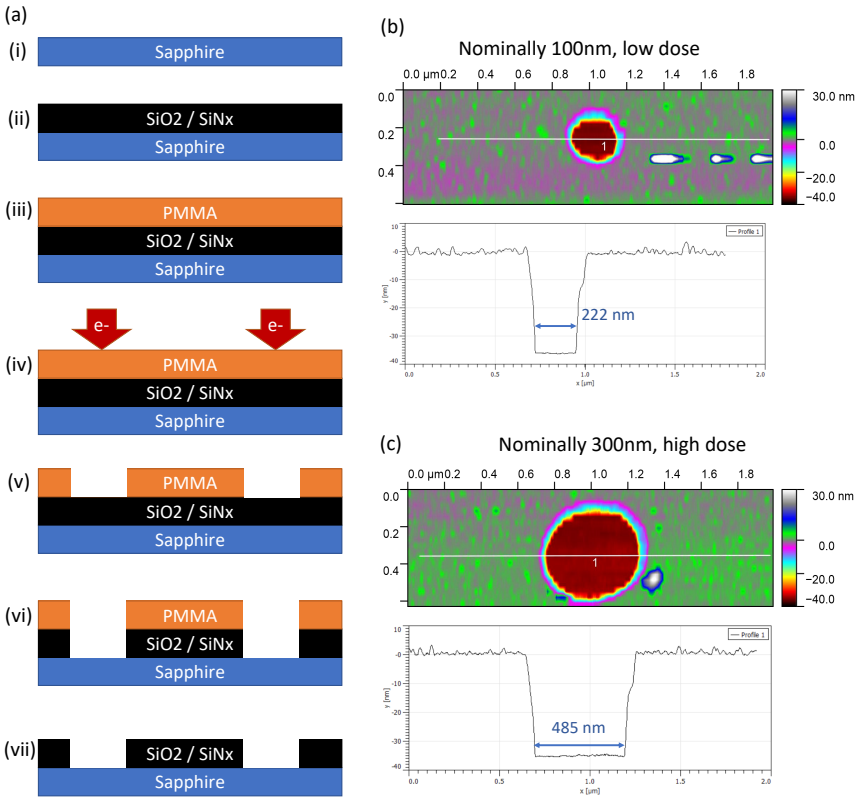

Figure 5.2: (a) A diagram depicting the substrate masking and patterning process. (b,c) AFM images showing holes that were nominally written to have diameters of (b) 100 nm or (c) 300 nm. The color indicated the measured depth. The 2-dimensional plot is a line cut along the white indicated line. The measured hole widths are approximately 100-200 nm wider than their nominal diameters.

Once the holes have been etched, we check their width using atomic force microscopy (AFM). As shown in Fig. 5.2(b,c), the holes are often 100-200 nm wider in diameter than our electron beam lithography pattern. We believe that the holes have reached the sapphire, because their edges are sharp and bottoms are flat.

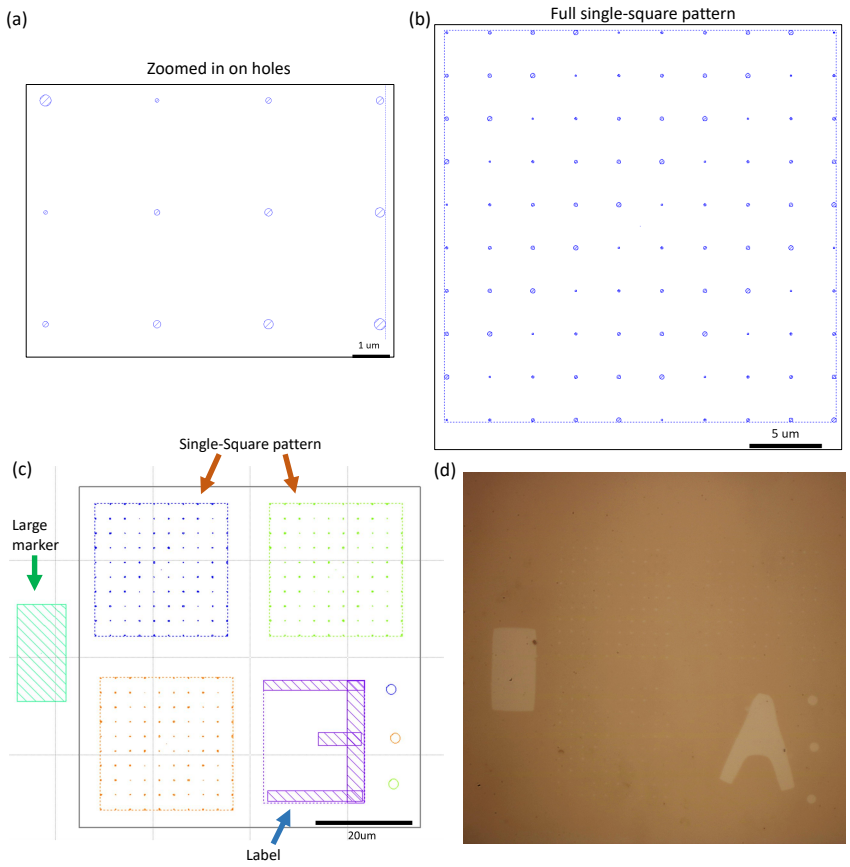

Figure 5.3: (a,b,c) Diagrams showing the nominal patterns of holes and markers at varying magnifications. (d) An optical image of a pattern in SiO_2.

5.3.3 Growth Process

Initial Growths

In Fig. 5.4(a), we begin by attempting our standard nanowire-growth recipe utilizing a substrate with an SiO_2 mask and patterned as described in Sect. 5.3.2. Growths are labelled with an H followed by a number that increases with each growth in the reactor. Fig. 5.4(a.i, a.ii) show a full pattern with corners of the large marker and "C" label indicated by red arrows. The nanowires on the exposed-sapphire markers and holes are taller and better aligned than the nanowires on the SiO_2. Fig. 5.4(a.iii) shows nanowires with a large flower shape that have formed in the exposed-sapphire holes. This growth does not

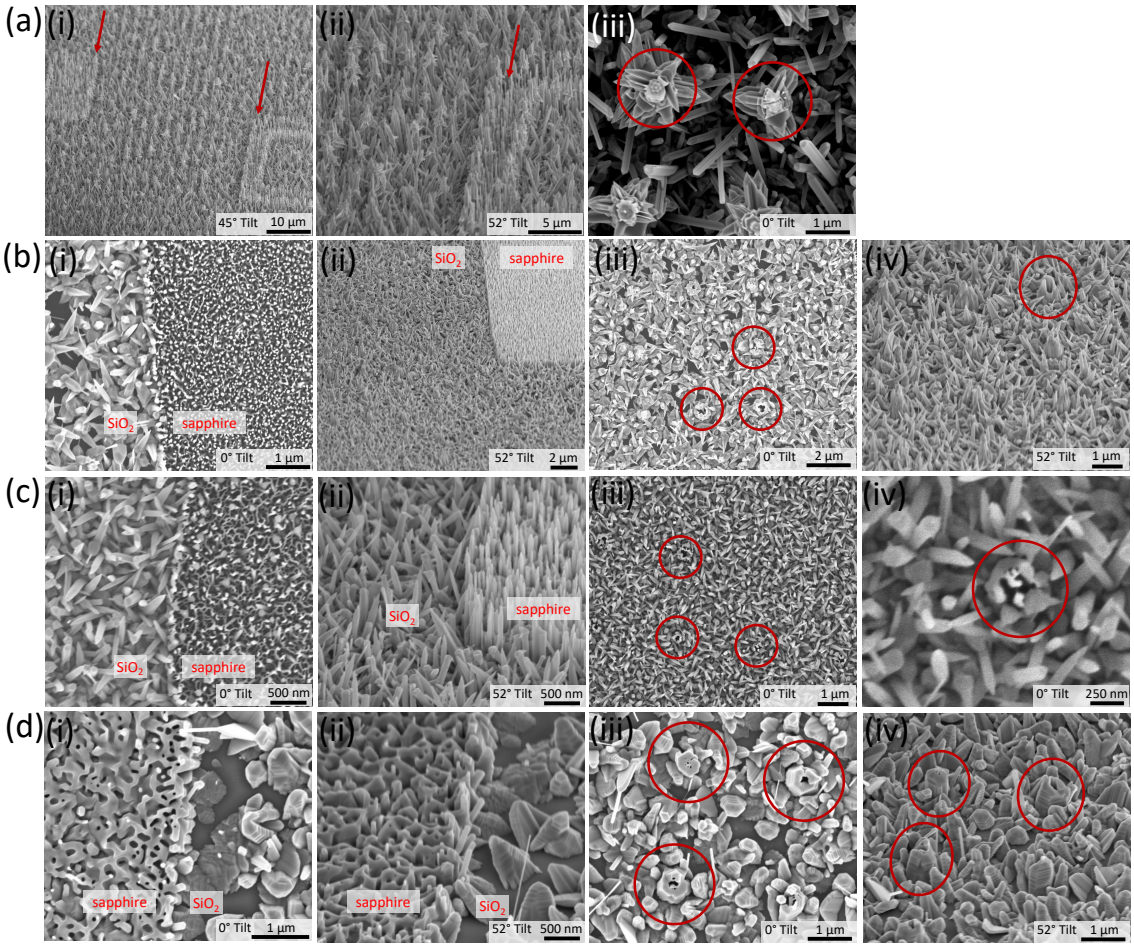

Figure 5.4: SEM images of several growth attempts. The positions of some holes are indicated with red circles. The edges of some large markers are indicated with red arrows. All of the samples are on a patterned SiO_2 substrate. The growths all occur with a DMZn flow rate of 2.24×10^{-5} mol/min and a N_2O flow rate of 1.3×10^{-1} mol/min. Each growth is followed by a 2 min post-anneal under N_2O at the growth temperature. Each row of the figure includes images from different locations or angles of the same sample. (a) Sample H1068 - Anneal at 605°C under N_2O for 5 min. Growth at 605°C for 60 min. (b) Sample H1070 - Anneal at 605°C under N_2O for 20 min. Growth at 605°C for 15 min. (c) Sample H1071 - Anneal at 905°C under O_2 for 20 min. Growth at 605°C for 15 min. (d) Sample H1073 - Anneal at 905°C under O_2 for 20 min. Growth at 705°C for 15 min.

meet our goal of reducing the volume of material within our laser spot by growing less dense nanowires. However, the fact that the holes produce the large flower-shaped nanowires indicates that the nanowires in the holes nucleated before those on the mask. To check where

the nucleation occurs first, a 15 min growth with the same parameters is performed. We see in Fig. 5.4(b) that even after only 15 min of growth, nucleation occurs on both the sapphire and the SiO_2. Fig. 5.4(b.i, b.ii) show that the nanowires on the large exposed-sapphire marker are much smaller in diameter and more densely packed than those on the SiO_2. In Fig. 5.4(b.iii, b.iv), the holes are circled in red and show slightly enhanced growth only at their perimeters.

We have several parameters available to tune (temperature, reactant molar flow rates, substrate mask material, and pre-anneal conditions). We begin by adjusting the pre-anneal from 20 min at 605°C under N_2O to 20 min at 905°C under O_2. Comparing Fig. 5.4(c) to Fig. 5.4(b) shows that changing these pre-anneal conditions has little impact on the selectivity between the sapphire and SiO_2. We then slightly increase the growth temperature from 605°C to 705°C. In Fig. 5.4(d.i, d.ii) we see that the desired selectivity has slightly increased, as large regions without ZnO are visible on the SiO_2; the ZnO appears to form larger chunks as opposed to nanowires. However, the morphology of the nanostructures on the sapphire has also changed, in that nanowalls are more prevalent than nanowires. In the regions with exposed-sapphire holes, shown in Fig. 5.4(d.iii, d.iv), the increased nucleation near the edges of the holes is still apparent, but there are few denuded regions on the SiO_2.

These preliminary selective area growth attempts show us that the standard nanowire growth recipe does not lead to full selectivity between the sapphire and SiO_2; however, we see that the selectivity can be tuned. Because of the labor intensive nature of making the patterned substrates, we then perform two careful studies on unpatterned substrates. These systematic studies focus on temperature and growth rate, because these parameters have been shown to control desorption and diffusion, respectively [37, 36, 41].

Growth Rate

To test the importance of adatom surface diffusion for selective area growth, we would like to control the growth rate [36]. Because of the high VI/II ratio that we use (mol(O)/mol(Zn) = 5800), Zn is likely the limiting reagent; therefore, we can control the growth rate by changing the flow of Zn. We are also interested if there is a difference between the growths

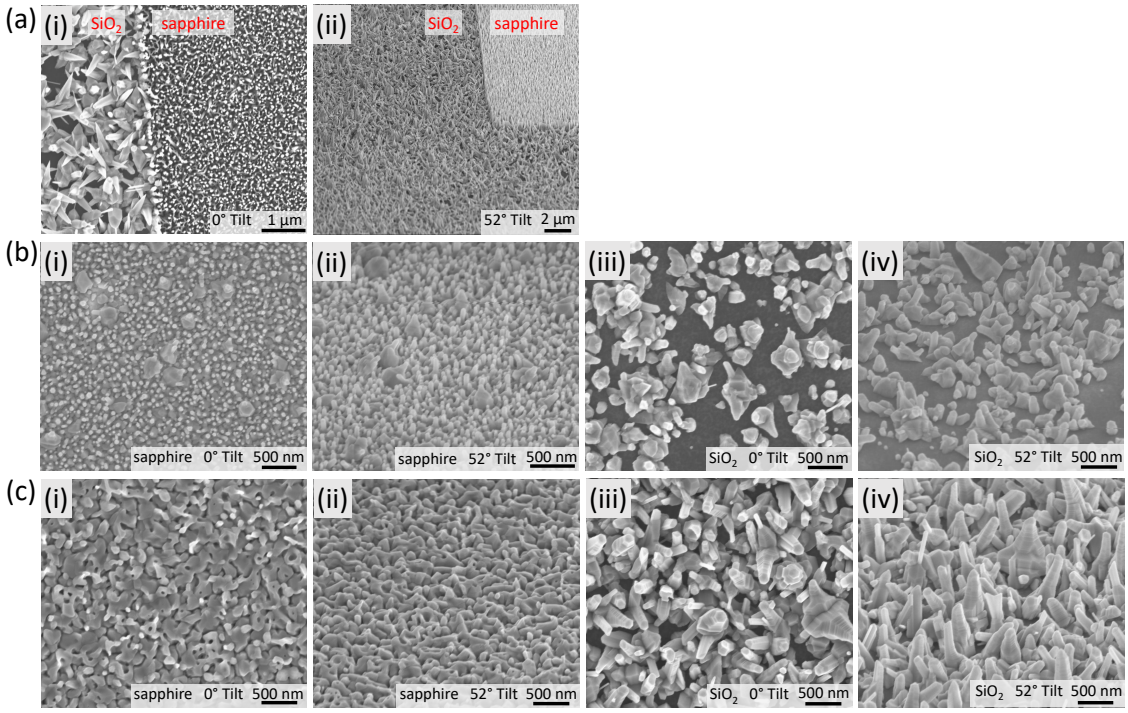

Figure 5.5: All growths are performed at 605°C with a N_2O flow rate of 1.3×10^{-1} mol/min. Before all growths, a 20 min pre-anneal is performed at 605°C under N_2O. After all growths, a 2 min post-anneal is performed at 605°C under N_2O. (a) Sample H1070 - 15 min growth with a standard DMZn flow rate of 2.24×10^{-5} mol/min. In (i, ii), a large marker of exposed sapphire is visible on the right. (b) Sample H1073 - 15 min growth with a reduced DMZn flow rate of 7.47×10^{-6} mol/min. (c) Sample H1074 - 45 min growth with a reduced DMZn flow rate of 7.47×10^{-6} mol/min.

on sapphire and SiO_2 at different growth rates. Our standard ZnO-nanowires are grown with 2.24×10^{-5} mol/min of DMZn. To test the effect of Zn flow on the growth rate and selectivity, we decreasing the Zn flow by about 3x to 7.47×10^{-6} mol/min. Fig. 5.5(a,b) show 15 min growths with (a) 2.24×10^{-5} mol/min and (b) 7.47×10^{-6} mol/min of DMZn. As before, we see in Fig. 5.5(a) that the structures are bigger and less dense on SiO_2 compared to the sapphire. With the slower growth rate, we see the the difference between the growth on sapphire (Fig. 5.5(b.i, b.ii)) and SiO_2 (Fig. 5.5(b.iii, b.iv)) is even more pronounced. This speaks to reduced wetting of the SiO_2 which may be a promising result.

To test for other changes caused by reducing the flow rate (for example morphology), we

would like to grow the same volume of ZnO at the fast and slow growth rates. Therefore, assuming that the growth rate is directly proportional to the Zn flow, we can grow the same volume of ZnO seen in Fig. 5.5(a) by growing for 45 min with 7.47×10^{-6} mol/min of DMZn (Fig. 5.5(c)). While we expected similar structures, the morphology of the nanostructures has changed. Rather than structures with sharp points at the top, the structures grown with a slower growth rate look more like nanowalls (on sapphire, Fig. 5.5(c.i, c.ii)) or blunt rods (on SiO_2, Fig. 5.5(c.iii, c.iv)). This may be a problem if the new morphology introduces strain to the ZnO. However, if the slower growth rate allows for the diffusion of adatoms to exposed sapphire and aids in the selectively of growth, then the slower growth rate may be preferred.

Temperature Dependence

An important factor in the selective area growth of GaAs is the desorption of adatoms, which can be controlled by the growth temperature [36]. To test the importance of desorption for ZnO selective area growth and to find the growth temperature most favorable for growth selectivity between sapphire and SiO_2/SiN_x, we performed a systematic growth-temperature study. We loaded 3 unpatterned substrates into the sample chamber during each growth: 1 bare sapphire, 1 SiO_2-covered sapphire, and 1 SiN_x-covered sapphire. The bare sapphire and SiN_x substrates had only been cleaned with acetone. All of the SiO_2 substrates had been coated in PMMA and gold, then cleaned with acetone. The SiO_2 substrate used for the growth at 605°C had a little exposed sapphire, but only regions far from the exposed-sapphire areas were considered in this study. 15 min growths were performed at the reduced growth rate (7.47×10^{-6} mol/min of DMZn, standard N_2O flow). Our aim was to see how the ZnO nucleates, rather than grow full nanowires. We were hoping for poor coverage on either the SiO_2 or the SiN_x substrates at some temperature.

Fig. 5.6 and Fig. 5.7 show the results of our study. They show representative SEM images of each of the samples at 25 kX (Fig. 5.6) and 80 kX (Fig. 5.7) magnification. There was some non-uniformity in the density of nucleation across some samples. For such non-uniform samples, two SEM images are shown. For each growth temperature, the SiN_x substrate

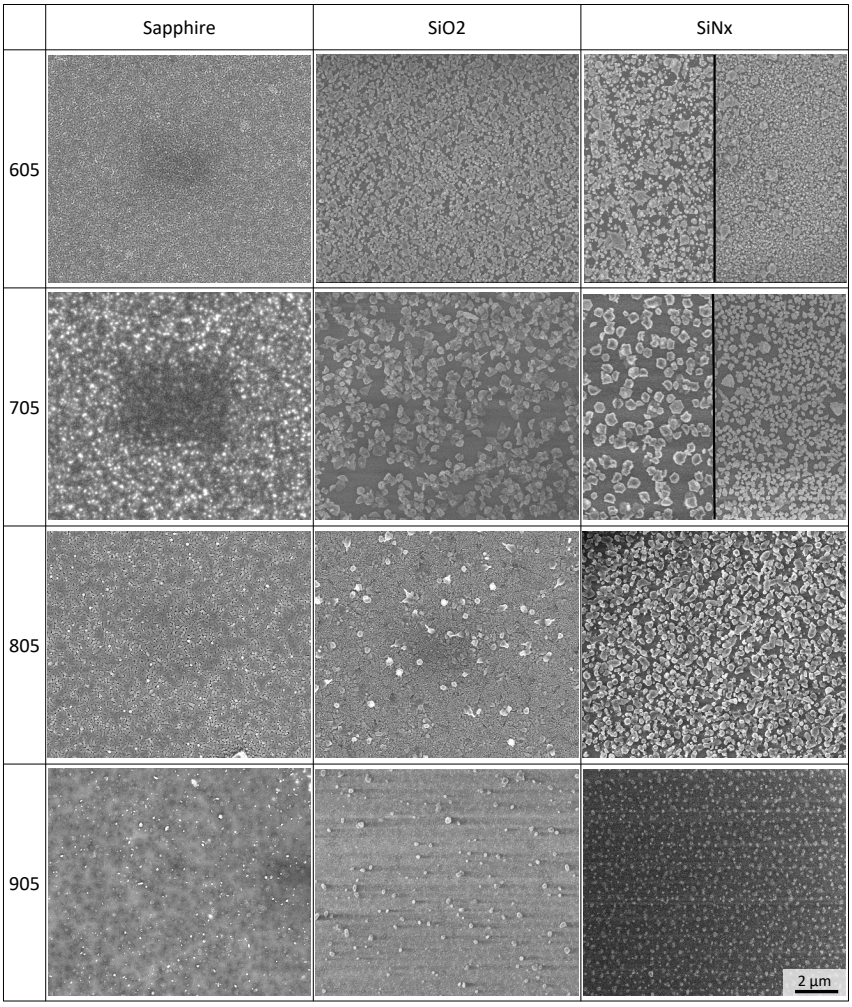

Figure 5.6: 25 kX magnification SEM images of different samples. The columns correspond to ZnO grown on Sapphire, SiO_2, or SiN_xsubstrates, respectively. The rows correspond to different growth temperatures, 605, 705, 805, and 905°C, respectively. All growths are performed with a 20 min pre-anneal under N_2O at the growth temperature, a 15 min growth with a N_2O flow rate of 1.3×10^{-1} mol/min and a reduced DMZn flow rate of 7.47×10^{-6} mol/min, and a 2 min post-anneal under N_2O at the growth temperature.

shows the least uniform wetting and the sapphire typically shows the most uniform wetting. On all of the SiN_x-substrate samples, the ZnO has grown in large chunks with the growth at 705°C having the largest ZnO chunks. For the SiN_x-substrate sample grown at 905°C, it was challenging to image the sample because of charging caused by electron accumulation;

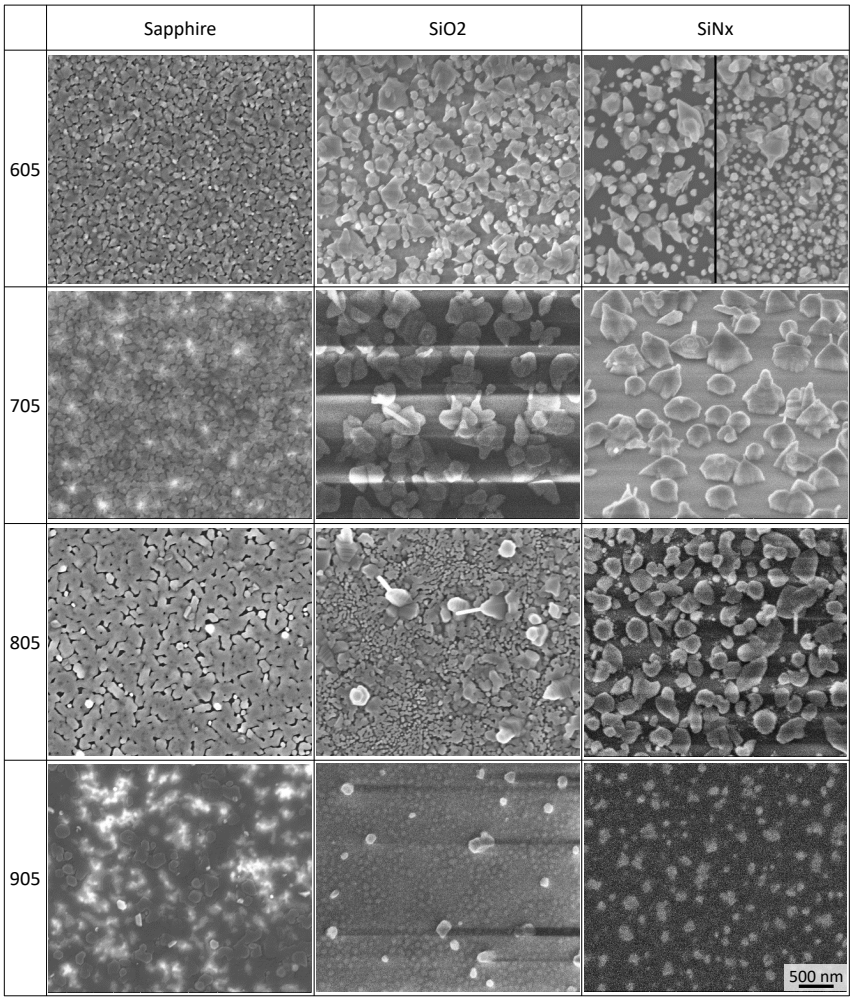

Figure 5.7: 80 kX magnification SEM images of different samples. The columns correspond to ZnO grown on Sapphire, SiO_2, or SiN_xsubstrates, respectively. The rows correspond to different growth temperatures, 605, 705, 805, and 905°C, respectively. These are the same samples as in Fig. 5.6 with a different imaging magnification; see Fig. 5.6 for growth details.

though, it appears that there are still large chunks in the growth. Charging may indicate reduced ZnO wetting, because charging is expected from samples with large areas of low coverage of ZnO (conductive) on sapphire (insulting). The SiO_2-substrate samples grown at 605°C and 705°C behave similarly to the SiN_x-substrate samples, though the non-uniform wetting is less pronounced. The SiO_2-substrate samples grown at the higher temperatures have large chunks in addition to a floor of more uniform ZnO nucleation. Interestingly,

on the sapphire-substrate samples, while the nucleation appears to remain uniform, the morphology becomes more planar with higher growth temperatures. Based on these results, we will focus on growths using the SiN_x substrates with growth temperatures of 705°C and 905°C.

Final Growths

Based on the findings of the temperature study, we focus our final growths on the SiN_x-patterned substrates. For comparison with the SiO_2-patterned substrates (Fig. 5.4), we perform a growth using the standard growth temperature (605°C) and DMZn molar flow rate (2.24×10^{-5} mol/min). Fig. 5.8(a) shows that, as indicated by the temperature test, the SiN_x-patterned substrate shows less uniform wetting than the SiO_2-patterned substrate grown with the same conditions (Fig. 5.4(b)). However, the rate of nucleation on the SiN_x is still too high to allow for the optical isolation of nanowires.

We then try a growth at one of the most promising temperatures from our temperature test (905°C) and with the slow growth rate (7.47×10^{-6} mol/min). Fig. 5.8(b) shows that this growth also has some selectivity between the sapphire and SiN_x. The large exposed-sapphire marker in Fig. 5.8(b.i, b.ii) and the small exposed-sapphire hole in Fig. 5.8(b.iii, b.iv) show reasonably uniform nucleation of many small nanostructures. While much of the SiN_x is visible in the masked regions, the ZnO nucleation is still too dense to allow for optical isolation.

We then try growths at several different growth rates. In Fig. 5.8(c), the growth rate has been increased 2.67x to 19.94×10^{-6} mol/min. In Fig. 5.8(c.i, c.ii), we see that while the nanowires that grow on the SiN_x are much less well aligned, there is little selectivity between the sapphire and the SiN_x. Fig. 5.8(c.iii, c.iv) shows that the holes somewhat orient the nanowires, but overall do not substantially affect the nanowire growth. To reduce the growth rate below our reactor's lowest DMZn flow rate (7.47×10^{-6} mol/min), we pulse the growth (30 s on, 30 s off). Fig. 5.8(d) shows that in this case, there is so little selectivity between the sapphire and the SiN_x that it is challenging to differentiate between the two when zoomed-in.

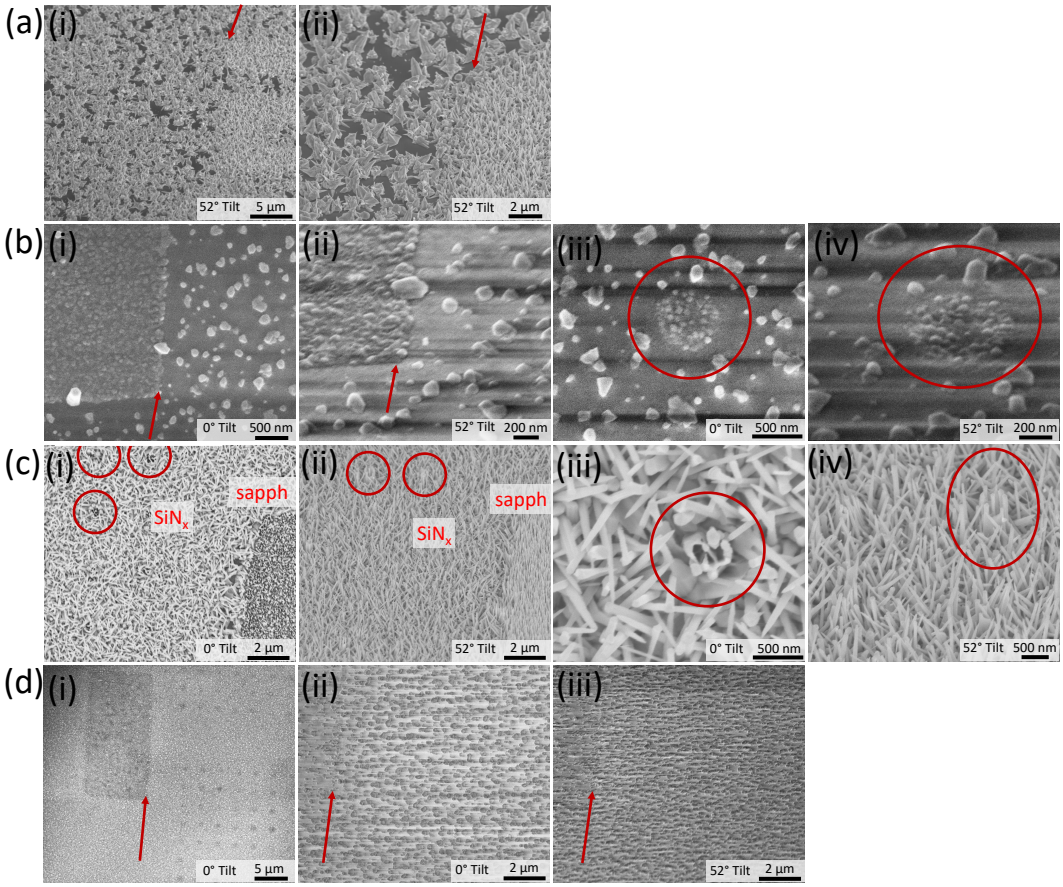

Figure 5.8: All samples use the patterned SiN_x substrate. All growths performed with a standard N_2O flow rate of 1.3×10^{-1} mol/min. The circled features are related to the locations of holes of exposed sapphire. (a) Sample H1069 - Pre-anneal at 605°C under N_2 for 10 min. 15 min growth at 605°C with a standard 2.24×10^{-5} mol/min DMZn flow rate. No post-anneal. The arrow indicates the top left corner of a large "2"-label. (b) Sample H1080 - Pre-anneal at 905°C under N_2O for 20 min. 15 min growth at 905°C with a reduced 7.47×10^{-6} mol/min DMZn flow rate. Post-anneal at 905°C under N_2O for 2 min. (c) Sample H1084 - Pre-anneal at 605°C under N_2O for 20 min. 15 min growth at 605°C with a fast $2.67 \times 7.47 \times 10^{-6}$ mol/min DMZn flow rate. Post-anneal at 905°C under N_2O for 2 min. (d) Sample H1086 - Pre-anneal at 905°C under N_2O for 20 min. Growth at 705°C with a reduced 7.47×10^{-6} mol/min DMZn flow rate. The average growth rate was further reduced by growing for 30 s with 30 s of no growth in between for 60 cycles. Post-anneal at 905°C under N_2O for 2 min. The arrow indicates the bottom right corner of a large rectangular marker.

5.3.4 Conclusions

After scanning the growth-parameter space using both patterned and unpatterned substrates, we conclude that we have some control over the selectivity of ZnO growth on sapphire compared to ZnO growth on SiO_2/SiN_x. However, we are unable to find a combination of parameters that would reduce the growth on the mask material enough for the fully-selective growth necessary for us to optically isolate individual nanowires. While methods using a ZnO wetting layer have been successful [104], they do not fully meet our goal of reducing the volume of ZnO within our measurement volume. Additionally, methods that involve more elaborate substrates, such as growing nanowires on the tips of GaN micropyramids [39], have shown to be successful, but are beyond the scope of this thesis.

5.4 Core-Shell Growths

5.4.1 Introduction

Another challenge that we hope to overcome using a non-standard growth is the surface exciton (SX) that can be seen in some of the spectra in Fig. 2.3. The SX is a large power-dependent feature that is related to excitons bound to surface centers [106, 117]. Studies have shown that it may be related to adsorbed OH species [10] or near surface band bending [106, 50]. We are concerned about the SX, because it overlaps spectrally with the D^0X lines. While for our current measurements, we can still observe our defects of interest, as we move toward the single-donor limit needed for quantum applications, the SX may begin to obscure our defect entirely. Additionally, it will lower the fidelity with which we can read-out our qubit state. To overcome this challenge, we propose to grow a $Zn_{1-x}Mg_xO$ shell on the ZnO nanowires.

We predict that the $Zn_{1-x}Mg_xO$ shell will help by first terminating the unterminated ZnO surface. MgO, while favoring the rocksalt crystal structure on its own, assumes the wurtzite crystal structure when alloyed with ZnO, because the formation energies of MgO-ZnO alloy structures in the the wurtzite structure are similar [3]. Having a similar crystal structure provides the opportunity to nicely terminate the ZnO surface, but makes it likely that the $Zn_{1-x}Mg_xO$ shell will also have a SX. To understand how a $Zn_{1-x}Mg_xO$ shell would

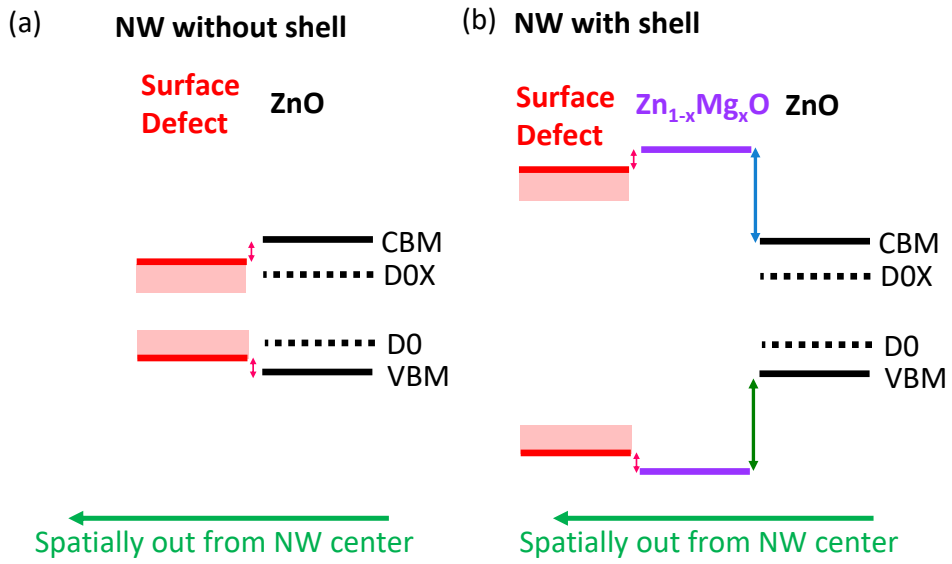

Figure 5.9: Energy level diagram showing how we predict the SX energy is related to the band gap and D^0X energies (a) without and (b) with a $Zn_{1-x}Mg_xO$ shell.

help, we note that we expect the energy level of the SX to be related to the energy level of the conduction band minimum (CBM) and valence band maximum (VBM) as shown in Fig. 5.9 (a). Since the SX is bound to surface features [106, 117], its energy is determined by the CBM and VBM of the ZnO near the surface of the nanowires. Therefore, if we grow a shell on the nanowires with a band gap larger than that of ZnO, we predict that we can shift the SX energy away from the D^0X lines as shown in Fig. 5.9 (b). $Zn_{1-x}Mg_xO$ is commonly used in the band gap engineering of ZnO toward higher energies [3, 104]. Additionally, significant work has already been done on the growth [104, 123] and modeling [66] of $ZnO/Zn_{1-x}Mg_xO$ core/shell heterostructures. To shift the energy of the SX enough to avoid the D^0X transitions, we need to increase the band gap of the the $Zn_{1-x}Mg_xO$ shell 15-20 meV above the band gap of ZnO. Based on the work of [76, 104] and extrapolated from [123, 1, 101], a 15-20 meV shift corresponds to 1-2% Mg incorporation; however, the percent Mg incorporation is much less than the percent of Mg present in the gas phase [104].

5.4.2 Growth Round 1

We begin experimenting with $Zn/Zn_{1-x}Mg_xO$ core/shell nanowires by performing three growths. In all of these samples, we start with a standard nanowire growth, then attempt to grow the $Zn_{1-x}Mg_xO$ shell as described in table 5.1. For the first sample (H1088), we begin with a growth that is similar to our standard growth, but with DMZn replaced by a combination of DEZn and Cp2Mg. In the second sample (H1090), we change the O precursor from N_2O to O_2. The authors of [104] found that using O_2 produces more uniform shells. In the third sample (H1092), we decrease the IV/II ratio by decreasing the flow of O_2. Before, after, and between these growths, we prepare a standard nanowire sample (i.e. without a $Zn_{1-x}Mg_xO$ shell).

Sample	DEZn	Cp2Mg	O precursor	Temperature	Time
H1088	1.82	0.20	N_2O, 1.3e5	605°C	30 min
H1090	0.52	0.25	O_2, 1.0e4	505°C	60 min
H1092	0.52	0.25	O_2, 5.0e3	505°C	60 min

Table 5.1: Growth parameters for shells of the first round of $Zn/Zn_{1-x}Mg_xO$ core/shell samples. All shells are grown on top of standard ZnO nanowires. The molar flow rates of DEZn, Cp2Mg, and the O precursor are reported with units of µmol/min.

Fig. 5.10 shows several SEM images of the core-shell sample H1088 and its preceding standard growth H1087 for comparison. The core-shell sample shows a slight increase in diameter near the top of nanowires, but otherwise appears normal in morphology.

Photoluminescence measurements are used to check for Mg incorporation (Fig. 5.11). Samples H1088 and H1090 display a peak at 3398.5 meV and 3388.0 meV, respectively, that can be attributed to the formation of a $Zn_{1-x}Mg_xO$ shell. Based on the work of [76, 104], these samples have ∼1% Mg incorporation. Sample H1092 does not have this peak.

For all three of the core-shell samples, the SX is still there, suggesting that whatever is causing the SX is still at the interface between the core and the shell. Other groups have even seen increases in the SX after coating ZnO nanowires [89]. Another possible reason for

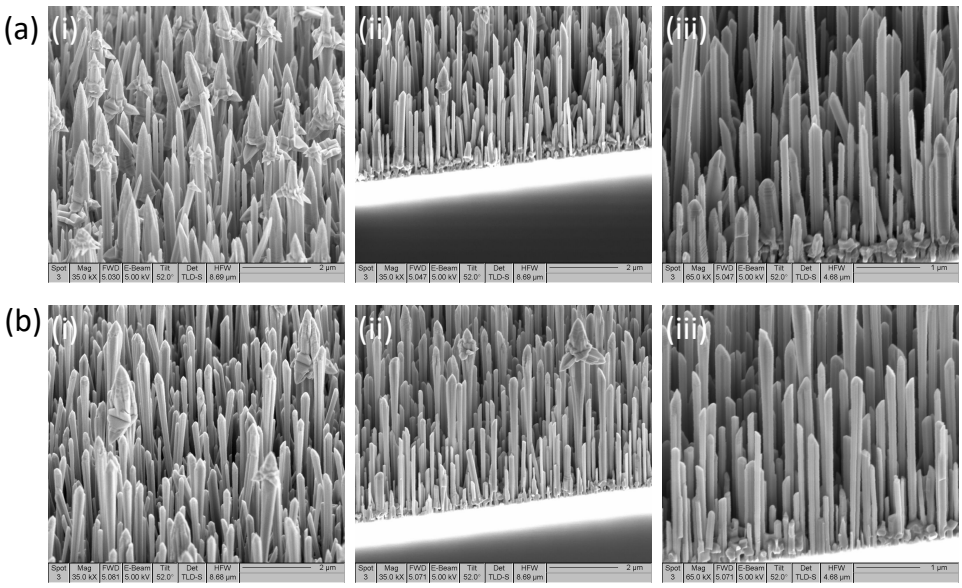

Figure 5.10: SEM images of a (a) standard ZnO nanowire sample (H1087) and a (b) $Zn/Zn_{1-x}Mg_xO$ core/shell sample (H1088)

the simultaneous presence of the $Zn_{1-x}Mg_xO$ peaks (at 3398.5 meV and 3388.0 meV) and the SX peaks is that the shells have some aggregated regions of $Zn_{1-x}Mg_xO$ and regions where pure ZnO is exposed [104]. However, promisingly there is some shift of the SX energy compared to a standard nanowire sample (i.e. from 3365.5 meV to 3369.2 meV). Because the SX did not shift as much as we were expecting, we plan to increase our Mg/Zn ratio in our next round of growths. Furthermore, sample H1088 had the strongest $Zn_{1-x}Mg_xO$ peak though it had the lowest Cp2Mg flow rate; therefore, we focus on growth recipes using N_2O.

5.4.3 Growth Round 2

For this round of growths, we keep the time, temperature, and N_2O flow of the shell growth constant, while changing the mole fraction of Mg in the gaseous phase. Fig. 5.12(a) shows photoluminescence (PL) measurements for core-shell samples with four different gaseous mole fractions of Mg ($mol_{Mg}/(mol_{Zn} + mol_{Mg})$ = 0.530, 0.393, 0.181, or 0.302). There is still little change in the spectral position of the SX. This indicates that either the molar ratio

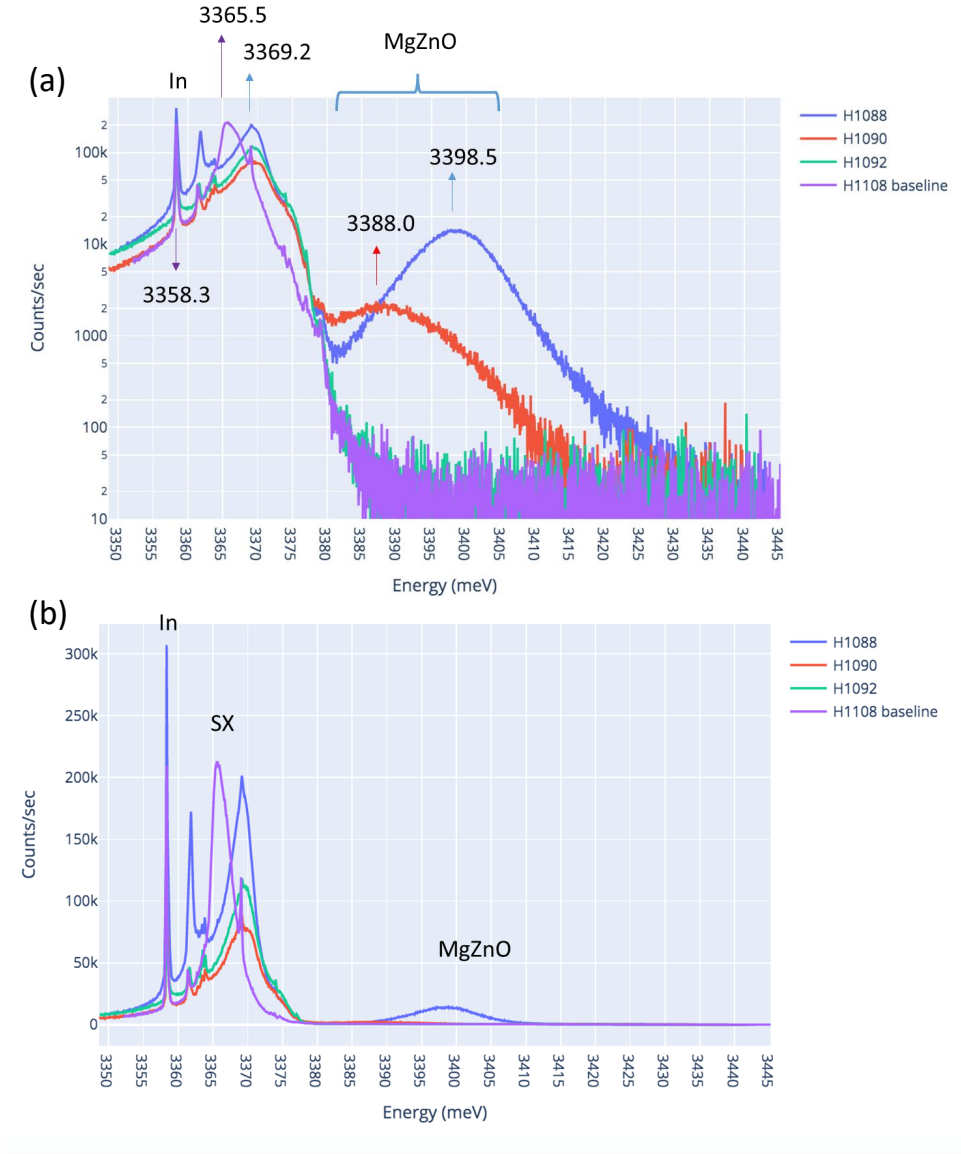

Figure 5.11: PL measurements of $Zn/Zn_{1-x}Mg_xO$ core/shell samples (H1088, H1090, H1092) and a standard growth nanowire sample (H1108). Plots are shown on (a) log and (b) linear scales. The centers of the peaks are indicated in (a).

of Mg to Zn in the gaseous phase does not correlate with the molar ratio incorporated into the $Zn_{1-x}Mg_xO$ shell or that the spectral position of the SX is independent of the band gap of the shell. Additionally, the linewidth of the SX increases as more growths are performed, independent of the Mg/Zn molar ratio. Fig. 5.12(b) compares the core-shell samples to the

standard nanowire growth samples performed around the same time. Notably, the SX is larger in all of the core-shell samples. We therefore conclude that the core-shell method does not look like a promising avenue to remove the SX. It appears that the SX may exist at the ZnO/$Zn_{1-x}Mg_xO$ interface or that we have not achieved a uniform $Zn_{1-x}Mg_xO$ shell.

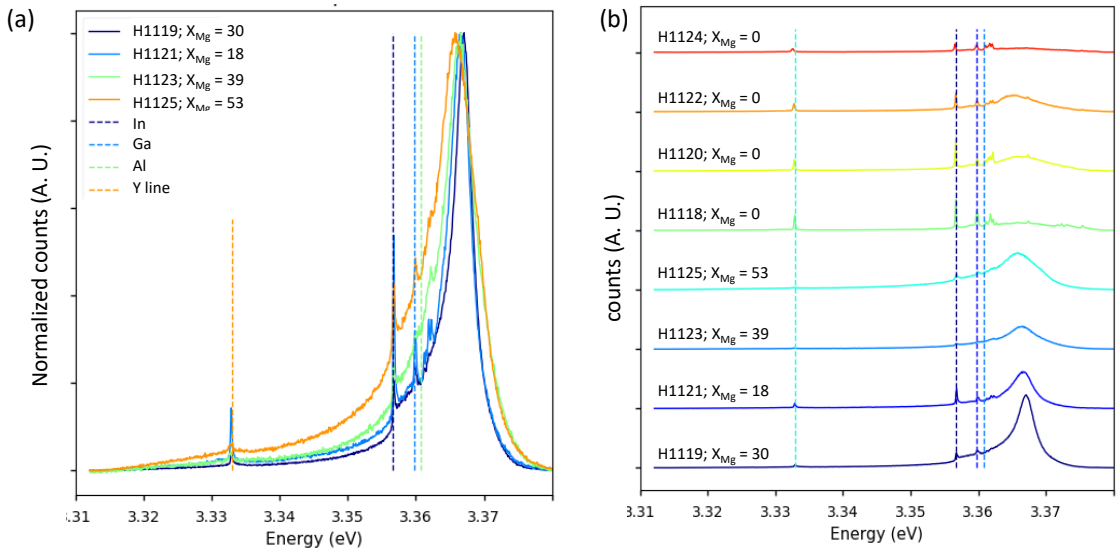

Figure 5.12: PL measurements of the second round of Zn/$Zn_{1-x}Mg_xO$ core/shell samples. The legend indicates the sample name and the mole fraction of Mg in the gaseous phase. (a) Spectra are normalized for ease of comparison. The spectral maximum of the SX does not shift as much as expected. The linewidth increases with growth number, independent of Mg mole fraction. (b) Both Zn/$Zn_{1-x}Mg_xO$ core/shell samples and the standard growth samples that were performed around the same time. Spectra are offset for clarity.

5.5 Summary

There are several outstanding challenges for the use of ZnO nanowires for quantum applications. In this chapter, we have attempted to tackle two of them using some non-standard growth methods. First, selective area growth was attempted to ease the isolation of single nanowires and their incorporation into devices. While some selectivity between sapphire and a mask material (SiO_2 or SiN_x) was seen, we have yet to find a set of parameters that result in the selectivity needed for nanowire isolation. It may be necessary to move toward

more advanced methods for fully deterministic growth of single nanowires. Additionally, a $Zn/Zn_{1-x}Mg_xO$ core/shell structure was attempted to shift the spectral position of the surface exciton (SX) away from the D^0X lines. Indications of Mg incorporation were seen in photoluminescence measurements; however, the SX did not shift as expected and appeared larger in the core/shell samples. This could suggest that the SX can exist at the core/shell interface or that a true core/shell structure was not formed. To further this work, future studies must include TEM measurements to confirm the growth of the shell.

Chapter 6

CONCLUSIONS AND OUTLOOK

This work considers the potential to utilize donor defects in ZnO for photon-based quantum applications. Our earlier works [60, 58] have found that ensembles of donors in bulk ZnO show favorable optical and spin properties, such as long spin coherence times and optical spin control. However, most quantum applications will require the isolation of single defects and their integration into nanoscale devices. Toward these requirements, the main goals of this work were to:

- move toward smaller ensembles of donors as a stepping stone toward single defect isolation
- show that there is nothing fundamental limiting the incorporation of donors into nanoscale devices
- begin addressing some of the outstanding challenges for the use of ZnO nanostructures in applications

To achieve these goals, we began with ZnO nanowires grown by our collaborator Simon Watkins at Simon Fraser University. These microstructures exhibited many favorable optical and spin properties comparable to those in bulk samples; however, these nanowires grow in a dense ensemble. To further reduce the amount of material within our measurement volume, we perform several methods of single nanowire isolation including scanning electron microscopy using ZnO/GaN samples, ion beam milling, exfoliation, and dropcasting (Ch. 3). While ion beam milling and exfoliation damaged the optical properties of the nanowires in all of the attempts, some of the ZnO/GaN samples and dropcast samples retained favorable photoluminescence spectra. Taking the most promising of those samples, we then demonstrate that favorable spin properties are also retained in these nanostructure environments (Ch. 4). Photoluminescence excitation spectroscopy confirms narrow optical lines, optical pumping allows for spin initialization, and coherent spin trapping demonstrates

the preparation of a superposition state. Finally, we attempt several non-standard growths to achieve the isolation of nanowires and shifting of the surface exciton (Ch. 5). While these attempts were not immediately successful, the work done here has provided a starting point for further study.

Due to the promising optical and spin characteristics observed in Ch. 4, shallow donors in ZnO warrant further study for quantum applications and our group is pursuing several exciting next steps. To achieve the isolation of a single defect, we are looking at moving toward less prevalent defects. For example, two lattice site defects, such as the tin complex in ZnO [51], lead to the formation of fewer defects, therefore have a lower density, and would make single defect isolation easier. This defect is also further from the band edge and surface exciton. Additionally, direct microwave control of the electron spin, rather than optical control, would reduce the effects of laser-induced dephasing. We could be able to achieve narrower linewidths in single nanowires and full access of the Bloch sphere. Thus, this work is one step in the larger story of using donors in ZnO for quantum applications.

BIBLIOGRAPHY

[1] Arpana Agrawal, Tanveer Ahmad Dar, D. M. Phase, and Pratima Sen. Type I and type II band alignments in ZnO/MgZnO bilayer films. *Applied Physics Letters*, 105:081603, 2014.

[2] Shunsuke Akasaka, Ken Nakahara, Atsushi Tsukazaki, Akira Ohtomo, and Masashi Kawasaki. $Mg_xZn_{1-x}O$ films with a low residual donor concentration ($< 10^{15}$ cm^{-3}) grown by molecular beam epitaxy. *Applied Physics Express*, 3:071101, 7 2010.

[3] H. Algarni, A. Gueddim, N. Bouarissa, M. Ajmal Khan, and H. Ziani. Crystal structure and electronic properties of wurtzite $Mg_xZn_{1-x}O$: Ab initio study. *Results in Physics*, 15:102694, 12 2019.

[4] Jonathan Allcock, Anna Vangone, Agnes Meyder, Stanislaw Adaszewski, Martin Strahm, Chang-Yu Hsieh, and Shengyu Zhang. Antibody loop modelling on a quantum computer. *arXiv*, 5 2021.

[5] Frank Arute, Kunal Arya, Ryan Babbush, Dave Bacon, Joseph C. Bardin, Rami Barends, Rupak Biswas, Sergio Boixo, Fernando G.S.L. Brandao, David A. Buell, Brian Burkett, Yu Chen, Zijun Chen, Ben Chiaro, Roberto Collins, William Courtney, Andrew Dunsworth, Edward Farhi, Brooks Foxen, Austin Fowler, Craig Gidney, Marissa Giustina, Rob Graff, Keith Guerin, Steve Habegger, Matthew P. Harrigan, Michael J. Hartmann, Alan Ho, Markus Hoffmann, Trent Huang, Travis S. Humble, Sergei V. Isakov, Evan Jeffrey, Zhang Jiang, Dvir Kafri, Kostyantyn Kechedzhi, Julian Kelly, Paul V. Klimov, Sergey Knysh, Alexander Korotkov, Fedor Kostritsa, David Landhuis, Mike Lindmark, Erik Lucero, Dmitry Lyakh, Salvatore Mandrà, Jarrod R. McClean, Matthew McEwen, Anthony Megrant, Xiao Mi, Kristel Michielsen, Masoud Mohseni, Josh Mutus, Ofer Naaman, Matthew Neeley, Charles Neill, Murphy Yuezhen Niu, Eric Ostby, Andre Petukhov, John C. Platt, Chris Quintana, Eleanor G. Rieffel, Pedram Roushan, Nicholas C. Rubin, Daniel Sank, Kevin J. Satzinger, Vadim Smelyanskiy, Kevin J. Sung, Matthew D. Trevithick, Amit Vainsencher, Benjamin Villalonga, Theodore White, Z. Jamie Yao, Ping Yeh, Adam Zalcman, Hartmut Neven, and John M. Martinis. Quantum supremacy using a programmable superconducting processor. *Nature*, 574:505–510, 2019.

[6] M. Aspelmeyer, T. Jennewein, M. Pfennigbauer, W.R. Leeb, and A. Zeilinger. Long-distance quantum communication with entangled photons using satellites. *IEEE Journal of Selected Topics in Quantum Electronics*, 9(6):1541–1551, 2003.

[7] Vitaliy Avrutin, Gene Cantwell, Jizhi Zhang, J. J. Song, Donald J. Silversmith, and Hadis Morkoç. Bulk ZnO: Current status, challenges, and prospects. *Proceedings of the IEEE*, 98:1339–1350, 2010.

[8] Simon C. Benjamin, Brendon W. Lovett, and Jason M. Smith. Prospects for measurement-based quantum computing with solid state spins. *Laser and Photonics Reviews*, 3:556–574, 2009.

[9] Charles H. Bennett, Gilles Brassard, and Jean-Marc Robert. How to reduce your enemy's information (extended abstract). In Hugh C. Williams, editor, *Advances in Cryptology — CRYPTO '85 Proceedings*, pages 468–476, Berlin, Heidelberg, 1986. Springer Berlin Heidelberg.

[10] Mahua Biswas, Yun Suk Jung, Hong Koo Kim, Kumarappan Kumar, Gregory J. Hughes, S. Newcomb, Martin O. Henry, and Enda McGlynn. Microscopic origins of the surface exciton photoluminescence peak in ZnO nanostructures. *Physical Review B*, 83:235320–235330, 2011.

[11] D Block, A Hervé, and R T Cox. Optically detected magnetic resonance and optically detected endor of shallow indium donors in ZnO. *Physical Review B*, 25:6049–6052, 1982.

[12] Reinhold Blümel, Nikodem Grzesiak, Nhung H. Nguyen, Alaina M. Green, Ming Li, Andrii Maksymov, Norbert M. Linke, and Yunseong Nam. Efficient stabilized two-qubit gates on a trapped-ion quantum computer. *Physical Review Letters*, 126:220503–220509, 6 2021.

[13] D. Brunner, B. Gerardot, P. Dalgarno, G. Wust, K. Karrai, N. Stoltz, P. Petroff, and R. Warburton. A coherent single-hole spin in a semiconductor. *Science*, 325:70–72, 11 2009.

[14] Srivatsa Chakravarthi, Christian Pederson, Zeeshawn Kazi, Andrew Ivanov, and Kai-Mei C. Fu. Impact of surface and laser-induced noise on the spectral stability of implanted nitrogen-vacancy centers in diamond. *Physical Review B*, 104, 8 2021.

[15] Susan M. Clark, Kai Mei C. Fu, Qiang Zhang, Thaddeus D. Ladd, Colin Stanley, and Yoshihisa Yamamoto. Ultrafast optical spin echo for electron spins in semiconductors. *Physical Review Letters*, 102:3–6, 2009.

[16] Lobna Dallali, Sihem Jaziri, Jamal El Haskouri, and Pedro Amorós. Optical properties of exciton confinement in spherical ZnO quantum dots embedded in SiO_2 matrix. *Superlattices and Microstructures*, 46:907–916, 12 2009.

[17] Aymeric Delteil, Zhe Sun, Wei bo Gao, Emre Togan, Stefan Faelt, and Ataç Imamoglu. Generation of heralded entanglement between distant hole spins. *Nature Physics*, 12:218–223, 12 2015.

[18] L. Ding, B. K. Li, H. T. He, W. K. Ge, J. N. Wang, J. Q. Ning, X. M. Dai, C. C. Ling, and S. J. Xu. Classification of bound exciton complexes in bulk ZnO by magnetophotoluminescence spectroscopy. *Journal of Applied Physics*, 105:053511, 2009.

[19] Marcus W. Doherty, Neil B. Manson, Paul Delaney, Fedor Jelezko, Jörg Wrachtrup, and Lloyd C.L. Hollenberg. The nitrogen-vacancy colour centre in diamond. *Physics Reports*, 528:1–45, 7 2013.

[20] F. Dolde, I. Jakobi, B. Naydenov, N. Zhao, S. Pezzagna, C. Trautmann, J. Meijer, P. Neumann, F. Jelezko, and J. Wrachtrup. Room-temperature entanglement between single defect spins in diamond. *Nature Physics*, 9:139–143, 2013.

[21] L-m Duan, M D Lukin, J I Cirac, and P Zoller. Long-distance quantum communication with atomic ensembles and linear optics. *Nature*, 414:413–418, 2001.

[22] Laird Egan, Dripto M. Debroy, Crystal Noel, Andrew Risinger, Daiwei Zhu, Debopriyo Biswas, Michael Newman, Muyuan Li, Kenneth R. Brown, Marko Cetina, and Christopher Monroe. Fault-tolerant control of an error-corrected qubit. *Nature*, 598:281–286, 10 2021.

[23] S. A. Empedocles and M. G. Bawendi. Influence of spectral diffusion on the line shapes of single CdSe nanocrystallite quantum dots. *Journal of Physical Chemistry B*, 103:1826–1830, 3 1999.

[24] Lukas Fricke, Samuel J. Hile, Ludwik Kranz, Yousun Chung, Yu He, Prasanna Pakkiam, Matthew G. House, Joris G. Keizer, and Michelle Y. Simmons. Coherent control of a donor-molecule electron spin qubit in silicon. *Nature Communications*, 12, 12 2021.

[25] Kai-Mei C Fu. *Optical Manipulation of Electron Spins Bound to Neutral Donors in GaAs*. PhD thesis, Stanford University, 2007.

[26] Kai-Mei C. Fu, Susan M. Clark, Charles Santori, Colin R. Stanley, M. C. Holland, and Yoshihisa Yamamoto. Ultrafast control of donor-bound electron spins with single detuned optical pulses. *Nature Physics*, 4:780–784, 2008.

[27] Kai Mei C Fu, Charles Santori, Colin Stanley, M C Holland, and Yoshihisa Yamamoto. Coherent population trapping of electron spins in a high-purity n-type GaAs semiconductor. *Physical Review Letters*, 95:1–4, 2005.

[28] Kai Mei C. Fu, Wenzheng Yeo, Susan Clark, Charles Santori, Colin Stanley, M. C. Holland, and Yoshihisa Yamamoto. Millisecond spin-flip times of donor-bound electrons in GaAs. *Physical Review B*, 74, 2006.

[29] C. Gonzalez, D. Block, R. T. Cox, and A. Hervé. Magnetic resonance studies of shallow donors in zinc oxide. *Journal of Crystal Growth*, 59:357–362, 1982.

[30] Michael Gould, Srivatsa Chakravarthi, Ian R. Christen, Nicole Thomas, Shabnam Dadgostar, Yuncheng Song, Minjoo Larry Lee, Fariba Hatami, and Kai-Mei C. Fu. Large-scale gap-on-diamond integrated photonics platform for NV center-based quantum information. *Journal of the Optical Society of America B*, 33:B35, 3 2016.

[31] Michael Gould, Emma R. Schmidgall, Shabnam Dadgostar, Fariba Hatami, and Kai Mei C. Fu. Efficient extraction of zero-phonon-line photons from single nitrogen-vacancy centers in an integrated gap-on-diamond platform. *Physical Review Applied*, 6, 7 2016.

[32] H R Gray, R M Whitley, and C R Stroud. Coherent trapping of atomic populations. *Optics Letters*, 3:218–220, 1978.

[33] Kristiaan De Greve, Peter L. McMahon, David Press, Thaddeus D. Ladd, Dirk Bisping, Christian Schneider, Martin Kamp, Lukas Worschech, Sven Höfling, Alfred Forchel, and Yoshihisa Yamamoto. Ultrafast coherent control and suppressed nuclear feedback of a single quantum dot hole qubit. *Nature Physics*, 7:872–878, 11 2011.

[34] Stephen E. Harris. Electromagnetically induced transparency. *Physics Today*, 50:36–42, 1997.

[35] Y. He, S. K. Gorman, D. Keith, L. Kranz, J. G. Keizer, and M. Y. Simmons. A two-qubit gate between phosphorus donor electrons in silicon. *Nature*, 571:371–375, 7 2019.

[36] Martin Heiß, Eva Riedlberger, Danče Spirkoska, Max Bichler, Gerhard Abstreiter, and Anna Fontcuberta i. Morral. Growth mechanisms and optical properties of GaAs-based semiconductor microstructures by selective area epitaxy. *Journal of Crystal Growth*, 310:1049–1056, 2008.

[37] K. Hiramatsu, K. Nishiyama, A. Motogaito, H. Miyake, Y. Iyechika, and T. Maeda. Recent progress in selective area growth and epitaxial lateral overgrowth of III-nitrides: Effects of reactor pressure in MOVPE growth. *Physica Status Solidi (A)*, 176:535–543, 1999.

[38] M. Holmes, S. Kako, K. Choi, M. Arita, and Y. Arakawa. Spectral diffusion and its influence on the emission linewidths of site-controlled GaN nanowire quantum dots. *Physical Review B*, 92:115447–115454, 9 2015.

[39] Young Joon Hong, Sung Jin An, Hye Seong Jung, Chul Ho Lee, and Gyu Chul Yi. Position-controlled selective growth of ZnO nanorods on Si substrates using facet-controlled GaN micropatterns. *Advanced Materials*, 19:4416–4419, 12 2007.

[40] Peter C Humphreys, Norbert Kalb, Jaco P J Morits, Raymond N Schouten, F L Vermeulen, Daniel J Twitchen, Matthew Markham, and Ronald Hanson. Deterministic delivery of remote entanglement on a quantum network. *Nature*, 558:268–273, 2018.

[41] Keitaro Ikejiri, Takuya Sato, Hiroatsu Yoshida, Kenji Hiruma, Junichi Motohisa, Shinjiroh Hara, and Takashi Fukui. Growth characteristics of GaAs nanowires obtained by selective area metal-organic vapour-phase epitaxy. *Nanotechnology*, 19, 7 2008.

[42] Thorlabs Inc. Laser scanning microscopy tutorial, 2021.

[43] Anderson Janotti and Chris G. Van De Walle. Fundamentals of zinc oxide as a semiconductor. *Reports on Progress in Physics*, 72:126501, 2009.

[44] B E Kane. A silicon-based nuclear spin quantum computer. *Nature*, 393:133–137, 1998.

[45] Todd Karin. *Optical and Spin Properties of Defect-Bound Excitons in Semiconductors*. PhD thesis, University of Washington, 2016.

[46] Todd Karin, Russell J. Barbour, Charles Santori, Yoshihisa Yamamoto, Yoshiro Hirayama, and Kai-Mei C. Fu. Radiative properties of multicarrier bound excitons in GaAs. *Phys. Rev. B*, 91:165204, Apr 2015.

[47] H. J. Kimble. The quantum internet. *Nature*, 453:1023–1030, 6 2008.

[48] E Knill, R Laflamme, and G J Milburn. A scheme for efficient quantum computation with linear optics. *Nature*, 409:46–52, 2001.

[49] Miro Kroutvar, Yann Ducommun, Dominik Heiss, Max Bichler, Dieter Schuh, Gerhard Abstreiter, and Jonathan J. Finley. Optically programmable electron spin memory using semiconductor quantum dots. *Nature*, 432:81–84, 11 2004.

[50] E Senthil Kumar, I P Anderson, Z Deng, F Mohammadbeigi, T Wintschel, D Huang, and S P Watkins. Effect of group-III donors on high-resolution photoluminescence and morphology of ZnO nanowires grown by metalorganic vapour phase epitaxy. *Semicond. Sci. Technol*, 28:045014, 2013.

[51] E. Senthil Kumar, F. Mohammadbeigi, L. A. Boatner, and S. P. Watkins. High-resolution photoluminescence spectroscopy of Sn-doped ZnO single crystals. *Journal of Luminescence*, 176:47–51, 8 2016.

[52] T. D. Ladd, F. Jelezko, R. Laflamme, Y. Nakamura, C. Monroe, and J. L. O'Brien. Quantum computers. *Nature*, 464:45–53, 2010.

[53] Walter R. L. Lambrecht, Anna V. Rodina, Sukit Limpijumnong, B. Segall, and Bruno K. Meyer. Valence-band ordering and magneto-optic exciton fine structure in ZnO. *Phys. Rev. B*, 65:075207, Jan 2002.

[54] B. P. Lanyon, J. D. Whitfield, G. G. Gillett, M. E. Goggin, M. P. Almeida, I. Kassal, J. D. Biamonte, M. Mohseni, B. J. Powell, M. Barbieri, A. Aspuru-Guzik, and A. G. White. Towards quantum chemistry on a quantum computer. *Nature Chemistry*, 2:106–111, 2010.

[55] F. Lecocq, F. Quinlan, K. Cicak, J. Aumentado, S. A. Diddams, and J. D. Teufel. Control and readout of a superconducting qubit using a photonic link. *Nature*, 591:575–579, 3 2021.

[56] Sheng Kai Liao, Hai Lin Yong, Chang Liu, Guo Liang Shentu, Dong Dong Li, Jin Lin, Hui Dai, Shuang Qiang Zhao, Bo Li, Jian Yu Guan, Wei Chen, Yun Hong Gong, Yang Li, Ze Hong Lin, Ge Sheng Pan, Jason S. Pelc, M. M. Fejer, Wen Zhuo Zhang, Wei Yue Liu, Juan Yin, Ji Gang Ren, Xiang Bin Wang, Qiang Zhang, Cheng Zhi Peng, and Jian Wei Pan. Long-distance free-space quantum key distribution in daylight towards inter-satellite communication. *Nature Photonics*, 11:509–513, 8 2017.

[57] Jennifer F. Lilieholm, Vasileios Niaouris, Alexander Kato, Kai Mei C. Fu, and Boris B. Blinov. Photon-mediated entanglement scheme between a ZnO semiconductor defect and a trapped Yb ion. *Applied Physics Letters*, 117:154002, 10 2020.

[58] X. Linpeng, M.L.K. Viitaniemi, A. Vishnuradhan, Y. Kozuka, C. Johnson, M. Kawasaki, and K.-M.C. Fu. Coherence properties of shallow donor qubits in ZnO. *Physical Review Applied*, 10, 2018.

[59] Xiayu Linpeng. *Dopant Qubits in Direct Band Gap Materials*. PhD thesis, University of Washington, 2020.

[60] Xiayu Linpeng, Todd Karin, M V Durnev, Russell Barbour, M M Glazov, E Ya Sherman, S P Watkins, Satoru Seto, and Kai-Mei C Fu. Longitudinal spin relaxation of donor-bound electrons in direct band-gap semiconductors. *Physical Review B*, 94:125401–125420, 2016.

[61] Xiayu Linpeng, Todd Karin, Mikhail V. Durnev, Mikhail M. Glazov, Rüdiger Schott, Andreas D. Wieck, Arne Ludwig, and Kai Mei C. Fu. Optical spin control and coherence properties of acceptor bound holes in strained GaAs. *Physical Review B*, 103, 3 2021.

[62] Chien Liu, Zachary Dutton, Cyrus H. Behroozi, and Lene Vestergaard Hau. Observation of coherent optical information storage in an atomic medium using halted light pulses. *Nature*, 409:490–493, 2001.

[63] Evan MacQuarrie, Camille Chartrand, Daniel Higginbottom, Kevin Morse, Valentin Karasyuk, Sjoerd Roorda, and Stephanie Simmons. Generating T centres in photonic silicon-on-insulator material by ion implantation. *New Journal of Physics*, 23:103008, 9 2021.

[64] J. C. McCallum, B. C. Johnson, and T. Botzem. Donor-based qubits for quantum computing in silicon. *Applied Physics Reviews*, 8(3):031314, 2021.

[65] John Melngailis. Focused ion beam technology and applications. *Journal of Vacuum Science Technology B*, 5:469–495, 3 1987.

[66] X. Q. Meng, Haowei Peng, Y. Q. Gai, and Jingbo Li. Influence of ZnS and MgO shell on the photoluminescence properties of ZnO core/shell nanowires. *Journal of Physical Chemistry C*, 114:1467–1471, 2010.

[67] Bruno K. Meyer, H. Alves, D. M. Hofmann, W. Kriegseis, D. Forster, F. Bertram, J. Christen, A. Hoffmann, M. Straßburg, M. Dworzak, U. Haboeck, and A. V. Rodina. Bound exciton and donor-acceptor pair recombinations in ZnO. *Physica Status Solidi (B)*, 241:231–260, 2004.

[68] J. T. Muhonen, A. Laucht, S. Simmons, J. P. Dehollain, R. Kalra, F. E. Hudson, S. Freer, K. M. Itoh, D. N. Jamieson, J. C. McCallum, A. S. Dzurak, and A. Morello. Quantifying the quantum gate fidelity of single-atom spin qubits in silicon by randomized benchmarking. *Journal of Physics Condensed Matter*, 27, 4 2015.

[69] Vikram Khipple Mulligan, Hans Melo, Haley Irene Merritt, Stewart Slocum, Brian D. Weitzner, Andrew M. Watkins, P. Douglas Renfrew, Craig Pelissier, Paramjit S. Arora, and Richard Bonneau. Designing peptides on a quantum computer. *bioRxiv*, 2020.

[70] S. Muthukumar, H. Sheng, Z. Zhang, J. Zhong, N. W. Emanaetoglu, and Y. Lu. Selective growth of ZnO nanotips using MOCVD. *Proceedings of the IEEE Conference on Nanotechnology*, 2:21–24, 2002.

[71] Sung-Ho Na and Chul-Hong Park. First-principles study of the surface energy and atom cohesion of wurtzite ZnO and ZnS - Implications for nanostructure formation. *Journal of The Korean Physical Society*, 56, 01 2010.

[72] M. Nakano, A. Tsukazaki, R. Y. Gunji, K. Ueno, A. Ohtomo, T. Fukumura, and M. Kawasaki. Schottky contact on a ZnO (0001) single crystal with conducting polymer. *Applied Physics Letters*, 91:142113, 2007.

[73] Yunseong Nam, Jwo Sy Chen, Neal C. Pisenti, Kenneth Wright, Conor Delaney, Dmitri Maslov, Kenneth R. Brown, Stewart Allen, Jason M. Amini, Joel Apisdorf, Kristin M. Beck, Aleksey Blinov, Vandiver Chaplin, Mika Chmielewski, Coleman Collins, Shantanu Debnath, Kai M. Hudek, Andrew M. Ducore, Matthew Keesan, Sarah M. Kreikemeier, Jonathan Mizrahi, Phil Solomon, Mike Williams, Jaime David Wong-Campos, David Moehring, Christopher Monroe, and Jungsang Kim. Ground-state energy estimation of the water molecule on a trapped-ion quantum computer. *npj Quantum Information*, 6, 12 2020.

[74] Vasileios Niaouris, Mikhail V. Durnev, Xiayu Linpeng, Maria L. K. Viitaniemi, Christian Zimmermann, Aswin Vishnuradhan, Y. Kozuka, M. Kawasaki, and Kai-Mei C. Fu. Ensemble spin relaxation of shallow donor qubits in ZnO. *arXiv*, 11 2021.

[75] Michael A. Nielsen and Isaac L. Chuang. *Quantum Computation and Quantum Information*. Cambridge University Press, 2000.

[76] A Ohtomo, M Kawasaki, T Koida, K Masubuchi, H Koinuma, Y Sakurai, Y Yoshida, T Yasuda, and Y Segawa. $Zn_{1-x}Mg_xO$ as a II-VI widegap semiconductor alloy. *Applied Physics Letters*, 72:2466–2468, 1998.

[77] Won Il Park. Controlled synthesis and properties of ZnO nanostructures grown by metalorganic chemical vapor deposition: A review. *Metals and Materials International*, 14:659–665, 12 2008.

[78] Henrik Pedersen and Simon D. Elliott. Studying chemical vapor deposition processes with theoretical chemistry. *Theoretical Chemistry Accounts*, 133, 5 2014.

[79] D. F. Phillips, A. Fleischhauer, A. Mair, R. L. Walsworth, and M. D. Lukin. Storage of light in atomic vapor. *Physical Review Letters*, 86:783–786, 1 2001.

[80] J. M. Pino, J. M. Dreiling, C. Figgatt, J. P. Gaebler, S. A. Moses, M. S. Allman, C. H. Baldwin, M. Foss-Feig, D. Hayes, K. Mayer, C. Ryan-Anderson, and B. Neyenhuis. Demonstration of the trapped-ion quantum ccd computer architecture. *Nature*, 592:209–213, 4 2021.

[81] Alexander P.M. Place, Lila V.H. Rodgers, Pranav Mundada, Basil M. Smitham, Mattias Fitzpatrick, Zhaoqi Leng, Anjali Premkumar, Jacob Bryon, Andrei Vrajitoarea, Sara Sussman, Guangming Cheng, Trisha Madhavan, Harshvardhan K. Babla, Xuan Hoang Le, Youqi Gang, Berthold Jäck, András Gyenis, Nan Yao, Robert J. Cava, Nathalie P. de Leon, and Andrew A. Houck. New material platform for superconducting transmon qubits with coherence times exceeding 0.3 milliseconds. *Nature Communications*, 12:1779, 12 2021.

[82] M. Pompili, S. L. N. Hermans, S. Baier, H. K. C. Beukers, P. C. Humphreys, R. N. Schouten, R. F. L. Vermeulen, M. J. Tiggelman, L. dos Santos Martins, B. Dirkse, S. Wehner, and R. Hanson. Realization of a multinode quantum network of remote solid-state qubits. *Science*, 372(6539):259–264, 2021.

[83] Jonathan H. Prechtel, Andreas V. Kuhlmann, Julien Houel, Arne Ludwig, Sascha R. Valentin, Andreas D. Wieck, and Richard J. Warburton. Decoupling a hole spin qubit from the nuclear spins. *Nature Materials*, 15:981–986, 9 2016.

[84] David Press, Thaddeus D Ladd, Bingyang Zhang, and Yoshihisa Yamamoto. Complete quantum control of a single quantum dot spin using ultrafast optical pulses. supp mat. *Nature*, 456:218–21, 2008.

[85] A K Ramdas and S Rodriguez. Spectroscopy of the solid-state analogues of the hydrogen atom: donors and acceptors in semiconductors. *Reports on Progress in Physics*, 44:1297–1387, 1981.

[86] Markus Reiher, Nathan Wiebe, Krysta M. Svore, Dave Wecker, and Matthias Troyer. Elucidating reaction mechanisms on quantum computers. *Proceedings of the National Academy of Sciences*, 114:7555–7560, 7 2017.

[87] M. E. Reimer, G. Bulgarini, A. Fognini, R. W. Heeres, B. J. Witek, M. A.M. Versteegh, A. Rubino, T. Braun, M. Kamp, S. Höfling, D. Dalacu, J. Lapointe, P. J. Poole, and V. Zwiller. Overcoming power broadening of the quantum dot emission in a pure wurtzite nanowire. *Physical Review B*, 93:195316, 5 2016.

[88] D. C. Reynolds, C. W. Litton, and T. C. Collins. Zeeman effects in the edge emission and absorption of ZnO. *Physical Review*, 140:1726–1734, 11 1965.

[89] J. P. Richters, T. Voss, D. S. Kim, R. Scholz, and M. Zacharias. Enhanced surface-excitonic emission in ZnO/Al_2O_3 core-shell nanowires. *Nanotechnology*, 19, 7 2008.

[90] Steffen Rüttinger. *Confocal Microscopy and Quantitative Single Molecule Techniques for Metrology in Molecular Medicine*. PhD thesis, Technical University Berlin, 2006.

[91] Kamyar Saeedi, Stephanie Simmons, Jeff Z Salvail, Phillip Dluhy, Helge Riemann, Nikolai V Abrosimov, Peter Becker, Hans-Joachim Pohl, John J L Morton, and Mike L W Thewalt. Room-temperature quantum bit storage exceeding 39 minutes using ionized donors in silicon-28. *Science*, 342:830–833, 2013.

[92] C. Santori, P. E. Barclay, K. M.C. Fu, R. G. Beausoleil, S. Spillane, and M. Fisch. Nanophotonics for quantum optics using nitrogen-vacancy centers in diamond. *Nanotechnology*, 21, 2010.

[93] Charles Santori, Philippe Tamarat, Philipp Neumann, Jörg Wrachtrup, David Fattal, Raymond G. Beausoleil, James Rabeau, Paolo Olivero, Andrew D. Greentree, Steven Prawer, Fedor Jelezko, and Philip Hemmer. Coherent population trapping of single spins in diamond under optical excitation. *Physical Review Letters*, 97:247401–247405, 2006.

[94] Emma R. Schmidgall, Srivatsa Chakravarthi, Michael Gould, Ian R. Christen, Karine Hestroffer, Fariba Hatami, and Kai Mei C. Fu. Frequency control of single quantum emitters in integrated photonic circuits. *Nano Letters*, 18:1175–1179, 2 2018.

[95] Tim Schröder, Sara L. Mouradian, Jiabao Zheng, Matthew E. Trusheim, Michael Walsh, Edward H. Chen, Luozhou Li, Igal Bayn, and Dirk Englund. Quantum nanophotonics in diamond [invited]. *Journal of the Optical Society of America B*, 33:B65, 4 2016.

[96] T. Senger and K. Bajaj. Optical properties of confined polaronic excitons in spherical ionic quantum dots. *Physical Review B*, 68:045313–045324, 7 2003.

[97] Peter W Shor. Algorithms for quantum computation: Discrete logarithms and factoring. pages 124–134, 1994.

[98] Peter W Shor and John Preskill. Simple proof of security of the BB84 quantum key distribution protocol. *Physical Review Letters*, 85:441–444, 2000.

[99] Darin J. Sleiter, Kaoru Sanaka, Y. M. Kim, Klaus Lischka, Alexander Pawlis, and Yoshihisa Yamamoto. Optical pumping of a single electron spin bound to a fluorine donor in a ZnSe nanostructure. *Nano Letters*, 13:116–120, 1 2013.

[100] Gerald B. Stringfellow. *Organometallic vapor phase epitaxy: theory and practice*. Academic Press, 1989.

[101] S. C. Su, Y. M. Lu, Z. Z. Zhang, C. X. Shan, B. H. Li, D. Z. Shen, B. Yao, J. Y. Zhang, D. X. Zhao, and X. W. Fan. Valence band offset of $ZnO/Zn_{0.85}Mg_{0.15}O$ heterojunction measured by x-ray photoelectron spectroscopy. *Applied Physics Letters*, 93:082108, 2008.

[102] Robert K Swank. Surface properties of II-VI compounds. *Physics Review*, 153:844–849, 1967.

[103] B.M. Terhal. Quantum supremacy, here we come., 6 2018.

[104] Robin Thierry. *ZnO nanowire growth and heterostructures core-shell ZnO / ZnMgO MOVPE*. PhD thesis, Universite Grenoble Alpes, 2011.

[105] Guilherme Tosi, Fahd A. Mohiyaddin, Vivien Schmitt, Stefanie Tenberg, Rajib Rahman, Gerhard Klimeck, and Andrea Morello. Silicon quantum processor with robust long-distance qubit couplings. *Nature Communications*, 8, 12 2017.

[106] V.V. Travnikov, A. Freiberg, and S.F. Savikhin. Surface excitons in ZnO crystals. *Journal of Luminescence*, 47:107–112, 1990.

[107] Alexei M. Tyryshkin, Shinichi Tojo, John J.L. Morton, Helge Riemann, Nikolai V. Abrosimov, Peter Becker, Hans Joachim Pohl, Thomas Schenkel, Michael L.W. Thewalt, Kohei M. Itoh, and S. A. Lyon. Electron spin coherence exceeding seconds in high-purity silicon. *Nature Materials*, 11:143–147, 2012.

[108] Maria L. K. Viitaniemi, Christian Zimmermann, Vasileios Niaouris, Samuel H. D'Ambrosia, Xingyi Wang, E. Senthil Kumar, Faezeh Mohammadbeigi, Simon P. Watkins, and Kai-Mei C. Fu. Coherent spin preparation of indium donor qubits in single ZnO nanowires. *arXiv.org*, 2021.

[109] Maria L. K. Viitaniemi, Christian Zimmermann, Vasilis Niaouris, E Senthil Kumar, Simon Watkins, and Kai-Mei C Fu. Optical pumping of few shallow donor qubits in ZnO nanostructures. page FTh1P.5. Conference on Lasers and Electro-Optics, 2021.

[110] M. R. Wagner, G. Callsen, J. S. Reparaz, J. H. Schulze, R. Kirste, M. Cobet, I. A. Ostapenko, S. Rodt, C. Nenstiel, M. Kaiser, A. Hoffmann, A. V. Rodina, M. R. Phillips, S. Lautenschläger, S. Eisermann, and B. K. Meyer. Bound excitons in ZnO: Structural defect complexes versus shallow impurity centers. *Physical Review B*, 84:035313–035331, 2011.

[111] Markus R. Wagner, Jan Hindrik Schulze, Ronny Kirste, Munise Cobet, Axel Hoffmann, Christian Rauch, Anna V. Rodina, Bruno K. Meyer, Uwe Röder, and Klaus Thonke. Γ_7 valence band symmetry related hole fine splitting of bound excitons in ZnO observed in magneto-optical studies. *Physical Review B*, 80:205203–205209, 2009.

[112] G. Waldherr, Y. Wang, S. Zaiser, M. Jamali, T. Schulte-Herbrüggen, H. Abe, T. Ohshima, J. Isoya, J. F. Du, P. Neumann, and J. Wrachtrup. Quantum error correction in a solid-state hybrid spin register. *Nature*, 506:204–207, 2014.

[113] Pengfei Wang, Chun Yang Luan, Mu Qiao, Mark Um, Junhua Zhang, Ye Wang, Xiao Yuan, Mile Gu, Jingning Zhang, and Kihwan Kim. Single ion qubit with estimated coherence time exceeding one hour. *Nature Communications*, 12:233, 12 2021.

[114] Thomas F Watson, Bent Weber, Yu-Ling Hsueh, Lloyd C L Hollenberg, Rajib Rahman, and Michelle Y Simmons. Atomically engineered electron spin lifetimes of 30 s in silicon. *Science Advances*, 3, 2017.

[115] M. Willander, O. Nur, Q. X. Zhao, L. L. Yang, M. Lorenz, B. Q. Cao, J. Ziga Pérez, C. Czekalla, G. Zimmermann, M. Grundmann, A. Bakin, A. Behrends, M. Al-Suleiman, A. El-Shaer, A. Che Mofor, B. Postels, A. Waag, N. Boukos, A. Travlos, H. S. Kwack, J. Guinard, and D. Le Si Dang. Zinc oxide nanorod based photonic devices: Recent progress in growth, light emitting diodes and lasers. *Nanotechnology*, 20:332001, 8 2009.

[116] Kirt R. Williams, Kishan Gupta, and Matthew Wasilik. Etch rates for micromachining processing - part II. *Journal of Microelectromechanical Systems*, 12:761–778, 12 2003.

[117] L. Wischmeier, T. Voss, S. Börner, and W. Schade. Comparison of the optical properties of as-grown ensembles and single ZnO nanowires. *Applied Physics A*, 84:111–116, 2006.

[118] David E. Wolf. What is the confocal volume?, 2008.

[119] Yulin Wu, Wan-Su Bao, Sirui Cao, Fusheng Chen, Ming-Cheng Chen, Xiawei Chen, Tung-Hsun Chung, Hui Deng, Yajie Du, Daojin Fan, Ming Gong, Cheng Guo, Chu Guo, Shaojun Guo, Lianchen Han, Linyin Hong, He-Liang Huang, Yong-Heng Huo, Liping Li, Na Li, Shaowei Li, Yuan Li, Futian Liang, Chun Lin, Jin Lin, Haoran Qian, Dan Qiao, Hao Rong, Hong Su, Lihua Sun, Liangyuan Wang, Shiyu Wang, Dachao Wu, Yu Xu, Kai Yan, Weifeng Yang, Yang Yang, Yangsen Ye, Jianghan Yin, Chong Ying, Jiale Yu, Chen Zha, Cha Zhang, Haibin Zhang, Kaili Zhang, Yiming Zhang, Han Zhao, Youwei Zhao, Liang Zhou, Qingling Zhu, Chao-Yang Lu, Cheng-Zhi Peng, Xiaobo Zhu, and Jian-Wei Pan. Strong quantum computational advantage using a superconducting quantum processor. *Physical Review Letters*, 127:80501–80508, 6 2021.

[120] Xiaodong Xu, Bo Sun, Paul R. Berman, Duncan G. Steel, Allan S. Bracker, Dan Gammon, and L. J. Sham. Coherent population trapping of an electron spin in a single negatively charged quantum dot. *Nature Physics*, 4:692–695, 2008.

[121] Leo Yu, Chandra M. Natarajan, Tomoyuki Horikiri, Carsten Langrock, Jason S. Pelc, Michael G. Tanner, Eisuke Abe, Sebastian Maier, Christian Schneider, Sven Höfling, Martin Kamp, Robert H. Hadfield, Martin M. Fejer, and Yoshihisa Yamamoto. Two-photon interference at telecom wavelengths for time-bin-encoded single photons from quantum-dot spin qubits. *Nature Communications*, 6, 11 2015.

[122] Gang Zhang, Yuan Cheng, Jyh-Pin Chou, and Adam Gali. Material platforms for defect qubits and single-photon emitters. *Applied Physics Reviews*, 7(3):031308, 2020.

[123] H. H. Zhang, X. H. Pan, B. Lu, J. Y. Huang, P. Ding, W. Chen, H. P. He, J. G. Lu, S. S. Chen, and Z. Z. Ye. Mg composition dependent band offsets of $Zn_{1-x}Mg_xO$/ZnO heterojunctions. *Physical Chemistry Chemical Physics*, 15:11231–11235, 2013.

[124] Han-Sen Zhong, Hui Wang, Yu-Hao Deng, Ming-Cheng Chen, Li-Chao Peng, Yi-Han Luo, Jian Qin, Dian Wu, Xing Ding, Yi Hu, Peng Hu, Xiao-Yan Yang, Wei-Jun Zhang, Hao Li, Yuxuan Li, Xiao Jiang, Lin Gan, Guangwen Yang, Lixing You, Zhen Wang, Li Li, Nai-Le Liu, Chao-Yang Lu, and Jian-Wei Pan. Quantum computational advantage using photons. *Science*, 370:1460–1463, 2020.

Appendix A

DERIVATION OF POLARIZATION RULES

The goal of this section is to derive the optical polarization selection rules for the D^0-D^0X system in ZnO. The optical transitions occur between the ground electron states $|\uparrow\rangle / |\downarrow\rangle$ and excited states $|\Uparrow\uparrow\downarrow\rangle / |\Downarrow\uparrow\downarrow\rangle$. For simplicity, the excited states are described solely by the hole state $|\Uparrow\rangle / |\Downarrow\rangle$, because the electrons form a spin singlet. The intensity of the optical transition between electron state $|i\rangle$ and hole state $|j\rangle$ is proportional to $|\epsilon \cdot \boldsymbol{p}_{ij}|^2$ [46], where ϵ is the electric field vector and $\boldsymbol{p}_{ij} = \langle j| \boldsymbol{\mu} |i\rangle$. $\boldsymbol{\mu}$ is the dipole operator and is equal to $e\boldsymbol{r}$, where e is the electron charge and $\boldsymbol{r} = x\boldsymbol{x} + y\boldsymbol{y} + z\boldsymbol{z}$ (position operator).

To find the polarization rules, we begin with the electron and hole wavefunctions at B = 0 T [53].

$$\begin{cases} |\uparrow\rangle_{B=0} = |S, \uparrow_z\rangle \\ |\downarrow\rangle_{B=0} = i\,|S, \downarrow_z\rangle \end{cases} \tag{A.1}$$

$$\begin{cases} |\Downarrow\rangle_{B=0} = ia\,|\frac{X+iY}{\sqrt{2}}, \downarrow_z\rangle - ib\,|Z, \uparrow_z\rangle \\ |\Uparrow\rangle_{B=0} = a\,|\frac{X-iY}{\sqrt{2}}, \uparrow_z\rangle + b\,|Z, \downarrow_z\rangle \end{cases} \tag{A.2}$$

$|S\rangle, |\frac{X+iY}{\sqrt{2}}\rangle$, and $|Z\rangle$ are the orbital basis functions. $\boldsymbol{z}$ is parallel to the crystal c-axis. The hole is defined as opposite of the unoccupied electron angular momentum in the valence band. a and b are constants determined from first-principles calculations to be 0.9950 and -0.0999, respectively [53].

At magnetic field, we must consider the addition of the Zeeman term

$$H_{\text{Zeeman},i} = \frac{1}{2} g_i \mu_B \boldsymbol{\sigma} \cdot \boldsymbol{B}, \tag{A.3}$$

where i is either electron or hole, g_i is the corresponding g-factor, μ_B is the Bohr magneton, $\boldsymbol{\sigma}$ are the Pauli spin matrices, and $\boldsymbol{B}$ is the magnetic field vector. We will now consider our two magnetic field geometries separately. We will solve for all of the possible transitions; see Sect. 3.6 for experimental considerations.

A.1 Voigt Geometry, $B \perp \hat{c}$

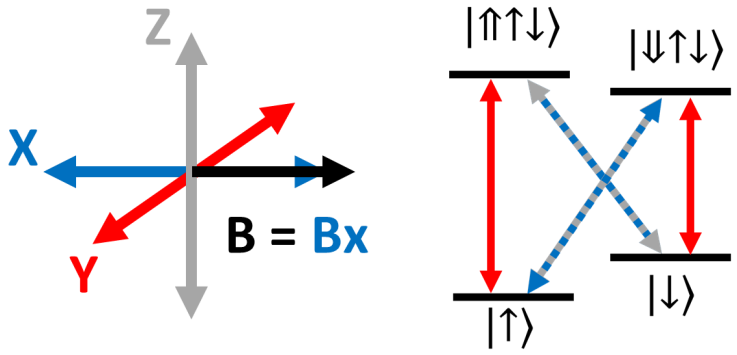

Figure A.1: Selection rules for $B \parallel \hat{x}$. The left side shows the Cartesian coordinate system with magnetic field direction shown. $\hat{z}$ is parallel to the crystal c-axis. The colors in the right side, correspond to the direction that light is polarized (i.e. red transitions are light polarized in the $\hat{y}$ direction). The dashed lines indicate elliptically polarized light in the $\hat{x} - \hat{z}$ direction.

For the case where the magnetic field is parallel to the x-axis ($B \parallel \hat{x}$), the Zeeman Hamiltonian is

$$H_{\text{Zeeman},i,B\parallel\hat{x}} = \begin{pmatrix} 0 & \frac{1}{2}g_i\mu_B B \\ \frac{1}{2}g_i\mu_B B & 0 \end{pmatrix}. \tag{A.4}$$

Solving this system we get the new electron and hole eigenstates

$$\begin{cases} |\uparrow\rangle_{B=0} = \frac{1}{\sqrt{2}}|S,\uparrow_z\rangle + \frac{i}{\sqrt{2}}|S,\downarrow_z\rangle \\ |\downarrow\rangle_{B=0} = -\frac{1}{\sqrt{2}}|S,\uparrow_z\rangle + \frac{i}{\sqrt{2}}|S,\downarrow_z\rangle \end{cases} \tag{A.5}$$

$$\begin{cases} |\Downarrow\rangle_{B>0} = -\frac{1}{\sqrt{2}}(a\,|\frac{X-iY}{\sqrt{2}},\uparrow_z\rangle + b\,|Z,\downarrow_z\rangle) + \frac{1}{\sqrt{2}}(ia\,|\frac{X+iY}{\sqrt{2}},\downarrow_z\rangle - ib\,|Z,\uparrow_z\rangle) \\ |\Uparrow\rangle_{B>0} = \frac{1}{\sqrt{2}}(a\,|\frac{X-iY}{\sqrt{2}},\uparrow_z\rangle + b\,|Z,\downarrow_z\rangle) + \frac{1}{\sqrt{2}}(ia\,|\frac{X+iY}{\sqrt{2}},\downarrow_z\rangle - ib\,|Z,\uparrow_z\rangle) \end{cases} \tag{A.6}$$

The dipole matrix elements, $\boldsymbol{p}$, are thus

$$\begin{cases} \langle\Uparrow|\,\boldsymbol{\mu}\,|\uparrow\rangle = \mu_0 \cdot \frac{-ia}{\sqrt{2}}\hat{y} \\ \langle\Uparrow|\,\boldsymbol{\mu}\,|\downarrow\rangle = \mu_0 \cdot (\frac{a}{\sqrt{2}}\hat{x} - ib\hat{z}) \\ \langle\Downarrow|\,\boldsymbol{\mu}\,|\uparrow\rangle = \mu_0 \cdot (\frac{-a}{\sqrt{2}}\hat{x} - ib\hat{z}) \\ \langle\Downarrow|\,\boldsymbol{\mu}\,|\downarrow\rangle = \mu_0 \cdot \frac{ia}{\sqrt{2}}\hat{y} \end{cases} \tag{A.7}$$

where $\mu_0 = \langle S|\, e\cdot x\,|X\rangle = \langle S|\, e\cdot y\,|Y\rangle = \langle S|\, e\cdot z\,|Z\rangle$. The spin combination rules, $\langle\uparrow|\downarrow\rangle = \langle\downarrow|\uparrow\rangle = 0$ and $\langle\uparrow|\uparrow\rangle = \langle\downarrow|\downarrow\rangle = 1$, have been used. Using the notation that the transition $|\Uparrow\uparrow\downarrow\rangle \Leftrightarrow |\uparrow\rangle$ corresponds to $\langle\Uparrow|\boldsymbol{\mu}|\downarrow\rangle$ we get the selection rules as shown in Fig. A.1.

A.2 Faraday Geometry, $B \parallel \hat{c}$

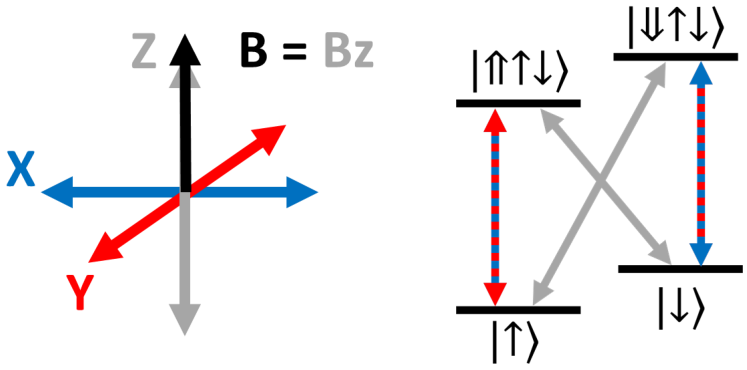

Figure A.2: Selection rules for $B \parallel \hat{z}$. The left side shows the Cartesian coordinate system with magnetic field direction shown. $\hat{z}$ is parallel to the crystal c-axis. The colors in the right side, correspond to the direction that light is polarized (i.e. gray transitions are light polarized in the $\hat{z}$ direction). The dashed lines indicate circularly polarized light in the $\hat{x}-\hat{y}$ direction.

For the case where the magnetic field is parallel to the z-axis ($B \parallel \hat{z}$), the Zeeman Hamiltonian is

$$H_{\text{Zeeman},i,B\parallel\hat{x}} = \begin{pmatrix} \frac{1}{2}g_i\mu_B B & 0 \\ 0 & \frac{-1}{2}g_i\mu_B B \end{pmatrix}. \tag{A.8}$$

Therefore the electron and hole eigenstates do not change at magnetic field. The dipole matrix elements, $\boldsymbol{p}$, are thus

$$\begin{cases} \langle\Uparrow|\boldsymbol{\mu}|\uparrow\rangle = \mu_0\cdot(\frac{a}{\sqrt{2}}\hat{x} - \frac{ia}{\sqrt{2}}\hat{y}) \\ \langle\Uparrow|\boldsymbol{\mu}|\downarrow\rangle = \mu_0\cdot(ib\hat{z}) \\ \langle\Downarrow|\boldsymbol{\mu}|\uparrow\rangle = \mu_0\cdot(-ib\hat{z}) \\ \langle\Downarrow|\boldsymbol{\mu}|\downarrow\rangle = \mu_0\cdot(\frac{-a}{\sqrt{2}}\hat{x} - \frac{ia}{\sqrt{2}}\hat{y}) \end{cases} \tag{A.9}$$

and we get the selection rules as shown in Fig. A.2.

Appendix B

OSCILLATORY BACKGROUND CORRECTION

A wavelength-dependent modulation of the signal is observed in single nanowire photoluminescence excitation (PLE) data. This is a consequence of a wavelength dependence of the transmittance and reflectance of the beamsplitter used in the excitation path. During the single nanowire measurements, the laser power was held constant at P_{C} (Fig. B.1b), leading to an oscillation in the excitation power, P_{A}. In order to correct for this oscillation in the excitation power, the wavelength dependence of the ratio of the reflected to transmitted power for the beamsplitter was measured. Fig. B.1a shows a representative measurement. The wavelength dependence of $P_{\mathrm{A}}/P_{\mathrm{B}}$ was found to have minimal variation in offset, amplitude, and period, while the phase was found to change significantly between measurements, possibly depending on factors such as ambient temperature.

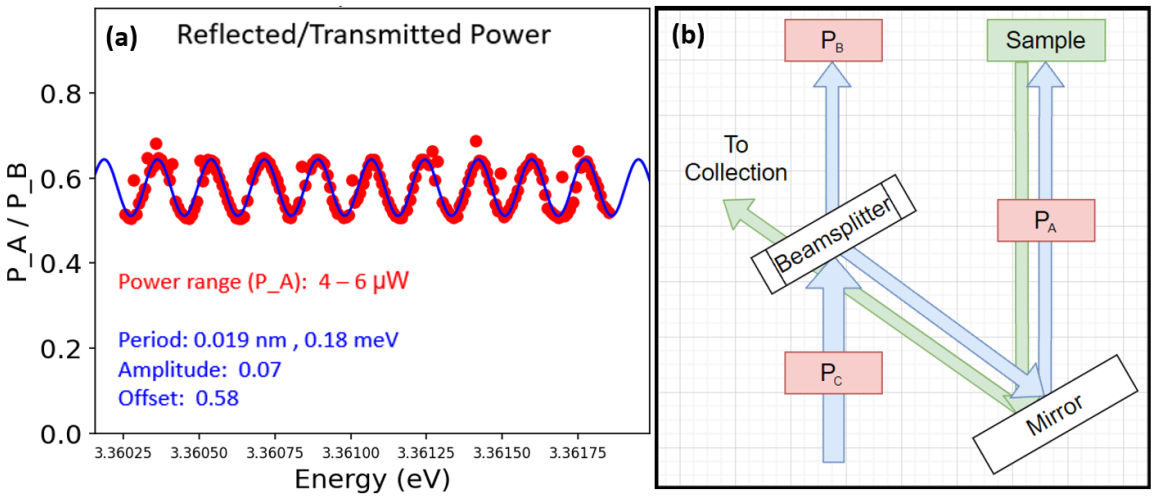

Figure B.1: (a) A measurement of wavelength dependence of excitation path beamsplitter transmitted and reflected powers. (b) Schematic of excitation path with power meter positions.

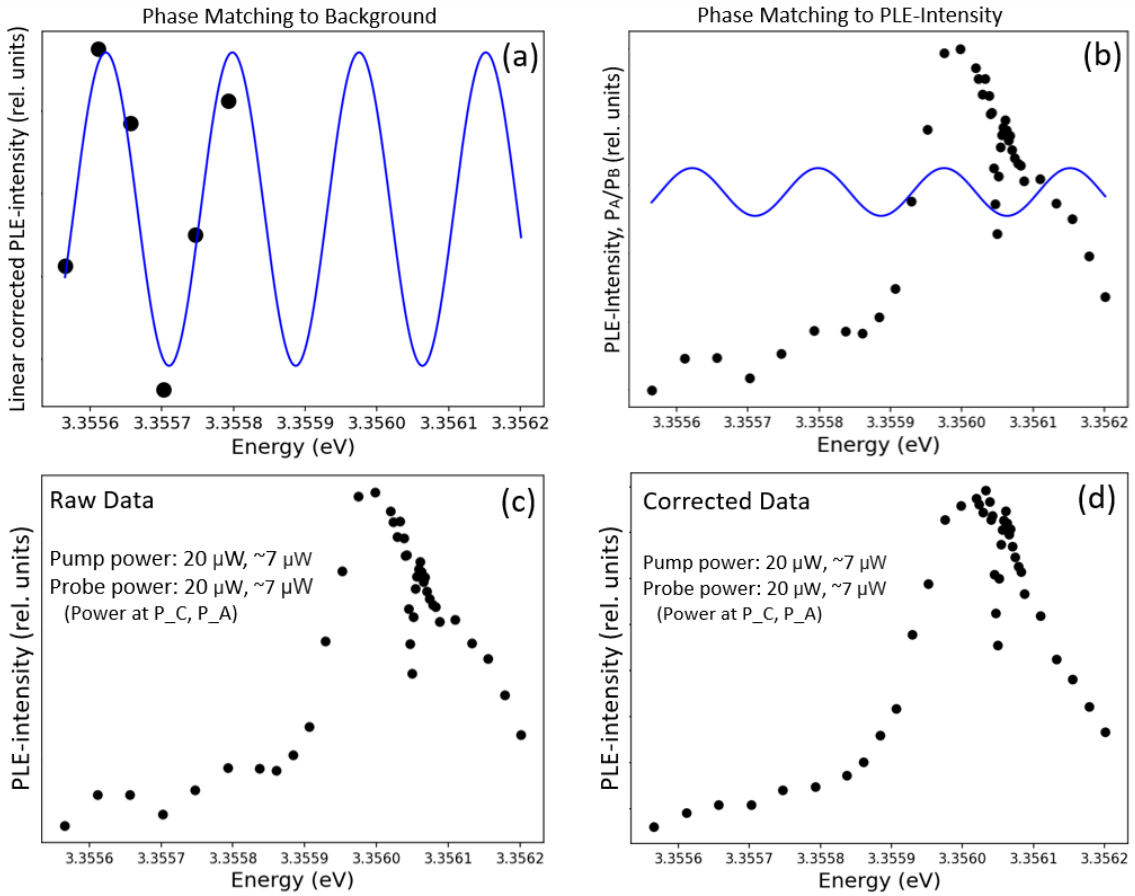

Figure B.2: (a) Sine fit with fixed period for determination of oscillation phase from linear corrected background PLE intensity. (b) Comparison of the phase and period of $P_{\mathrm{A}}/P_{\mathrm{B}}$ with low-energy background of the PLE intensity. Two oscillations in the background can be seen to the left of the peak, matching the phase and period of the correction, shown in blue. (c,d) Example data from the measurement of CPT on the In $\mathrm{D}^0\mathrm{X}$ in a single nanowire (c) before and (d) after correction.

Correction of this oscillation was only applied to single-nanowire data where power was measured at P_{C} rather than P_{A}. Assuming minimal absorption and scattering from the beamsplitter, and only phase changes in $P_{\mathrm{A}}/P_{\mathrm{B}}$, oscillations in the excitation power can be calculated. For simplicity, we will use $f(\mathrm{E},\, \phi)$ for handling $P_{\mathrm{A}}/P_{\mathrm{B}}$, using the data in Fig. B.1 to define the function. E is the excitation photon energy, and ϕ is the phase of the oscillation.

$$f(E,\phi) = \frac{\mathrm{P_A}}{\mathrm{P_B}} = 0.58 + 0.07 \times \sin\left(\frac{2\pi E}{0.18\mathrm{meV}} + \phi\right)$$

Minimal absorption and scattering tells us $\mathrm{P_C} = \mathrm{P_A} + \mathrm{P_B}$, thus $\mathrm{P_C} = \mathrm{P_A}\ (1 + 1/f(\mathrm{E},\ \phi))$. The mean power reflected over incident power $\mathrm{P_A/P_C}$ is 0.36. This factor can be used to convert from an oscillating excitation power to a constant excitation power, as $\mathrm{P_C}$ was held constant during measurement. The oscillatory background correction is performed by determining the phase of $f(\mathrm{E},\, \phi)$, then multiplying the measured PLE intensity by the resulting energy dependent correction factor.

$$\frac{\text{Corrected } \mathrm{P_A}}{\mathrm{P_A}} = (1 + \frac{1}{f(E,\phi)}) \cdot (0.36) = \text{Correction Factor}$$

In the regime where the PLE intensity is proportional to the probe power, PLE data can be accurately corrected using this factor. The probe power changes by 18% peak to peak. This small variation in excitation power from the oscillation allows for the approximation of the dependence of the PLE intensity on probe power as linear, $\mathrm{Counts}(E) \approx \alpha P_{\mathrm{A}}(E) + \beta$. For single-laser PLE and for two-laser PLE with observable oscillations in the off-resonant signal, we find that $\alpha >> \beta$ and have therefore corrected the oscillations. Two-laser PLE with no observable oscillations were assumed to have $\alpha << \beta$ and have not been corrected.

This correction is applied in Fig. B.2. First the off-resonant or background region is differentiated from the on-resonant or peak region. The background region is then linearly corrected and fit using a sine function with a period of 0.18 meV (Fig. B.2a). From this fit the phase of $P_{\mathrm{A}}/P_{\mathrm{B}}$ is obtained, so our correction factor is determined. The resulting $P_{\mathrm{A}}/P_{\mathrm{B}}$ can be compared to PLE intensity to check that the oscillations align well with the low energy portion of the data, which was considered part of the background (Fig. B.2b).

Only the period and phase of $P_{\mathrm{A}}/P_{\mathrm{B}}$ is checked at this stage. Using the determined $P_{\mathrm{A}}/P_{\mathrm{B}}$, the PLE intensity is multiplied by the correction factor. The effect of this correction can be seen in Fig. B.2c and Fig. B.2d.

Appendix C

SUBSTRATE ETCHING DETAILS

Planning

The etch rates were seen to vary between runs. This may be the result of using slightly different etchants (diluted HF vs BOE) or differences in the deposition of the mask material. It is encouraged to perform an etch test when either of these variables is changed.

Cleaving Sapphire

Samples need to be at least 8 mm wide (see PMMA). Scribe hard all the way across the back of where you want to cleave. Place the piece upside down on a glass slide so that the scratch is aligned with the edge of the slide. Press (i.e. with tweezers) on both edges of the sapphire until it snaps. It does not often snap along the desired line.

Deposit SiO_2/SiN_x

The PECVD2 in the UW clean room was used along with the recipe SiO_350_LDR. For SiO_2, the P1 recipe is better than the LDR recipe. For SiN_x, the LDR recipe is fine.

PMMA

Samples need to be at least 8 mm wide for the PMMA to spin coat evenly. Use A4, 950 PMMA. Spin coat with 0.8 kRPM for 9 s followed by 4 kPRM for 60 s. Heat at 180°C for 5 min. PMMA is UV sensitive, so if you plan to store it for a bit, put it somewhere dark.

Gold

Take note of approximately where the PMMA becomes uniform (see e-beam). Sputter 2 nm gold so that it is conductive (for e-beam/SEM). For suppering using 20 Amp, 0.8 units of Ar pressure, 50 sec.

E-beam/SEM

After covering in gold, put 4 scratches from about the center of each edge. Extend the scratch to where the PMMA became uniform. Also put an "x" in the top right corner. In the e-beam, find every corner and edge of scratch. Record the location and use the ends of the scratches for z-leveling. Write the pattern. Between each chip you need to turn off the High Voltage (HV) for 5 min and log off. Then you can log back in and recalibrate the machine to write the next chip. Reasonable settings are: HV = 30 kV, Beam Intensity = 6 (out of 10). I usually do 3 different dose regions (300, 600, 900 $\mu C/cm^2$). The higher doses are probably unnecessary. The beam current is set by the machine and measured. It is usually around 30-40 pA. Develop in cold IPA:water (7:3) for ∼1 min. Then rinse in warm IPA for 10 s. Use N_2 gas to dry. Do *not* use gold etchant (I_2 and KI). Check that the write came out using the optical microscope.

AFM

AFM to measure the width of the holes. When you save, the processed data (not the raw data) is saved. For faster response, increase PI (in PID). If you see an oscillation, decrease PI. Note that changing the rotation, changes the scan direction. If you are going to use Gwyddion to analyze the data, write down: scan range, scan rate, line number, rotation, PID, and any analysis done on the pictures. NanoscopeAnalysis automatically reports all of these things.

Etch

Use BOE to etch the SiO_2/SiN_x. Careful with the etch rate. Use acetone to remove the PMMA by soaking and agitating for ∼1 min. Then rinse in IPA for ∼10 s. Use N_2 gas to dry. Repeat the acetone clean, but with a sonication for 5 min.

Appendix D

ADDITIONAL GROWTH IMAGES

This section contains additional images of selective area growth attempts.

- Fig. D.1 contains additional images from the growths used to test the growth rate in Sect. 5.3.3.
- Fig. D.2 contains additional images from the growths done on the SiO_2 patterned substrates in Sect. 5.3.3.
- Fig. D.3 contains information about an additional growth as well as additional images from the growths done on the SiN_x patterned substrates in Sect. 5.3.3.

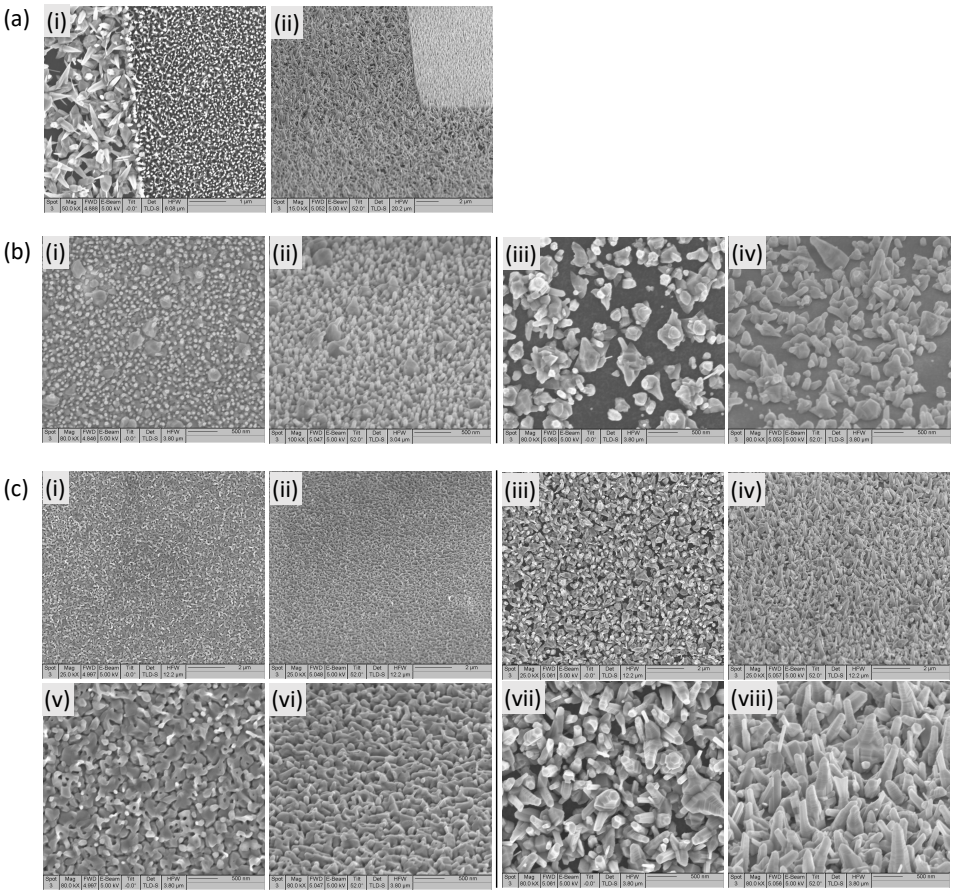

Figure D.1: All growths are performed at 605°C with a N_2O flow rate of 1.3×10^{-1} mol/min. Before all growths, a 20 min pre-anneal is performed at 605°C under N_2O. After all growths, a 2 min post-anneal is performed at 605°C under N_2O. (a) Sample H1070 - 15 min growth with a standard DMZn flow rate of 2.24×10^{-5} mol/min. In (i, ii), a large marker of exposed sapphire is visible on the right. (b) Sample H1073 - 15 min growth with a reduced DMZn flow rate of 7.47×10^{-6} mol/min. (i, ii) are on sapphire while (iii, iv) are on SiO_2. (c) Sample H1074 - 45 min growth with a reduced DMZn flow rate of 7.47×10^{-6} mol/min. (i, ii, v, vi) are on sapphire while (iii, iv, vii, viii) are on SiO_2.

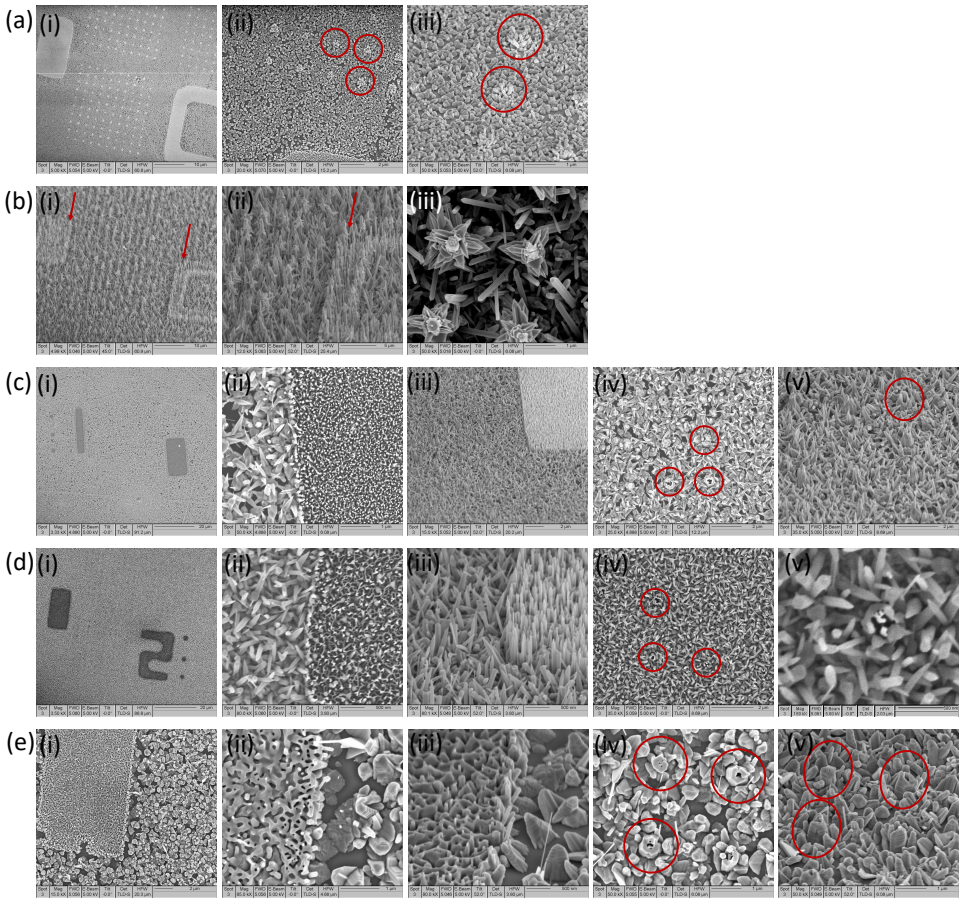

Figure D.2: SEM images of several growth attempts. The magnification, scale, and tilt are indicated on the bottom of each image. The positions of some holes are indicated with red circles. The edges of some large markers are indicated with red arrows. All of the samples are on a patterned SiO_2 substrate. The growths all occur with a DMZn flow rate of 2.24×10^{-5} mol/min and a N_2O flow rate of 1.3×10^{-1} mol/min. Each growth is followed by a 2 min post-anneal under N_2O at the growth temperature. Each row of the figure includes images from different locations or angles of the same sample. (a) Sample H1067 - Anneal at 605°C under N_2O for 20 min. A brief growth occurs at 680°C. Anneal again at 605°C under N_2O for 20 min. Start a new growth at 605°C for 10min. (b) Sample H1068 - Anneal at 605°C under N_2O for 5 min. Growth at 605°C for 60 min. (c) Sample H1070 - Anneal at 605°C under N_2O for 20 min. Growth at 605°C for 15 min. (d) Sample H1071 - Anneal at 905°C under O_2 for 20 min. Growth at 605°C for 15 min. (e) Sample H1073 - Anneal at 905°C under O_2 for 20 min. Growth at 705°C for 15 min.

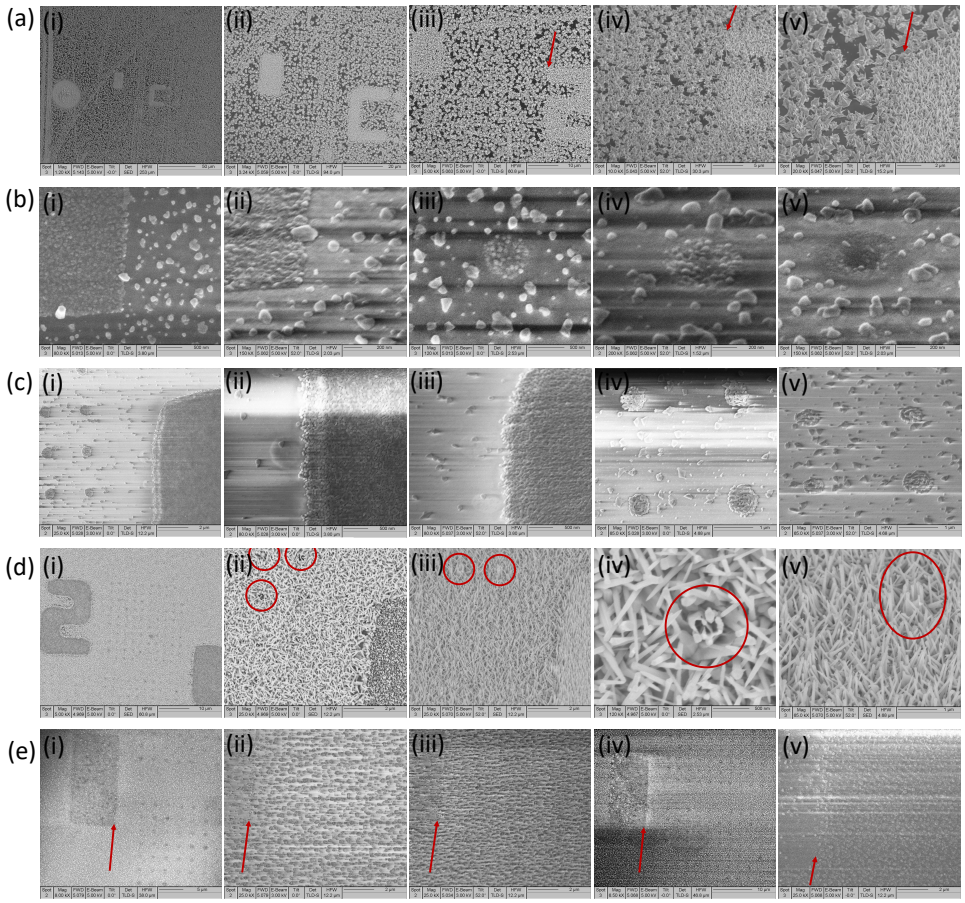

Figure D.3: All samples use the patterned SiN_x substrate. All growths with a standard N_2O flow rate of 1.3^{-1} mol/min. (a) Sample H1069 - Pre-anneal at 605°C under N_2 for 10 min. 15 min growth at 605°C with a standard 2.24^{-5} mol/min DMZn flow rate. No post-anneal. The arrow indicates the top left corner of a large "2" marker. (b) Sample H1080 - Pre-anneal at 905°C under N_2O for 20 min. 15 min growth at 905°C with a reduced 7.47^{-6} mol/min DMZn flow rate. Post-anneal at 905°C under N_2O for 2 min. (c) Growth 17 - Pre-anneal at 905°C under N_2O for 20 min. Growth at 905°C for 1m40s + 705°C for 1m40s at 7.47^{-6} mol/min (slow). Post-anneal at 705°C under N_2O for 2 min. (d) Sample H1084 - Pre-anneal at 605°C under N_2O for 20 min. 15 min growth at 605°C with a fast 2.67x7.47^{-6} mol/min DMZn flow rate. Post-anneal at 905°C under N_2O for 2 min. The circled features are related to the locations of holes of exposed sapphire. (e) Sample H1086 - Pre-anneal at 905°C under N_2O for 20 min. Growth at 705°C with a reduced 7.47^{-6} mol/min DMZn flow rate. The average growth rate was further reduced by growing for 30 s with 30 s of no growth for 60 cycles. Post-anneal at 905°C under N_2O for 2 min. The arrow indicates the bottom right corner of a large rectangular marker.